Fall 12-1-2018

Structure-Property Relationships of Solvent-Cast Organic Thin Films For Model Corrosion Control Coatings

Austin Maples
University of Southern Mississippi

STRUCTURE-PROPERTY RELATIONSHIPS OF SOLVENT-CAST ORGANIC THIN FILMS FOR MODEL CORROSION CONTROL COATINGS

by

Austin L. Maples

A Dissertation
Submitted to the Graduate School,
the College of Arts and Sciences
and the School of Polymer Science and Engineering
at The University of Southern Mississippi
in Partial Fulfillment of the Requirements
for the Degree of Doctor of Philosophy

Approved by:

Dr. James Rawlins, Committee Chair
Dr. Robson Storey
Dr. Jeffrey Wiggins
Dr. Derek Patton
Dr. Gopinath Subramanian

Dr. James Rawlins Committee Chair	Dr. Jeffrey Wiggins Director of School	Dr. Karen S. Coats Dean of the Graduate School

December 2018

Published by the Graduate School

ABSTRACT

This dissertation aimed at answering several fundamental questions, specifically: 1) What is the effect of scribing parameters on visual corrosion assessments? 2) What role do molecular weight, residual solvent, and polymer composition have on morphological changes in organic thin films? 3) What alternatives to visual assessments could be implemented to better understand and detect corrosion before macroscopic failure? This research definitively proved that scribes can vary in type and dimensions, and yet are still comparable if the scribe dimensions before exposure are known. Furthermore, it demonstrated that solvents common to a variety of coating industries could become trapped within the polymeric film. Whether trapped through chemical interactions or physical limitations due to vitrification of the film, these solvents ultimately affect the modulus, T_g, and adhesion in a dramatic, complex, but detectable manner. In addition, when water-miscible solvents are utilized, they are ultimately exchanged with water and result in voids during water uptake and solvent exchange. In clear films, these voids are largely detectable without the use of aided optics as the films whiten as a result of refractive index differences between the voids and the polymeric material. However, these same results were observed in commercial pigmented thermoplastic coatings through the use of electron microscopy. The impact of these voids formed through solvent selection has yet been in the corrosion literature, and this research affords a foundation from which new formulations can be created. Lastly, the use of fluorescein was validated quantitatively for the detection of cathodic delamination, correlated with scanning Kelvin probe. These cathodically delaminated areas were quantified through a shift to basic pH at the coating-metal interface. Additionally, a ratiometric technique

using fluorescein and rhodamine B was established to determine the apparent pH at the substrate-coating interface without the need for additional experiments. The development of correlative techniques and manipulation of morphological features resulting from solvent cast polymeric thin film formulation and application conditions provided predictive results from which a specific threshold can be selectively shifted to facilitate inhibitor release rates, lower testing durations, and achieve higher throughput life-cycle assessments of coatings.

ACKNOWLEDGMENTS

I would like to thank my advisor, Dr. James Rawlins, as well as my other committee members who have been instrumental in this research: Dr. Derek Patton, Dr. Jeffrey Wiggins, Dr. Robson Storey, and Dr. Gopinath Subramanian.

I would also like to thank my funding source, The United States Air Force (FA7000-13-2-0022 and FA7000-14-2-0011), through funding by the Department of Defense and collaborative efforts for Corrosion Prevention and Understanding via the Technical Corrosion Collaboration working group comprised of The University of Virginia, The University of Hawaii, The Ohio State University, the Air Force Academy, The University of Akron, The University of Southern Mississippi, the Air Force Institute of Technology, the Naval Postgraduate School, and the US Naval Academy.

I am grateful for the collaboration and hospitality from Swansea University, specifically Dr. James Sullivan and Dr. Natalie Wint as part of a research exchange during the summer of 2018.

DEDICATION

I would like to thank my family for their enduring support while I pursued my education. They have always pushed me to do the best I could, and without them, I would not have made it this far. Each of you has taught me valuable life lessons that I will not soon forget.

I also would like to give a big thank you to my classmates of 2013-2014, especially Dr. Frazee and Dr. Cooke. Without all of you, this work would not have been possible. I appreciate all of the guidance and help you all gave me.

From my research laboratory, I would like to thank Dr. Williams for working through the complex findings and getting as excited as I did on finding explanations for our results. You really made it enjoyable to work through difficult problems. To the rest of my research group, thank you for all of your help, whether it was instrumentation, data collection, or being a sounding board. I appreciate all of you.

A big thank you to the SPECIFIC team at Swansea University. You all put your research on hold to help me and were all excellent to work with. I cannot express enough gratitude for everything you all did for me to make it feel like home and collect meaningful data while still having fun.

TABLE OF CONTENTS

LIST OF TABLES

LIST OF ILLUSTRATIONS

LIST OF ABBREVIATIONS

AFM	Atomic force microscopy
ASTM	American Society for Testing and Materials
ATR-FTIR	Attenuated total reflectance – Fourier transform infrared
CPVC	Critical pigment volume concentration
CyNONE	Cyclohexanone
DSC	Differential scanning calorimetry
EEP	Ethyl-3-ethoxypropionate
EIS	Electrochemical impedance spectroscopy
FSCN	Fluorescein
HPTSA	8-hydroxypyrene-1,3,6-trisulfonic acid trisodium salt
IMPACT	International Measures of Prevention, Application, and Economics of Corrosion Technologies
ISO	International Organization for Standardization
MEK	Methyl ethyl ketone or 2-butanone
MIL-SPEC	Military specification
NACE	National Association of Corrosion Engineers
PC	Propylene carbonate
PGME	1-methoxy-2-propanol
PVB	Poly(vinyl butyral-co-vinyl alcohol-co-vinyl acetate)
PVC	Pigment volume concentration
RH	Relative humidity
RhB	Rhodamine B

RH-DMA	Relative humidity dynamic mechanical analysis
RS	Residual solvent
SEM	Scanning electron microscopy
SHE	Standard hydrogen electrode
SKP	Scanning Kelvin probe
T_g	Glass transition temperature
TGA	Thermogravimetric analysis
THF	Tetrahydrofuran

CHAPTER I – INTRODUCTION

1.1 Polymeric-based corrosion control

Traditionally, polymeric coatings are the most abundant means of controlling corrosion, both with and without corrosion inhibitors.[1] These organic films provide a physical and chemical barrier to the substrate, and they are typically effective until water, oxygen, and electrolyte(s) penetrate the film. These contaminants (water, oxygen, electrolyte(s)) can enter the coating through a defect, mechanical damage, or diffusion through the coating over time, resulting in potentially catastrophic coating failure and consequently, metallic substrate failure.

Corrosion is a direct result of environmental impacts changing a metallic material, whether it be a pipeline, boat, or building, from the unstable state to its more natural oxide state.[2] To protect these assets, reduce maintenance costs, and offer services safely, metallic substrates are coated with organic films composed of binders, solvents, fillers, and other additives. Organic coatings are often designed to afford a barrier to environmental conditions an asset may encounter, but typically lack the long-term performance needed for low cost and maintenance options. Furthermore, there is a fundamental lack of understanding of the complex interplay of all of the components within a final formulation and how they impact a coating's final performance properties.

A 2016 NACE (National Association of Corrosion Engineers) IMPACT (International Measures of Prevention, Application, and Economics of Corrosion Technologies) study found that over USD $2.5 trillion is spent each year globally on corrosion-related failure.[3] They also estimated that with current technologies, if best practices were instituted, costs savings could range from 15 – 35%.[3] While these costs

savings are identified using current technologies, with advancements in coatings, either through binder chemistries or better understanding of inhibitors, more significant cost savings could be realized. Figure 1.1 details the average percentage of corrosion-based expenditures in five major countries with very different economic market sectors. In all of these cases, services such as water and power, and industry (oil and gas) dominated expenditures to combat corrosion and maintain assets, indicating a need for better understanding of organic coatings for corrosion control. Furthermore, this graphic highlights the need for the study of corrosion as it not exclusively a single market issue, rather it pervades all of the industries where metal infrastructure is present.

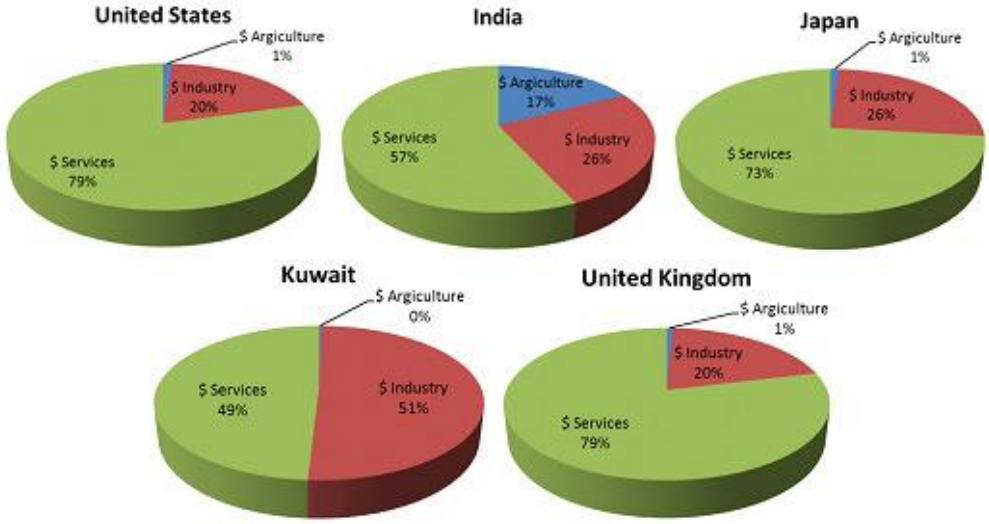

Figure 1.1 Corrosion cost by market sector.[3]

Total estimated corrosion cost is $2.5 trillion annually. These graphs indicate distinct market sectors from different nations and where the corrosion cost is most prevalent.

Organic coatings have long been used to protect an underlying substrate because they are easy to apply, offer a wide variety of chemistries, and are cost-effective.[4] Over the years, incremental gains in coating efficacy at corrosion prevention have occurred. Most often, slight adjustments are made to coating formulations to improve the protection

of the film for metal substrates; however, these changes are often based on experience with little consideration or knowledge of tunable parameters for predictable performance.

Typically, coatings are applied in several different layers, each with specific attributes that contribute to the overall protection of the substrate. Primer coats are primarily used as corrosion inhibitor carrying matrices and to promote adhesion with a colored top coat.[5] Depending on the coating system, there may be an intermediate coat that contains the pigments or other performance additives, followed by a top coat that contains UV inhibitors and affords better resistance to water and/or oxygen permeation.[5-6] In coating systems that only have two layers, the top coat contains both the UV inhibitors and pigments and provide the final aesthetic and/or protective finish. Most commonly, epoxy based chemistries are utilized as primers, whereas acrylics and polyurethanes, or hybrids thereof are topcoats.[7-8]

Figure 1.2 lists an abbreviated timeline of events, starting with coating application to coating failure. Initially, upon application of a coating, solvent loss and crosslinking of the polymeric binder causes a shrinkage, increasing the internal stress of the film. Upon exposure to the environment, photo-oxidation or UV degradation occurs, along with water and electrolyte transport through the film. These initial exposures can cause nano or microscopic cracks and voids to form and cause color changes in the protective film. Upon sufficient exposure, cathodic and anodic regions form, either through defects in the film or damage obtained through use. The development of cathodic and anodic regions causes delamination and film porosity increases. After enough damage or corrosion progression has occurred, catastrophic film failure results in loss of the protective coating and, with a lack of attention, asset failure.

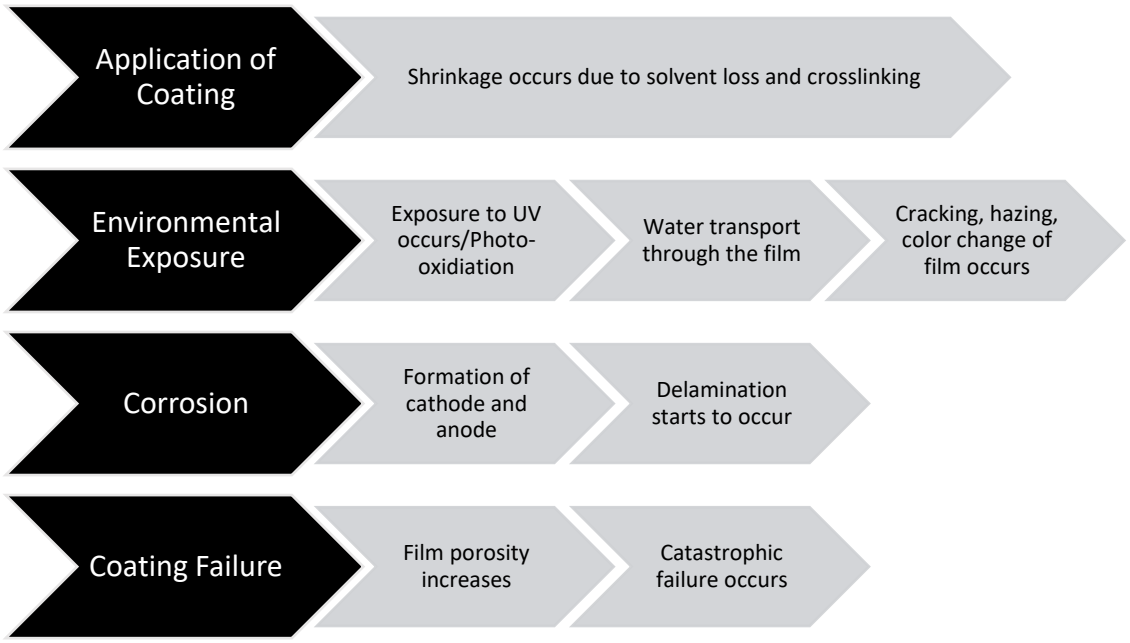

Figure 1.2 Abbreviated timeline of important events from coating application to coating failure.[9]

Between coating application and corrosion e.g., what changes in film properties (microscopic, mesoscopic, macroscopic) occur prior to visual macroscopic corrosion remain largely unknown. Martin et. al. described this temporal region of unknowns as an "induction period" during which some performance characteristic or changes in characteristics of a coating are unobservable.[10] Only after some critical threshold of changes and processes occur, can the coating performance be directly interrogated whether the measurements are adhesion, diffusion, visible corrosion, or some other polymer property difference, e.g., blisters. Due to the complicated nature of commercially available coatings (often >10 raw materials combinations thereof), researchers have shifted to the use of model polymers that contain either no or little additives and pigments. The simplified models reported herein are most often coatings

comprised of solely thermoplastic polymers for the ease of processing, availability of advanced characterization methods that require post-application and post-environmental exposure solubilization of the polymer, the ability to change solvent conditions without catalyzing or inhibiting the cross-linking reaction, and to avoid chemical or physical vitrification, which has been reported as a complex and complicated process for every solvent-cast thermoset.[5, 11-16] By simplifying, i.e., knowing each component included in the thermoplastic coating, a better understanding of the complex interplay between each of the components during the induction period was envisioned to be attainable. Furthermore, this knowledge can facilitate faster development of new materials to be screened in later testing, and new test methods and protocols to determine limiting quantifiable variables towards improved understanding and ultimately less corrosion related failures.

Upon critical review of the timeline in Figure 1.2, several questions arise: 1) When has the coating failed and how did it fail? 2) When can corrosion be stopped to prevent catastrophic failure? 3) Are these changes quantifiable, and if so, how? Many researchers use qualitative methods to determine the effect of new additives or binders; however, these are inherently subjective. This dissertation aimed at addressing the earliest quantifiable key performance factors that either shift the induction time to earlier detection times such that the performance characteristics are observable before macroscopic corrosion occurs, or, in the case of Chapter V, utilize more sensitive techniques. With respect to Chapter V, there still exists an induction time, but the developed characterization method detects and quantifies material changes on an earlier time scale and may afford a direct measurement of dissolved ionic species *in-situ*. For

example, visual corrosion detection is the only major method utilized worldwide for monitoring corrosion rates. This visual analysis is out of necessity and yet reduces every research activity to a limit of waiting until visible rust is detected to determine any differences in corrosion rates. These data are widely reported and render research stagnate in determining mechanistic differences for actual corrosion resistance. The minimal sufficient time to see corrosion for polymer-based coatings can range from days to years and rarely results in quantities for performance above relative rankings of systems due to the complexity and single nature of analysis. By using fluorescent probes, a waiting period still exists for visual detection, but the fluorescent detection time is truncated often by an order of magnitude, e.g. minutes or hours for fluorescence turn on to occur compared with days or weeks for visible corrosion spots in the same system and conditions. Figure 1.3 illustrates the induction period as reported by Martin and coworkers with respect to time and critical failure.[10]

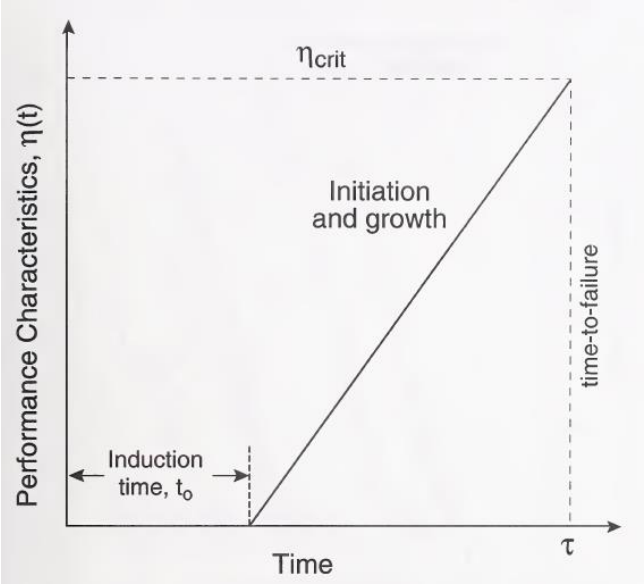

Figure 1.3 Representation of performance characteristics of a coating over time.[10]

Performance characteristics can include blistering, color change, visual corrosion, blushing/whitening, loss of adhesion etc.

In the case of this research, Chapter III was a prime example of waiting for some induction period before any measurements could be accurately performed on coated substrates. However, Chapter IV addressed and observed possible performance characteristics and placed in context how the "induction time" related processes may be shifted or altered when a defect free coating is exposed. In this example, some critical characteristic or ratios of characteristics (residual solvent type and concentration, polymer molecular weight relative to residual solvent, dry versus environmental T_g, adhesion, and use temperature) impart an irreversible change on the polymer film such that upon exposure to water, the film is drastically altered and the visual performance was directly correlated to the void formation. Importantly, the measured induction period, or time before a performance characteristic change is observed, is characteristic dependent. Again in the case of the whitened films, the performance characteristic may be corrosion, in which case the void formation occurs during the induction period. If the performance characteristic of a color change, is desired, then the induction period would be water sorption into the polymer film prior to whitening. In all cases of this research, water sorption into the film occurs during the induction period, regardless of the critical or desired performance characteristic. Each chapter of this dissertation focused on answering at least one unknown processes or mechanistic changes that occurred in advance of macroscopic corrosion. In Chapter III, the tool type and resultant scribe width impacted the induction time such that wider scribes underwent larger macroscopic changes earlier in accelerated corrosion testing. Chapter III also determined vital variables often overlooked during accelerated corrosion measurements that result in substantial performance differences in coatings and attempts to remove the human error

in testing. Chapter IV measured key polymer performance attributes that impacted the induction period before visual corrosion would occur on defect-free films. Morphological changes driven through solvent selection, retention, and exposure to environmental contaminants often found during an asset's lifetime were characterized along with methods to increase the induction period to extend a coating's lifetime. Lastly, Chapter V quantified a more sensitive method to detect corrosion earlier without changing the induction time for visual corrosion using SKP compared with fluorescence turn on based upon fluorescein being sensitive to basic pH environments (pH $\geq$7). It was hypothesized that overall, this research would result in fundamental gains in understanding of how polymer film morphologies are altered using common solvents and drying and annealing conditions for film formation and as well as elucidate variables in early detection for accelerated corrosion testing that are critical to the measured coating performance in the presence of a defect. Thus, each chapter focuses on different performance characteristics in advance of macroscopic visual corrosion and provides quantities which have not been correlated with precursor events to corrosion being detected visually.

1.2 Morphological features of polymer thin films

Typically, polymeric binders are thought of as homogeneous materials, unless intentional phase separation/stratification or fillers such as pigments or fibers were employed to influence the coating.[17-21] When considering pigmented coatings, it has been shown that below a critical pigment volume concentration (CPVC), there exists sufficient polymer binder to completely encompass the pigment or inhibitor particles.[22-23] Formulating below the CPVC ensures that no macroscopic air voids remain between the

pigment, filler, or inhibitors and the polymeric binder; however, above the CPVC, the film becomes discontinuous, creating detectable and large voids.[6, 22-25] The voids increase in number and size the further the coating is formulated above CPVC, decreasing the barrier properties of the coating. Utilizing unpigmented coatings for fundamental research overcomes this issue of CPVC. In the case of unpigmented coating chemistries, epoxy-amines are the most highly studied thermoset organic coatings. The study of fracture planes by various researchers has demonstrated that within epoxy-amine films, nodules of approximately 50 nm in diameter are formed during the curing and vitrification process.[13, 26-28] However, within the morphological research of coatings, comparatively little work has been performed on other systems, specifically solvent-borne thermoplastics.

Considering that, by design, only minor particulates (dust, oligomers, surfactants, etc.) are present in transparent films, un-pigmented systems are expected to consist of only resin and solvent and perform as such. Films free from impurities should be uniformly homogeneous, with smooth fracture planes depending on the T_g of the polymer. In one of the earliest studies, Fedors found that when a water-soluble salt was present within a rubber elastomer, voids formed as the salt was dissolved.[29] Water sorption into the rubbers concentrated where water soluble impurities were located; however, when the salt was insoluble, the rubber exhibited no voids or cracks.[29] The spatial specificity of void and crack formation suggested that the extent of void size and number of voids was dependent on the spatial location and solubility of the salt present. Based on this research, a correlation was also drawn between the voids and the modulus of the polymer matrix within which the salt was contained. In more recent literature,

Sundberg *et al.* observed a similar phenomenon in both solvent and water based acrylic systems. Films cast from solutions that contained residual surfactants from the polymerization process exhibited more voids and greater void volume during water immersion.[30] As these voids grew, they absorbed a broader range of visible light, and the films became more opaque. These voids were shown to contain heterogeneous water clusters and resulted in light scattering due to refractive index differences between the water, polymer, and air.[30] When given a sufficient amount of time under immersion conditions, these voids achieved a sufficient domain size that the film became opaque to the unaided eye.

Comparatively little work regarding this void content has been performed on non-pigmented coatings outside of acrylic-based chemistries that inherently possess distinct phases (water or solvent and polymer particles) in advance of film formation.[31-32] Other examples of polymers that whitened with the introduction of water include molten polyethylene saturated with water during processing, and polycarbonate when exposed to water above its glass transition temperature (T_g).[33-34] These data correlate to the process suggested by Fedors in which the internal osmotic pressure must overcome the external pressure, or modulus of the polymeric matrix in which the void is formed (Equation 1).[29] Sundberg *et al.* offered a clarification of the polymeric modulus, such that it should be represented by the water or solvent-plasticized bulk polymer modulus (Equation 2).[30]

$$P_{int} = \frac{G}{2}\left[5 - \frac{4}{\lambda} - \frac{1}{\lambda^4}\right] \qquad \text{Equation 1.}$$

Where P_{int} is the internal pressure of a water-filled void, G is the storage modulus of the polymer, and λ is the ratio (r/r_0) of radius at a current point compared to the initial void or solute size

$$P_{ext} = f\ (plasticized\ polymer\ modulus) \qquad \text{Equation 2}$$

Where P_{ext} is some function of the plasticized polymer modulus.

By combining these theories, inhibition of voids should occur when $P_{int} \leq P_{ext}$. Upon sufficient void growth, the film or rubber appeared opaque. The internal pressure that can be caused by water has been relatively neglected by materials scientists; however, it is of great importance in the botany and biological field.[32, 35-43] The amount of pressure water can exert on a cell has been highly researched concerning trees and other plant life because, without this pressure, tall trees could not exist due to the lack of water in the upper part of the plant.[40, 44] The water cohesion-tension theory acknowledges that water has a tensile strength due to its high polarity and hydrogen bonding capabilities.[45] Experimentally, most researchers have only been able to measure 10's to 100's of MPa, which is far short of the theoretically calculated limit of ~1,500 MPa.[40-41, 44, 46-47] However, this research posits the water cohesion-tension theory to provide a critical value for DMA experiments within Chapter IV of this dissertation. While the water cohesion-tension theory is a widely disputed topic within the botany world, the theoretical basis may explain the water sorption, void formation, and growth observed in polymeric films.[46] Combining the values obtained theoretically in the water cohesion-tension theory with the knowledge that water-miscible domains must exist to form voids leads to a greater understanding of the effect of residual solvents and impurities within cast films. Critically, the internal macroscopic structure within polymeric films contributes largely to mechanical and thermal performance. By correlating these starting polymer structures and solvent combinations with the resultant behaviors before, during, and after exposure, a more complete picture of changed

polymer film morphology can be realized. This knowledge would allow for a greater understanding of inhibitor transport through a film or the protective capabilities of an inhibitor in a coating that does not contain a defect. As Fedors and Sundberg both acknowledged, a water-soluble or miscible component must be present within the film for the formation of these voids. In the case of the thermoplastic films used herein, the composition of the spray solvent is such that each component is readily miscible in water, which gives rise to water clustering and aggregation sites for void formation.

Solvent-induced morphology is used to describe the resultant bulk features of a polymeric system that has been directly influenced by the type and concentration of solvent used in casting a film, or by preferential evaporation techniques.[12, 48-51] Solvent characteristics such as polarity, boiling point, and solvency power influence the film morphology, either accidentally or intentionally to drive aggregation events or alter transport properties of water and other electrolytes.[12, 48-54] Currently the most studied solvent-induced morphology variability relates to trends in organic photovoltaics or block copolymer assembly and aggregation. Muller-Buschbaum *et al.* measured the influence of four independent solvents on the morphology of poly(3-hexylthiophene)-phenyl-C61-butyric acid methyl ester (P3HT-PCBM) photovoltaics.[50] Various crystal sizes were achieved by merely using solvents with varying boiling points to cast the films. Matsumoto and co-workers modified the morphology of poly(3,4-ethylenedioxythiophene) polystyrene sulfonate (PEDOT-PSS) films utilizing both vapor and liquid state solvents, which significantly altered the morphology and the conductivity of the resultant films.[48] Furthermore, the chemical composition of the solvents induced differing layering capabilities of the P3HT-PCBM films, ranging from entirely

heterogeneous material separation to a gradient of polymer compositions. With regards to copolymer morphologies, Jung and Ross were able to change the pattern width as well as shifting the pattern from lines to perforated lamellar structures by simply changing the composition of the solvent vapor in their research.[51] While these take the forefront of morphology alteration resulting from differential solvent conditions, surface coatings could also be influenced by judicious solvent selection. In coatings, morphology is often discussed and yet poorly observed, and rarely are data accompanied by quantifiable variables. By altering the morphology predictively and controllably, organic coatings could be tailored to provide a specific inhibitor release profile or act as a membrane for selective electrolyte transfer. To measure these morphologies, scanning electron microscopy (SEM), atomic force microscopy (AFM), and transmission electron microscopy (TEM) are often used to visualize the conformation after preferential solvent evaporation or vapor annealing.

While SEM, AFM, and TEM are the most common techniques for measuring morphological changes, internal stress measurements can also be performed to afford a quantitative measure of the stresses that are induced throughout a coating's lifetime. Internal stress measurements detect and directly interrogate the amount of induced stress that occurs between films and substrates, whether from solvent loss, crosslinking, vitrification, swelling, or other environmental events surrounding polymer film formation and exposure.[55-57] The single cantilever beam method is the most applicable to a single-sided coated material, such as a decorative or protective coating. In this case, the amount of bending a thin metal substrate undergoes during wet and dry exposures provides greater insight regarding the amount of stress that is present within the conditionally

specific applied film. Croll successfully measured the internal stress developed in a solvent-based poly(isobutyl methacrylate) coating by utilizing a single cantilever beam deflection method (detailed in Chapter II).[58-59] He suggested that internal stress develops in a solvent-cast coating during solvent evaporation and the "locking in" of polymer conformations on a localized level, or in simpler terms: the more residual solvent, the lower internal stress a coating exhibits due to the solvent allowing for more degrees of freedom. Sato expressed the total internal stress of a coating as a sum of three primary factors: 1) solvent loss during drying/curing; 2) thermal stresses resulting from a differential in the coefficient of thermal expansion; and 3) polymer degradation stresses.[60] Solvent cast thermoplastics, like the ones used in this research, primarily exhibit internal stress related to solvent loss at early times, and through solvent extraction during immersion measurements.[61] Single layer, single polymer coatings would exhibit minimal stress from thermal expansion as there exists only one primary component. At later times of exposure, polymeric degradation stresses, such as loss of adhesion would affect the stress within the film. Negele's and Funke's data support this hypothesis as each distinct region within a measured internal stress curve relates to either: 1) water ingress into the film, or 2) adhesion-related bond rearrangement at the cantilever-coating interface. During the experiment, the coated cantilevers are exposed to liquid water, which is a less effective plasticizer than the solvent used to cast the coating.[61-66] The solvent is miscible in the water, leading to water-derived solvent extraction and stress differentials. This water extraction of the solvent leaves voids that upon future exposure of water allows for water aggregation. Critically, the solvent of the cast films behaves similarly to the salt

and surfactant experiments performed by Fedors and Sundberg leading to a new understanding of solvent selection in polymeric thin films used in a protective capacity.

Combining the concepts of solvent-induced morphology with respect to non-solvent interactions between the water and polymer, void formation caused by solvent extraction of water miscible components within the film, the water cohesion and tension theory found in nature, and the ability to measure internal stress during morphological changes, the variations in organic protective coating morphology can be systematically controlled. The relationship between residual solvent and molecular weight were defined and captured, and are believed to be occurring in all thermoplastic coatings, thus altering their short and long-term performance throughout the life cycle of the coated material. Chapter IV addresses the lack of research in solvent – non-solvent interactions that occur in a solvent-cast films during exposure conditions. A systematic study on the T_g and modulus of the coating was found to directly relate to the ability to form microcellular domains through commonly found residual solvents from the application, building on current literature precedents. Selectively altering the amount of residual solvent and molecular weight of solvent-cast films resulted in the understanding of critical performance parameters related to attaining, retaining, and losing corrosion control properties. It is expected that the tailorability of the coating morphology could be exploited to alter inhibitor transport rates, as well as a tool to help understand failure mechanisms of coatings that failed in the absence of an intentionally induced defect.

1.3 Coating and corrosion testing protocols and methods

Throughout literature, typical anti-corrosion coating performance evaluations are performed using intentional defects in a metallic substrate-bound film exposed to an

accelerated weathering evaluation under conditions of a corrosive environment.[67] This method allows for quick assessments of new coating technologies, i.e., new formulations, corrosion inhibitors, polymeric binders, etc., rather than waiting for longer times for real-world testing. These visual cues are considered commonplace owing to their apparent simplicity, and in many cases, required by certain specifications, such as MIL-SPEC or several ASTMs and ISOs.[68-71] Various electrochemical evaluations are used for advancing the analysis of corrosion failure with polymer coatings; however, these techniques are often costly and have limited use on fully formulated coating systems. Thus visual assessments of accelerated weathering are standard practice for the performance evaluation of a material system, especially in commercial industries. While it is accepted that accelerated weathering yields information about the coating's corrosion resistance and performance in corrosive environments, little discussion exists regarding the dimensions of the initial defect in the polymer coating. These initial defect characteristics, such as scribe width, roughness, and/or depth of a scribe are typically not mentioned in literature and result in a lack of correlation between laboratories, or even repeatability within individual laboratories with regards to visually assessing corrosion performance. Furthermore, there is a significant lack of discussion regarding the corrosion performance results with the selected scribe tool and establishing the dependency the scribe choice had on the reported results.[72-76] Tool types are rarely reported, and when it is, there exists a considerable variation in the scribe parameters which unnecessarily compounds the complexity of the results.[77-84] ASTM D1654 provides recommendations between two different tools, a carbide pen or a lathe tool (ANSI B94.50 Type E), but does not state a specific tool geometry or size that is required

for use.[69] Much of the current literature fail to include tool geometry, spindle rotation, and material feed rate in their published methods, making accurate reproduction of experiments difficult or impossible. Of the reviewed literature, only one publication attempted to delineate scribe profiles and their relation to corrosion assessments. Yasuda et al. studied the width and profile (U-shaped vs. V-shaped) on aluminum 2024 (AA-2024) substrates utilizing electrochemical impedance spectroscopy (EIS) measurements.[85] They found that the impedance of the coating did not change based on scribe width or depth; however, it was reported that a drag tip (V-shaped) resulted in higher impedances than those created with a rotating spindle (U-shaped).[85]

The standard procedure for visual assessment of corrosion performance of a coated sample is to use an intentional defect through the protective film on coated metal substrates. Merely making a defect in the coating is not sufficient for understanding and reporting an evaluation of anti-corrosion coating performance. With the drive to eliminate high-performance corrosion-prevention pigments, like $SrCrO_4$, from commercial applications due to toxicity concerns, a more accurate method for reporting the actual performance of a coating system is necessary for inter-laboratory comparison of the performance of new technologies in a correlative and quantitative manner.

To expedite corrosion testing procedures, several accelerated techniques have been developed. Although these tests do not offer a direct comparison to real-world exposures, they allow for faster rates to down-select material combinations for outdoor exposure. ASTM B117 consists of a constant 5% NaCl spray at 35 °C and is meant to simulate an aggressive marine environment.[67] More recently, General Motors (GM) developed a technique that is more representative of the conditions a coating will face in

the real world. This system consists of three distinct eight hours steps per 24 hour cycle: 1) a three minute salt spray (0.9 wt% NaCl, 0.1 wt% $CaCl_2$, and 0.0075 wt% $NaHCO_3$) at the beginning of an eight hour hold at 25 °C and 45 %RH; 2) a one hour ramp to 49 °C and 100 %RH, held for seven hours; 3) a three hour ramp to a dry stage at 60 °C and 25 %RH, held for five hours.[86] In doing this, samples are exposed to elevated temperatures, which are often at or above the coating's T_g, various salts typically found in the environment, and changing humidity, representative of dew cycles. Both of these cabinets were utilized in this research to afford a comparison of results obtained. Chapter III compared the results obtained from each chamber and afforded a direct relationship when measuring cathodic delamination and the appearance of visual rust from a defect. Therefore, the majority of corrosion measurements within this research utilized 5% NaCl solutions to afford comparable data to those obtained during ASTM B117.

1.4 Corrosion and corrosion inhibition

1.4.1 Corrosion Process

Much of the metal used for structural or decorative purposes does not occur in nature in that state. During production, metallic ores are stripped of impurities and alloyed with other elements to achieve the desired properties.[87] The product of this energy-intensive process is temporarily stable, but over time, the material reverts to its natural, thermodynamically stable state, which manifests as corrosion.[5, 88-90] The corrosion process (Figure 1.4) is a simple electrochemical cell in which the corroding metal acts as an electron donor (anode) as the metal oxidizes. Free electrons from the metal react with other species (primarily water or oxygen) at the cathode (or electron acceptor). Upon

oxidation, the metal undergoes dissolution and eventually forms insoluble iron oxides and hydroxides that are deposited.

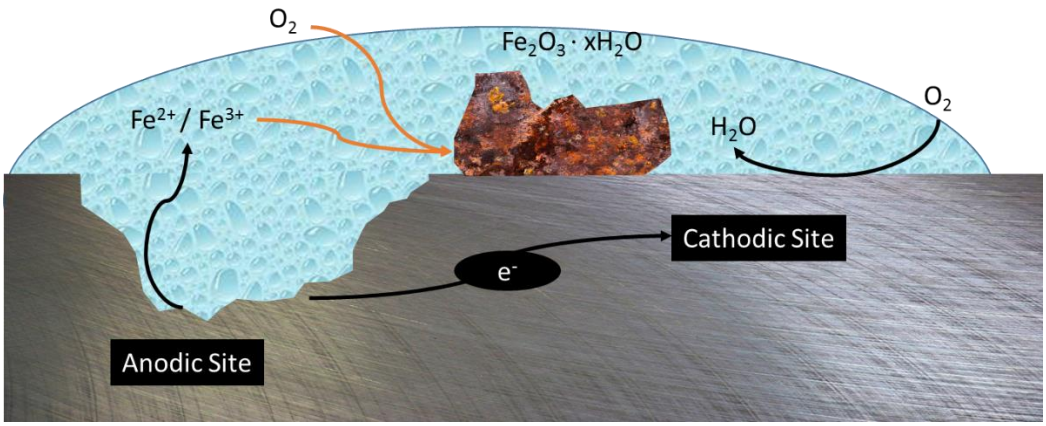

Figure 1.4 Corrosion process for steel substrates in the presence of an aqueous electrolyte.

Electrolyte accumulation at the metallic interface initiates corrosion, resulting in metal dissolution at the substrate. Once the metal dissolves, voids and cavities form, further exposing new metal to the electrolyte. As more electrolyte infiltrates the coating to the coating-substrate interface, delamination and blister formation occurs as a result of differentials in internal stresses. Precipitation of the dissolved metal(s), oxides, hydroxides, and salts results in higher stresses at the coating-substrate interface. Water penetration to the metal interface also weakens mechanical adhesion from plasticization and swelling of the polymer and eventual bond hydrolysis.[91] When the mechanical adhesion is weakened and the internal stress is increased, severely diminished protective capabilities of the organic coating are observed.[55, 61, 65, 92-98]

These corrosion reactions cause potential and pH gradients to form at the metal substrate. At the dissolving metal (anode) a more negative potential is observed, characteristic of freely corroding metal. At the cathode, a more positive potential occurs

due to the reduction of water and oxygen. The redox reactions also cause a change in the pH where the anodic region is more acidic due to the excess H^+ formed, while the cathodic site is more basic due to the formation of OH^- species. The two primary half cell reactions exploited in this work are listed in Figure 1.5. The pH formed at the substrate during these reactions has been reported as between 10 and 14 at the cathode, and between 3 and 4 at the anode.[99-102]

$$M \rightarrow M^{n+} + ne^- \text{ (metal dissolution)}$$

$$O_2 + 2H_2O + 4e^- \rightarrow 4OH^- \text{ (oxygen reduction in neutral/basic solutions)}$$

Figure 1.5 Select corrosion half-cell reactions.

Because of these potential and pH gradients, corrosion occurring beneath the coating can be detected and monitored; however, the throughput and usefulness of commonly used techniques such as electrochemical impedance spectroscopy (EIS), are limited. While these type of electrical techniques attempt to provide quantifiable corrosion results, there is little correlation between laboratory measurements and actual environmental corrosion performance. The nature of EIS which will be covered later in this chapter limits the applicability to adequately measure corrosion in a spatially defined manner, leading to poor performance predictions. The use and validation of fluorescent probes to spatially define corrosion events before macroscopic corrosion is highlighted in Chapter V as a viable technique to track corrosion and measure the effect of inhibitors and electrolyte exposure. It was hypothesized that the pH at the interfacial region between the polymer and metal substrate would be sufficiently basic during cathodic delamination that fluorescein would respond quantifiably and in a spatially defined manner such that fluorescence could be realized as a viable alternative to electrochemical

methods. Furthermore, it was expected that quantifiable correlations between fluorescent intensity and scanning Kelvin probe would be possible if the two methods were tracking the initial metal dissolution and development of a distinctly cathodic region.

1.4.2 Corrosion inhibitors

In addition to organic coatings providing a physical barrier to contaminants, several types of corrosion inhibition are employed. Industrially relevant, but non-polymeric in nature is the used of sacrificial anodes, in which a more corrosive metal (Table 1.1) is electrically connected to the substrate being protected, forming a galvanic couple. Most often, zinc is used due to its high corrosivity. The sacrificial anode corrodes before the protected material and requires replacement upon depletion. Cathodic protection is also used industrially and consists of a positive charge flowing to the substrate to prevent the anodic reaction from occurring. The concept of sacrificial protection has also been extended to the use of zinc, magnesium, and aluminum particles and flakes to create a metal-rich primer in which the metal pigments corrode and form a protective oxide layer prior to substrate corrosion.[103-105]

Table 1.1 Galvanic potential table for various metals.

Most anodic (active)

Most cathodic (passive)

Metal	Corrosion Potential (mV)
Magnesium	<-1600
Zinc	-1000
Aluminum	-700 - -1000
Steel	-400 - -700
Copper	-300 - -400
Gold	200-0
Graphite	>200

Metals and their corresponding potentials. Adapted from StructX engineering resources.[106]

Aside from metal-rich primers, corrosion inhibitors are often included as either a pretreatment or in the primer itself. Based on their mechanism, corrosion inhibitors are

divided into three main classes: anodic inhibition, cathodic inhibition, and mixed inhibition. Anodic inhibitors interfere with the oxidation of metal at the anodic site and typically contain functional groups such as nitrites, ferricyanides, phosphates, and silicates, while cathodic inhibitors interfere with the reduction of oxygen at the cathodic site.[107] Zinc, in the aforementioned zinc-rich primer, is a popular cathodic inhibitor due to the deposition of insoluble $Zn(OH)_2$ at the cathodic site, blocking further reduction reactions, and can also be found as a pretreatment on many steels as a galvanizing layer.[107] Strontium chromate is considered the standard for corrosion control performance and is a mixed inhibitor where the chromate ion acts as an oxidation interferer while the strontium ion preferentially is reduced instead of the oxygen, thus stopping the cathodic reaction.[108] With the environmental and health risks of chromate inhibitors realized, there is a drive to replace all chrome-based products with less hazardous materials; however, little understanding of inhibitor transport and efficacy due to polymeric properties exists. Most corrosion inhibitors are typically included in coatings from 1-15 weight percent, yielding no consistency in the amount required to mitigate corrosion.[109-111] These high concentrations are utilized to overcome the lack of fundamental knowledge of how inhibitors are transported to corrosion sites and the effect the polymer has on these migration rates.

Chapter IV of this dissertation offers a method to control void content and subsequently, transport rates of inhibitors. The use of a model thermoplastic with tailorable void content and size can provide a simple scaffold to study inhibitor release kinetics and efficiency studies. If the inhibitor cannot migrate, it cannot protect the substrate. Conversely, if it is too soluble or transports too quickly, the coating will

deplete it protective capabilities rapidly, causing premature failure. Through proper solvent selection and drying and annealing conditions to result in differentials of residual solvent, a model thermoplastic film is proposed to address these shortcomings of current inhibitor studies.

1.5 Detection of corrosion

1.5.1 Electrochemical methods

Electrochemistry has been used to monitor polymer performance in regards to barrier properties, inhibitor efficacy, and water diffusion to predict service lifetimes.[112-113] Barrier properties of coatings in an electrolyte source have been monitored with electrochemical impedance spectroscopy (EIS), which is based on Ohm's Law shown in Equation 3, where *Z* is the complex impedance and accounts for amplitude of voltage and current signals, *V* is the voltage perturbation, *I* is the current at the given voltage, and ω accounts for the phase shifts that arise from the use of alternating current (AC).

$$Z(\omega) = \frac{V(\omega)}{I(\omega)} \qquad \text{Equation 3}$$

While EIS has been useful in determining the barrier properties of coatings, it does not adequately predict the corrosion performance of the film. Because it is such a macroscopic technique, any pinholes in the coating will lead to artificially lower impedance values. In fact, due to various heterogeneities in the coating, or any minor defect, replicates have been found to have over three orders of magnitude in impedance variation.[114] Furthermore, because equivalent circuits are made based on best-fit to experimental data, several circuits may adequately meet the parameters. Therefore, prior knowledge of what is occurring at the coating-substrate interface must be known.[114] Figure 1.6 details a typical impedance plot used to determine the corrosion resistance in

literature examples. In this plot, the impedance is plotted against the applied frequency of the AC wave. Films that exhibit higher impedance, usually $1E^9$ Ohms or greater, are considered good corrosion control coatings, while those lower than $1E^5$ Ohms are poor coatings.

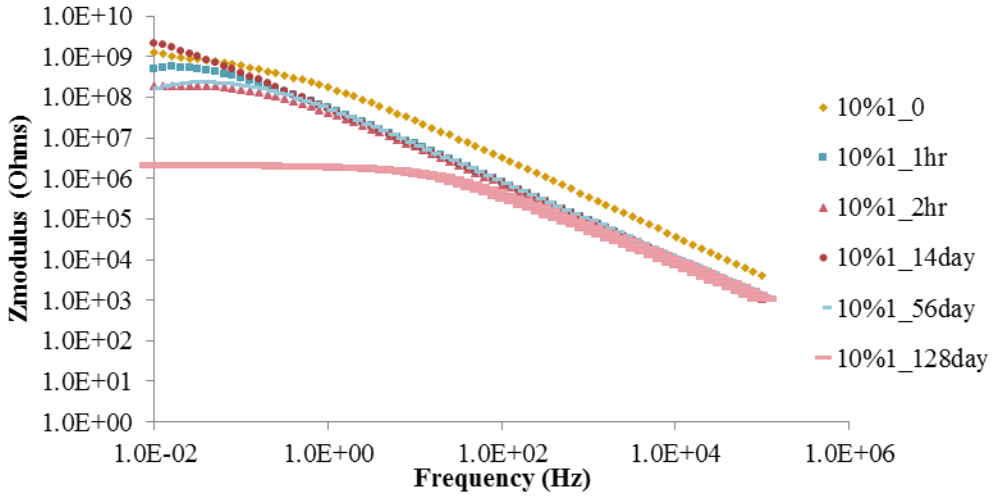

Figure 1.6 Bode plot of an epoxy-amine containing 10% PVC of Al flake.[115]

The impedance will vary depending on the frequency of the AC perturbation and the coating's electrolyte barrier properties. If the coating suffers a defect, a decrease in impedance will be observed as an electrical bridge forms between the solution and the metal panel, creating a short circuit. A straight line, increasing from right to left, is exhibited by an intact coating performing as a perfect capacitor, while plateauing of the line in the low-frequency regimes indicates the formation of a resistive element due to electrolyte ingress to the substrate. To afford a more in-depth look at the mechanisms that could be occurring at the substrate Nyquist plots (Figure 1.7) are used. These plots are created by graphing the imaginary impedance against the real impedance. The imaginary component results from the out of phase component of the sine wave from the

AC potential. In the example illustrated in Figure 1.6, a perfect, intact coating is represented by a single semicircular loop. Any breach in the coating causes additional loops to appear, due to the formation of resistive or diffusion elements from the electrolyte, corrosion product, or inhibitors.

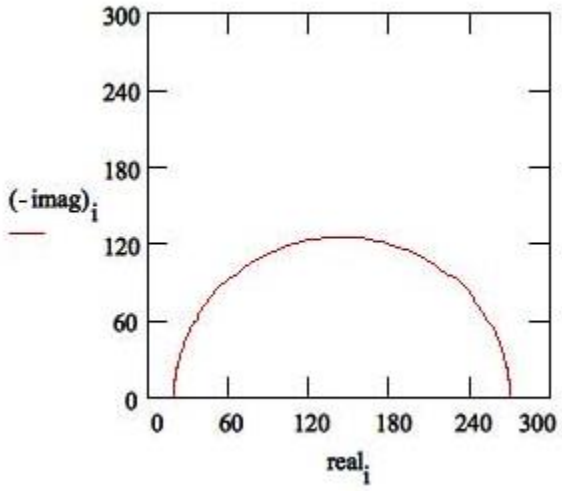

Figure 1.7 Representative Nyquist plot obtained from EIS.[116]

These plots are modeled to equivalent circuits to understand the mechanism of corrosion or the coating's response to the environment. For example, two semicircular loops indicate that water has reached the substrate; as one time constant (loop) is inherent to the coating, while the second is the metal and oxide on the substrate. Additional loops can indicate corrosion inhibitors or pigments that are oxidizing while a straight line from the circle indicates the diffusion of the electrolyte.

Corrosion inhibitor efficacy can be monitored using Tafel extrapolations (polarization curves) as depicted in Figure 1.8. If the metal substrate is protected from a corrosion event, the measured corrosion potential would shift to a lower current and a lower potential (cathodic inhibitors, Figure 1.7B), the same potential but lower current

(organic inhibitors, Figure 1.7C), or a higher potential and lower current (anodic inhibitors, Figure 1.7A).[117]

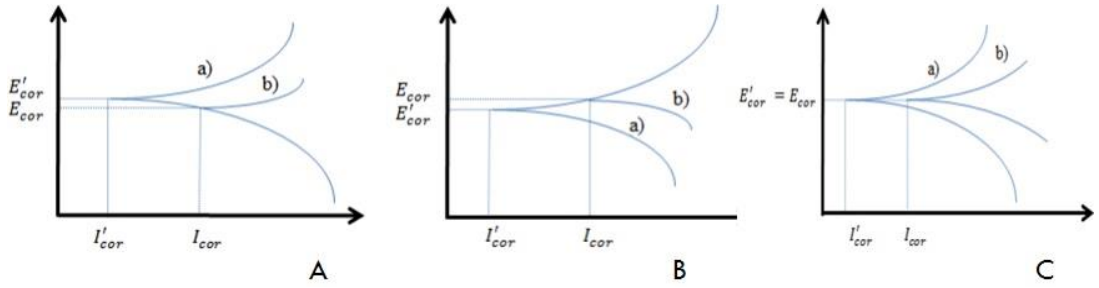

Figure 1.8 Tafel polarization curves of 3 types of inhibitors.[117]

Typical shifts in polarization potentials due to anodic (A), cathodic (B), and organic (C) inhibitors are shown, where a) is inhibited, b) is non-inhibited.

Another technique, albeit lesser known, has been used to characterize a coated metallic substrate during the corrosion process. The scanning Kelvin probe (SKP) utilizes work function differences between corroding and non-corroding surfaces at the metal interface. In this technique, a small wire is vibrated above the substrate while a potential is applied to the substrate, creating a parallel plate capacitor. Two different steps need to occur to measure the potential of the substrate: 1) an electron must transfer from the substrate to the polymer, and 2) transfer of the electron occurs from the polymer to the probe tip.[118] A bias is then applied to the tip to null the measured potential after electron transfer. Upon further changes in the potential, the bias is adjusted and the change recorded. These values are then adjusted for comparisons against a standard hydrogen electrode (SHE), resulting in potential maps from the substrate. A pictorial representation of this process is illustrated in Figure 1.9.

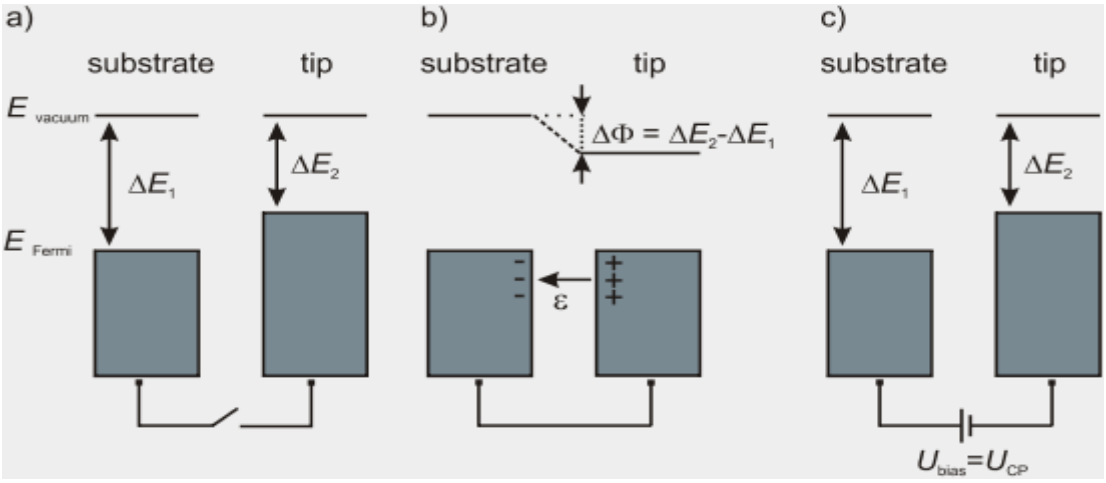

Figure 1.9 Operating principle of SKP.[119]

When performing SKP, the head is rastered across the sample such that a potential map in the X and Y plane is created. This potential map can then be used to monitor corrosion under a coating, cathodic delamination, or filiform corrosion. Potential comparisons to half-cell reaction potentials are used to determine the likely speciation of corrosion products at the substrate. Figure 1.10 displays an SKP instrument and the small gold wire used for a probe tip.

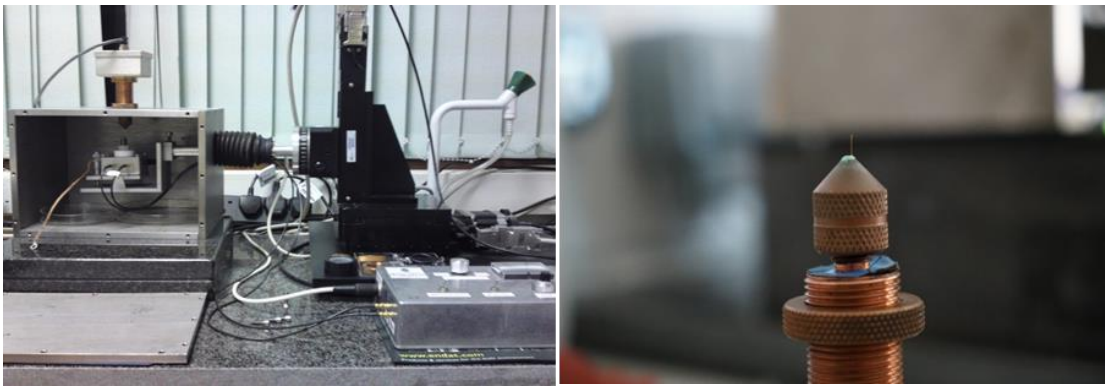

Figure 1.10 SKP instrumentation and tip (courtesy of Swansea University, Wales, UK).

Left) Typical SKP instrument equipped with a 3-axis stage and measurements are conducted inside a Faraday cage; Right) Tip of SKP (note the thin gold wire).

Stratmann and co-workers, the Leidheiser group, and the Grundmeier group have all published numerous papers detailing the use of SKP to measure ionic migration and transport during cathodic delamination, in which the concentration and salt composition were altered to measure the effect of cation and anion size on the delamination kinetics.[101, 118, 120-126] As the hydrated cation size increases, the delamination rate slows.[101] Conversely, as the concentration of the cations increases, the rate also increases.[101] During the delamination of the coating from the metal substrate, the potential of the substrate-polymer interface is represented by the combined potentials of the substrate-electrolyte and electrolyte polymer potential differences which can be directly interrogated utilizing SKP. This technique, combined with previous research regarding the use of fluorescent probes would allow for direct comparisons of the two techniques.[11] Chapter V will show that fluorescence can be directly and quantifiably correlated to electrochemical measurements, affording a faster throughput of polymeric binder and inhibitor efficacy testing for new coating and technologies development.

1.5.2 Fluorescent methods

The use of fluorescent probes for detection of corrosion in coatings is a relatively recent development.[127-138] Several methods of detecting corrosion *via* fluorescence can be employed such as chelation-enhanced fluorescence (CHEF), ionic sensing such as chloride or sodium selective fluorophores, and pH gradients.[129-133, 136-139] In chelation-enhanced fluorescence, fluorophores act as ligands for metal ions (i.e., Fe^{2+}, Al^{3+}, etc.). These small molecules or the ions must exhibit enough molecular mobility within the polymer film to afford ionic interactions. They also require a high enough concentration of both the ions and the fluorophores that the signal can be detected during

measurements. Due to the corrosion process, these metal ions are only in high concentration at the anodic region or defect site where bare metal has been exposed.

Conversely, it was previously mentioned that electrolyte cations, such as Na^+ migrate to the delamination front, which would only lend utility in the use of sodium fluorophores. However, a pH gradient forms during the corrosion process. Thus pH sensing fluorophores should provide the most significant utility as multiple probes can be used such that the entire pH range can be accounted measured.

One of the most ubiquitous fluorophores for sensing pH is fluorescein (FSCN). Previous research has demonstrated the utility of FSCN to detect corrosion events under polymeric coatings; however, direct correlation of the measured intensities to other methods have yet to be correlated to state definitively that fluorescein is monitoring corrosion events.[130, 132, 134-135, 137-138] Chapter V will show that FSCN is both sensitive enough and, even in low concentrations, accurately measures cathodic delamination compared to existing methods such as SKP.

FSCN exhibits seven different protolytic forms depending on the nature of the environment (protic vs. aprotic) and pH of the solution.[140] Figure 1.11 highlights each of the protolytic states that can be found for fluorescein, each with distinct pKas or solvent requirements to reach a specific conformation.[141] In an aprotic solvent, the lactone tautomer dominates, while when in protic solvent, the quinoid and zwitterion are more prevalent.[142] Upon decreasing the pH, the cation is formed, while increasing the pH results in the monoanion or dianion, depending on the pH of the solution.

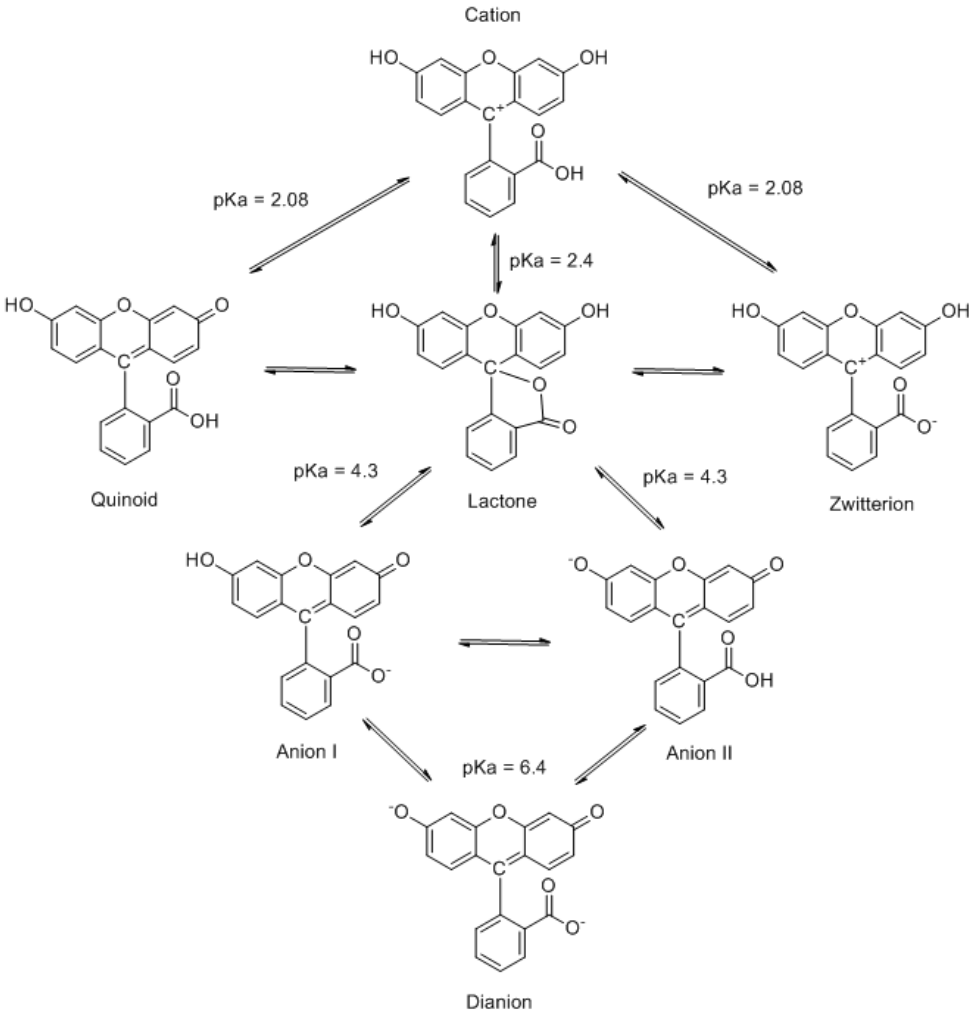

Figure 1.11 Fluorescein ionic states.[143-145]

pKa values listed are for aqueous solutions.

The visible and fluorescent response of FSCN to various solvents and pHs are highlighted in Figure 1.12. By altering the solvent and pH, the fluorescent response could be greatly altered, which indicated a need for consistent solvents for preparation of films.

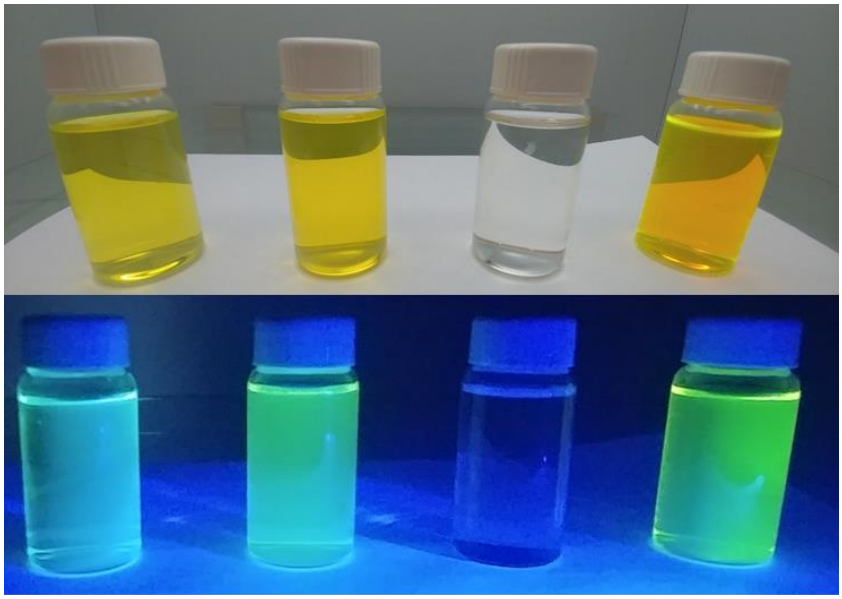

Figure 1.12 Visible and fluorescent response of fluorescein to different solvents and pHs. The neutral THF was anhydrous, while the methanol was HPLC grade. Acidification was performed using concentrated HCl. Basic methanol was prepared using N-morpholine.

Upon initiation of a corrosion event, the pH of the region around a defect increases due to the reduction of dissolved oxygen in water into free hydroxyl ions, causing an increase in the fluorescent intensity. While the monoanionic state is fluorescent, the quantum yield is low (0.37) compared to the dianionic state (0.93).[144] This indicates that both the mono and di anionic states will contribute to the measured intensities; however, the majority of the signal is derived from the dianionic species that formed. Again, model thermoplastic coatings provide a useful matrix to utilize FSCN. Due to the inherent amine basicity, an artificial increase in intensity is observed and the corrosion events masked if traditional epoxy-amine chemistries are used. However, upon successful quantification of cathodic delamination rates in the model thermoplastic used in Chapter V, the addition of fluorescein to other chemistries such as polyurethanes or

acrylates could be performed. This research only included FSCN into the thermoplastic epoxy-similar chemistries, as polyurethanes and polyacrylates are typically not utilized as primer coatings, and thus would not be in direct contact with the corroding metal substrate.

Although pH changes of corrosion events after immersion in solutions have been widely monitored, in situ pH monitoring has not yet been used effectively, especially when directly correlated to quantitative electrochemical corrosion measurements. Chapter V addresses this critical gap of fundamental relationships between two techniques and offers a solution to time-consuming electrochemical methods. Extending this knowledge to other polymeric binders can be easily accomplished, and further development of probe cocktails can be performed such that the anodic region could be monitored simultaneously.

CHAPTER II – MATERIALS AND METHODS

2.1 Materials

All resins, solvents, and fluorophores were used as received, without further purification. Metal substrates were primarily SAE 1008/1010 mild steel; however, hot-dip galvanized mild steel was utilized to determine the efficacy of fluorescence on a different substrate. The SAE 1008/1010 steel panels were supplied by Q Panel with a "Type R" finish (dull matte mill finish of 25-65 μ inches). The chemical composition of SAE 1008/1010 steel is listed in Table 2.1. The hot-dipped galvanized steel (Tata Steel) has a similar chemical composition but is plated with zinc, containing 0.15 wt% max aluminum. These substrates were polished with 5 μm aluminum oxide aqueous slurry to remove the oxidized zinc from the surface. Free films were created by casting on polished polypropylene which afforded easy release of the films after drying or curing. Glass slides were utilized as inert substrates, or when absorbance of bound films was needed.

Table 2.1 Elemental composition of SAE 1008/1010 steel.

Element	Max Weight Percent (wt%)
Manganese	0.60
Carbon	0.15
Phosphorus	0.030
Sulfur	0.035

Values represent the max weight percent present in the steel composition.

Additional experimental details can be found in Chapter III as it pertains to method development.

2.1.2 Model Thermoplastics

In order to compare model films to more complex coatings, Phenoxy® (Gabriel Performance Products) thermoplastic poly(hydroxyether) was utilized. This resin was a

linear thermoplastic diglycidylether of bisphenol A (DGEBA) that has been ring opened to form poly(hydroxyether)s comprised of secondary hydroxyls in place of the epoxide group (Figure 2.1). Three different molecular weights were used to measure the effect of conditionally specific glass transition temperatures and modulus has on corrosion processes and are shown in Table 2.2 with their corresponding T_g values as measured *via* DSC.

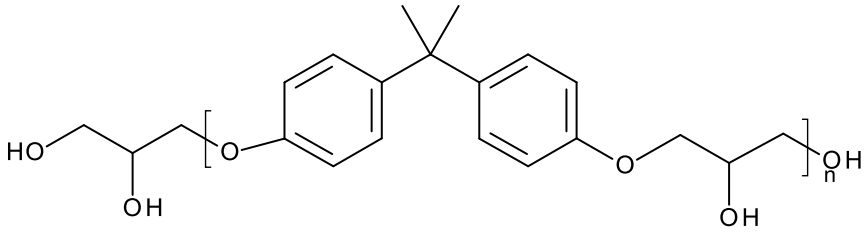

Figure 2.1 Primary structure of Phenoxy® PK series poly(hydroxyether).

Table 2.2 Molecular weights and corresponding T_gs of each Phenoxy resin.

Phenoxy Name	Molecular Weight (g/mol)	Tg (DSC, °C)
PKHA	25k	80
PKHH	52K	86
PKFE	60	97

A commercial acrylic resin (NeoCryl B-728) supplied as a solid powder was utilized as different chemistry, and was soluble in the same solvents utilized in this research. Neocryl B-728 is a copolymer consisting of methyl methacrylate and butyl methacrylate with a glass transition temperature of ~120 °C depicted in Figure 2.2.

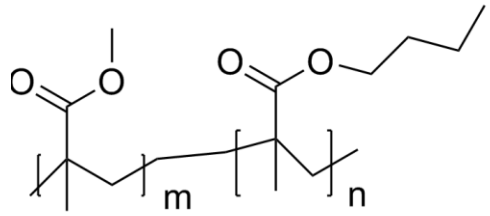

Figure 2.2 Neocryl B-728 primary structure.

In order to compare with other literature examples of fluorescent detection, Chapter V utilized poly(vinyl butyral) (PVB). This polymer was supplied as a poly(vinyl butyral-co-vinyl alcohol-co-vinyl acetate) because of the inherent difficulty in preventing hydrolysis during the synthesis. The molecular weight was 70,000-100,000 g/mol and supplied as a powder. Ethanol was utilized to solubilize the powder at 15 wt%, and the coating was drawn down at 25 ± 5 μm. The combined structure of PVB is depicted in Figure 2.3.

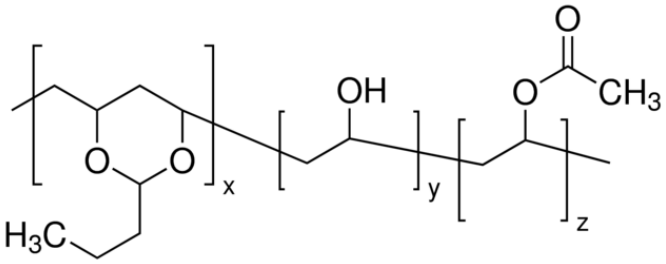

Figure 2.3 Structure of PVB as supplied by Sigma Aldrich.

2.1.3 Solvent Packages

Solvent-based resin solutions were prepared in accordance with their application method. Phenoxy® coatings for draw downs were formulated at 30 wt% resin solubilized in either ethyl 3-ethoxypropionate (EEP) or a blend of 2-butanone (methyl ethyl ketone, MEK) and 1-methoxy-2-propanol (PGME) in a 75/25 wt% mixture.

Spray applied Phenoxy® coatings were prepared by solubilizing 15 wt% resin in a blend of MEK (52.6 wt%), EEP (26.3 wt%), cyclohexanone (15.8 wt%), and propylene carbonate (5.3 wt%). The structures for each solvent are shown in Figure 2.4, with the boiling points, vapor pressures, and water solubilities listed below the structures. This solvent blend afforded a high flash primary solvent (MEK), two medium flash solvents (EEP/CyNONE), and a tailing solvent (PC) to aid in film formation.

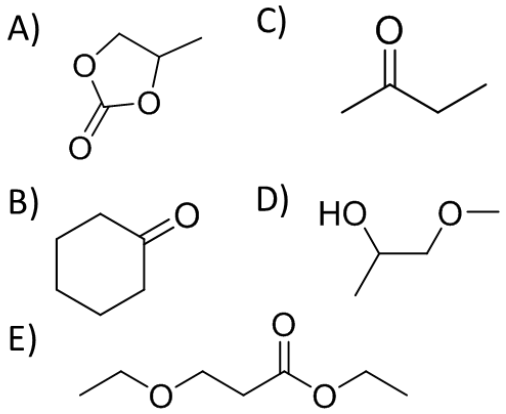

Solvent	Boiling Point (°C)	Vapor Pressure (mmHg)	Water Solubility (g/L)
PC	240	0.05	175
CyNONE	155	3.4	86
MEK	80	71	200+
PGME	118	10.9	200
EEP	166	1.7	54

Figure 2.4 Structure and corresponding properties of the various solvents used for solvent casting of poly(hydroxyether) resins.

A) propylene carbonate; B) cyclohexanone; C) MEK; D) PGME; E) EEP.

Several crucial performance differences were noted when a sample of one-year-old resin solution was utilized, which prompted an investigation into why a difference existed. The viscosity versus the shear rate of 30 wt% PKHH in MEK/PGME with two different age profiles is compared in Figure 2.5, and at low shear rates (<1 1/s), the aged

solution exhibited only one peak, whereas the new solution exhibited two. This difference was thought to be two slightly separate phases (i.e., MEK/polymer and PGME/polymer) resulting from incomplete homogenization. Upon resting for a length of time, these two phases better compatibilize and form a singular phase. Thus, only new solutions were used for consistency as the aged resin was prepared one year before the measurements. While the spray blend was composed of different solvents, it was not expected that it would display separate viscosities as the overall viscosity of the resin solution was so low, which afforded better mixing during preparation.

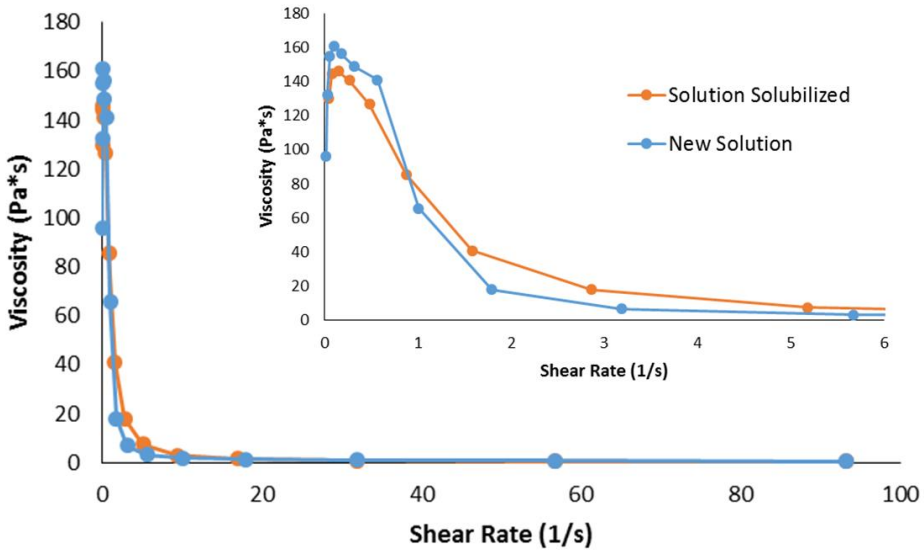

Figure 2.5 Viscosity versus the shear rate of 30 wt% PKHH in MEK/PGME

1 year old in can (solution stabilized) vs. a 3-day old mixture showing distinct low shear rate viscosity differences.

2.1.4 Commercial coatings

In Chapter III, a commercial MIL-SPEC coating at 75 ± 7 μm was utilized to minimize formulation issues and allow direct analysis of the scribe. DEFT Aerospace 02W053 (PPG), was a white chrome-free epoxy amine coating that contained zinc phosphate and was spray-applied.

In Chapter IV, a commercial MILSPEC water tank liner was used as a comparison to model coatings in order to afford comparisons between pigmented and non-pigmented coatings. This coating stack (V-766E) is an epoxy-polyamide and vinyl chloride-vinyl acetate copolymer that was spray applied and used at a dry film thickness of 240 - 250 µm (10 mils).

2.1.5 Fluorophores

Fluorescein (FSCN) was used as a pH-sensitive probe throughout this research. As depicted in Chapter 1, FSCN consists of seven distinct protolytic forms; however, the dianion is of most utility. Figure 2.6 indicates the absorbance and fluorescence spectra obtained from 10 µM FSCN in methanol. The boxed regions in Figure 2.6 highlight the regions of excitation and emission that were monitored during measurements.

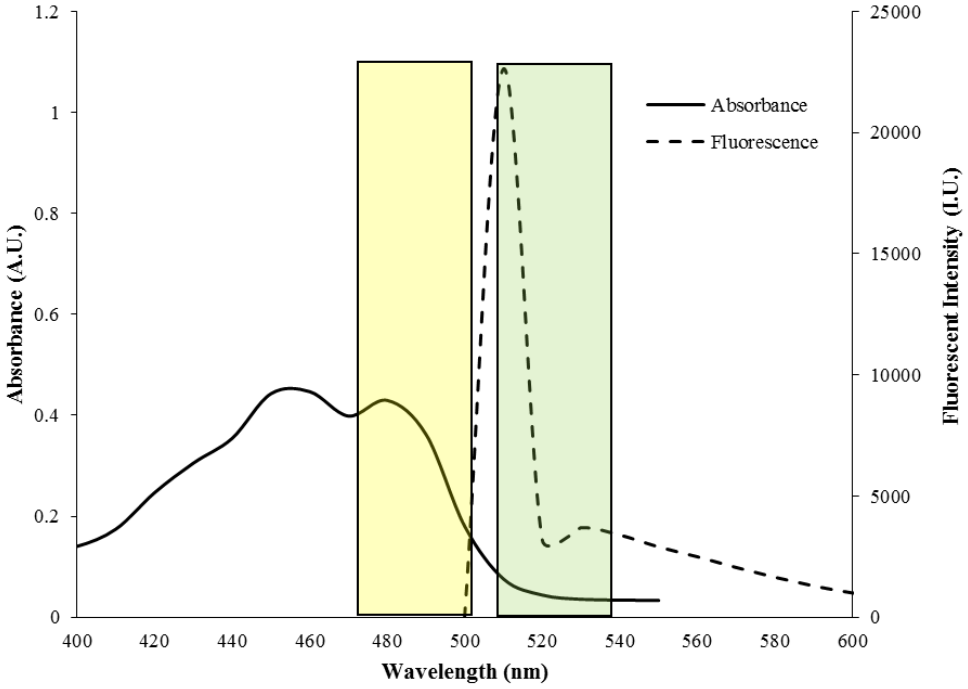

Figure 2.6 Absorbance and emission spectra for 10 µM FSCN in methanol.

Boxed regions denote the excitation and emission bandwidths

In the poly(hydroxyether) films, the absorbance and fluorescence spectra exhibit a blue shift, which puts the bandwidth of excitation and emission over the peak values. The broad bandwidth was an instrument limitation and could not be narrowed; however, the broadness of these regions ensured any shifts in the spectra would be captured. Furthermore, FSCNs various protolytic forms exhibit slightly different peak absorbance values, and by measuring a wider range, it was possible to capture the aggregated average of the speciation of FSCN in the measured signal.

Rhodamine B (RhB) was utilized as a pH insensitive probe as it resulted in a consistent fluorescent response up to approximately pH = 11. It is, however, affected by the solvent it is dispersed in. Thus there was a fluorescent increase with protic solvents similar to FSCN. The increase in fluorescence upon interaction with protic environments allowed for a direct comparison of water ingress into a film as both FSCN and RhB are affected by the protic nature of the environment. Upon reaching a saturation level with RhB in fluorescent signal, any additional increase in the fluorescent signal of FSCN is attributed to a pH increase. Figure 2.7 indicates the absorbance and fluorescence of RhB (10 μM) in methanol. The boxed regions denote the excitation and emission ranges that were measured.

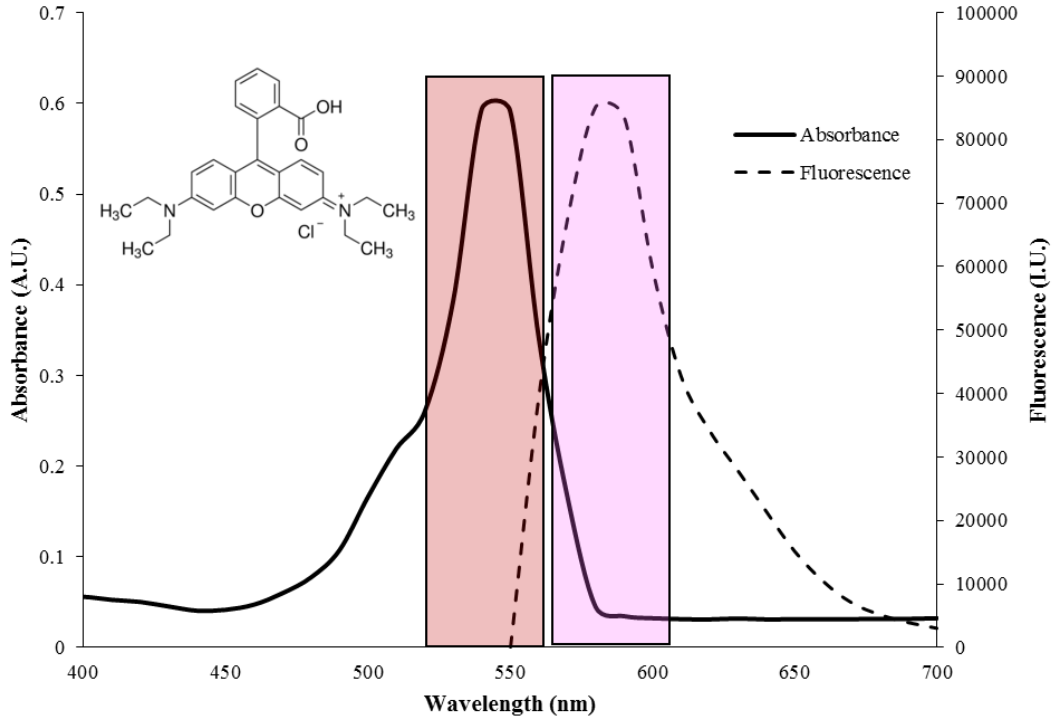

Figure 2.7 Absorbance and fluorescence spectra of 10 μM RhB in methanol.

The boxed regions denote excitation bandwidth (left) and emission bandwidth (right)

Water ingress was detected using a third fluorescent probe, 8-hydroxypyrene-1,3,6-trisulfonic acid trisodium salt (HPTSA), of which the absorbance spectrum and structure are depicted in Figure 2.8. Upon water infiltration into the polymeric film, HPTSA aggregates in the water phase, causing a fluorescent signal increase, indicated in Figure 2.9.

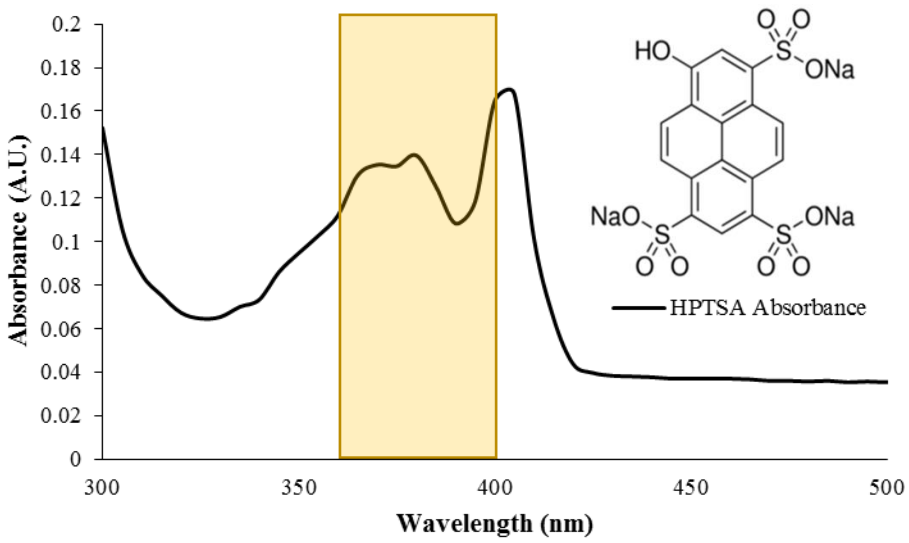

Figure 2.8 The absorption spectrum for 10 μM HPTSA in PGME.

Boxed region indicates the excitation bandwidth utilized.

Excitation was performed at 380 nm while monitoring the response of additional water content from 400 700 nm. HPTSA exhibited a reduction in the intensity at ~415 nm and an increase in the intensity at ~510 nm. Due to the response obtained after incorporation into the polymer, the fluorescent increase was monitored at 510 ± 20 nm.

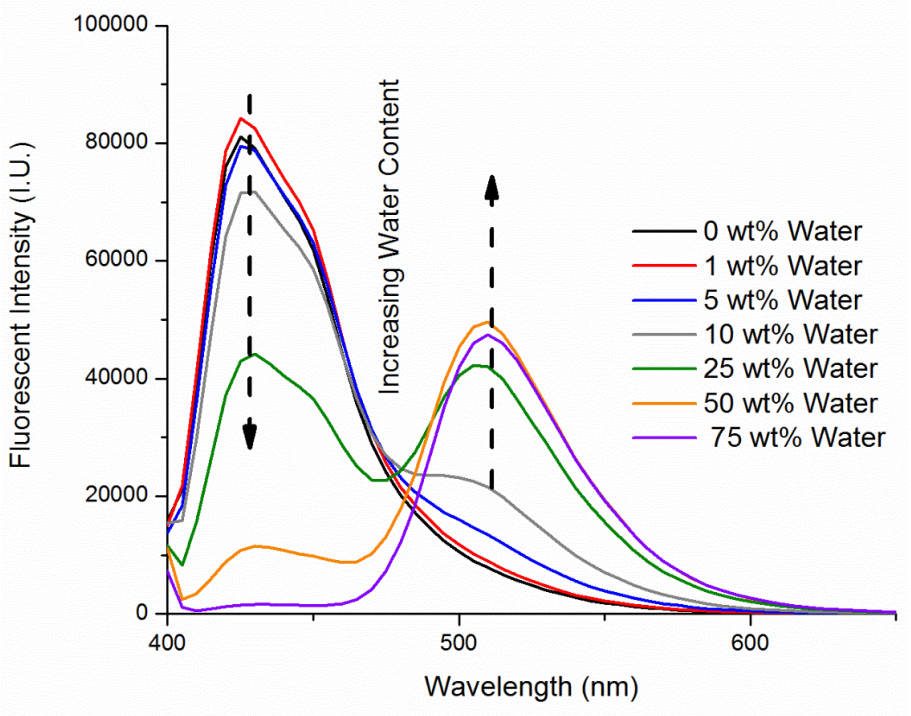

Figure 2.9 HPTSA fluorescent response curves upon addition of water into the solvent. HPTSA was only in the solvent phase. Therefore there is a decrease in the amount of HPTSA with increasing water content; however, the intensity is still appropriately mirrored with the addition of water.

2.2 Drop-on-demand printing

Drop-on-demand printing or inkjet printing is a precise method to control the spatial positioning of desired materials in ceramic depositions,[146-153] electronic applications,[150-152, 154-160] biological materials,[161-163] and more.[164-167] In the corrosion science field, this type of spatial control is desirable for the precise placement of contaminants, inhibitors, or sensors within a coating system.

Drop-on-demand printing was performed using a MicroFab Technologies Inc. single head inkjet printer outfitted with a 120 μm tip. A resin blend consisting of 1 wt% PKHH solubilized in a 75/25 w/w mixture of EEP and benzyl alcohol (BzOH) was used as a carrying fluid for the fluorescent probes in order to ensure adhesion to the substrate.

A viscosity versus wt% resin curve was generated to determine the max wt% printable by viscosity considerations (Figure 2.10). With the MicroFab printer, 5 wt% was the maximum solution concentration that remained printable; however to ensure printing was consistent, 1 wt% PKHH was utilized.

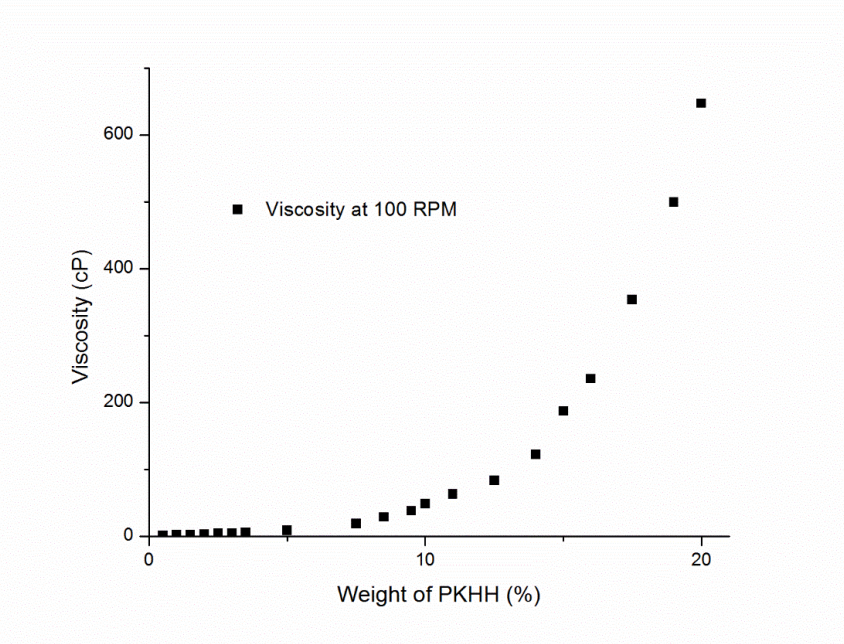

Figure 2.10 Viscosity profiles vs. weight % PKHH in EEP/BzOH for printing.

Printing was performed using a custom text script in which gridlines formed a 5 x 5 mm gridded surface for facile measurements. The piezo wave parameters were as follows: a 3 μs rise, 30 μs dwell time at 35 volts, 3 μs fall, a 30 μs echo time at -35 volts, followed by a 3 μs echo rise, depicted in Figure 2.11. The frequency of the print head was set at 300 Hz. This set-up produced a square wave that yielded consistent print results and a schematic is depicted in Figure 2.11.

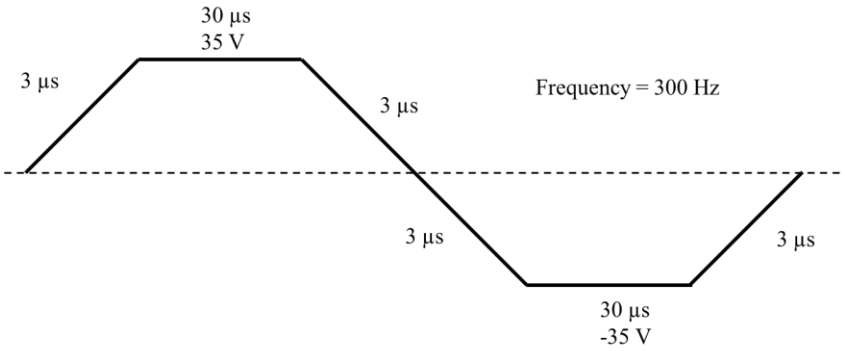

Figure 2.11 Square wave-form utilized for inkjet printing.

The results of the grid printing are described in Figure 2.12. The grid printed at the surface was visible through the overcoated film due to the different wavelengths of excitation and emission between FSCN and RhB. Chapter V utilized this method of sample preparation for facile area measurements.

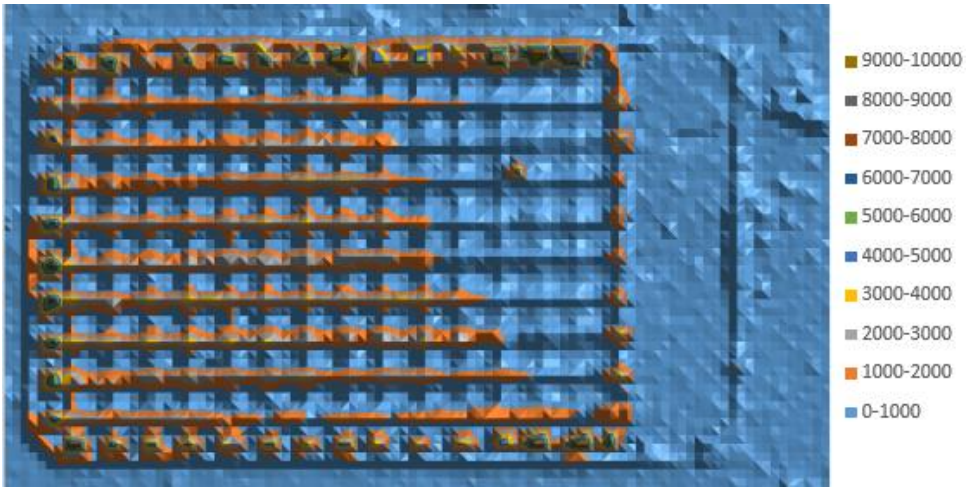

Figure 2.12 Fluorescent signature of an over-coated, printed grid composed of PKHH and RhB for analysis on a steel panel.

Each grid square is 5 mm x 5 mm.

2.3 Accelerated Corrosion Testing

Two separate accelerated corrosion tests were used to determine cyclical testing and salt content and type impact on the corrosion performance of various coatings and

additives. All panels were back and edge tape-masked to limit corrosion to the face of the coated steel coupon. Samples were scribed with a vertical line down the center of the panel using a 350 μm burnishing tool. Additional details regarding tool selection can be found in Chapter III. ASTM B117 salt spray was used as an accelerated corrosion test. This method continually sprays 5% NaCl solution at a temperature of 35 °C. Metal coupons were placed in the chamber at 45° angles to prevent liquid accumulation from occurring on the surface. Samples were removed periodically, rinsed with DI water, and imaged before continuing the weather test.

GM14872 system consists of three distinct steps within one cycle: 1) a three minute salt spray comprised of 0.9 wt% NaCl, 0.1 wt% CaCl2, and 0.0075 wt% NaHCO3 during which time the chamber is held at 25 °C and 45 %RH for eight hours; 2) a one hour ramp to 49 °C and 100 %RH, held for eight hours; 3) a three hour ramp to a dry stage at 60 °C and 25 %RH, maintained for 8 hours. Again, the coated metal coupons were placed into the chamber at a 45° angle to prevent liquid accumulation on the surface.

In order to monitor the corrosion visually, high definition images were measured using the measurement analysis tool within Adobe Pro suite to quantify the area covered by corrosion across the exposed surface. A representative image is shown in Figure 2.13. The area between the red lines was the measured area considered corrosion. The light orange/yellow regions outside of the dark area were stained due to wash-off during accelerated corrosion.

Figure 2.13 Representative corrosion area measurement.

The sample was exposed for 2,000 hours to ASTM B117. Image analyzed in Adobe Pro.

2.4 Methods

2.4.1 ATR-FTIR

Model polymer solutions were spray applied to the thermally-controlled Durasampler™ test plates including over the diamond ATR crystal, annealed under varying conditions as described above, and used to directly measure the diffusion coefficient of water sorption using an iC10 ReactIR system from Mettler Toledo. Coatings were challenged with either DI water, 5% NaCl, or GM 14872 solution at 25 °C to observe the real-time sorption of the challenge solution from the substrate interface of the coating material. Using the equation from Fieldson and Barbari, water sorption was calculated as the total saturation within the polymer film (Equation 4).[168]

$$\frac{A_t}{A_\infty} = 1 - \frac{8\gamma}{\pi[1-\exp(-2\gamma L)]} \cdot \left[\frac{exp\left(-\frac{D\pi^2 t}{4L^2}\right)\left(\frac{\pi}{2L}\exp(-2\gamma L)+(2\gamma)\right)}{\left(4\gamma^2+\frac{\pi^2}{4L^2}\right)}\right] \qquad \text{Equation 4}$$

where A_t is the concentration at time t and A_∞ is the concentration at saturation equilibrium. The film thickness is represented by L in cm, and the depth of penetration for the ATR effervescent wave is represented by γ (Equation 5).[168-169]

$$\gamma = \frac{\lambda}{2\pi n_2\left[sin^2\theta - \left({}^{n_1}/_{n_2}\right)^2\right]^{1/2}}$$ Equation 5

where n_1 is the refractive index of the rarer medium (polymer), n_2 is the refractive index of the propagating medium (diamond), θ is the IR angle of incident (45°), and λ is the IR wavelength in μm. Since the sorption kinetics of water within the polymer film were measured below 0.5 of saturation (linear region of the initial sorption curve), Equation 3 was simplified to calculate the slope of diffusion for all penetrant solutions into the coating (Equation 6).[168-169]

$$\ln\left(1 - \frac{A_t}{A_\infty}\right) = \ln\left(\frac{4}{\pi}\right) - \frac{D\pi^2}{4L^2}t$$ Equation 6

With Equation 6, the value for the diffusion coefficient, *D,* was calculated from the absorbance data as a function of time using linear least squares regression of the IR sorption logarithm slope below 0.5 saturation. Only samples with 14 wt% - 6 wt% residual solvent were capable of being measured utilizing this method as temperatures above 80 °C to drive additional solvent loss could damage the equipment.

2.4.2 Internal stress measurements

Metal strips (12 mm x 102 mm) were cut from 0.1 mm thick 304 stainless steel (304SS) strips and prepared as per ASTM D6991. Coatings were applied via air-assisted spray while restraining the metal strips with an adhesive tape (target dry film thickness 40 μm). The deflection of coated strips caused by drying, volume change, and in response to wet and dry cycles was monitored optically utilizing a digital camera array comprised of four Vision HAWK Smart Cameras. The wide field of view in the digital cameras enabled the simultaneous measurement of five samples per camera. Adobe Photoshop

was employed in conjunction with InduSoft Web Studio and Microscan AutoVISON programs to automate the data acquisition. A typical single cantilever beam apparatus is illustrated in Figure 2.14.

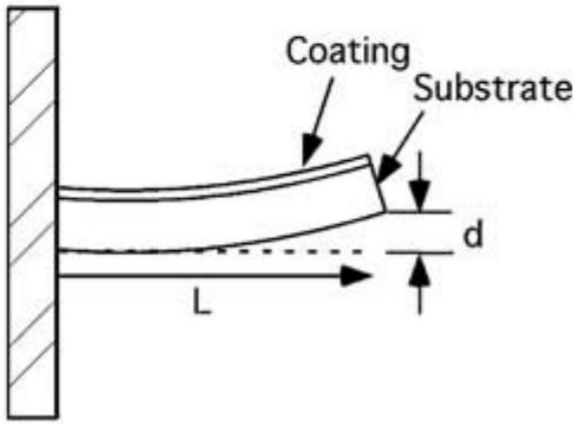

Figure 2.14 Typical single cantilever beam apparatus for internal stress.

A measurement reference was used within the sample cells to adjust for the field of view distortions. Internal stress (*S*) of the coating was calculated from the deflection of the coated strip using Equation 7.

$$S = \frac{hE_s t^3}{3L^2 c(t+c)(1-\gamma_s)} + \frac{hE_c(t+c)}{L^2(1-\gamma_c)} \qquad \text{Equation 7}$$

Where E_s, is the substrate elastic modulus (1.93 x 10^4 MPa for 304SS), γ_s is substrate's Poisson ratio (0.25 for 304SS), t is the substrate thickness, L is the measured length to deflection (80 mm), c is the coating thickness, E_c is coating's elastic modulus, and γ_c is the coating's Poisson ratio. If the coating thickness is less than half of the substrate thickness, the elastic modulus and Poisson's ratio in the second part of Equation 7 are rendered negligible, which is beneficial as γ_c is difficult to determine for a formulated coating. At the specified thickness, the films would fall into this design parameter.

Negating the second term in Equation 7 results in Equation 8, which was utilized for the internal stress evaluations in this research.

$$S = \frac{hE_s t^3}{3L^2 c(t+c)(1-\gamma_s)} \qquad \text{Equation 8}$$

2.4.3 Optical transparency measurements

The degree of whitening, or opacity, was measured using a BioTek Synergy Neo multi-mode plate reader in absorbance mode from 300 - 800 nm in 100 nm increments every 2.5 minutes for 24 hours.[30] To measure the change in film transmittance, 6 mm disks were punched from a free film and placed into the bottom of clear 96 well plate and covered with 300 μL of DI water.

2.4.4 SEM analysis

Scanning electron microscopy (SEM) was performed utilizing a Zeiss Sigma-VP field emission scanning electron microscope at 10 keV acceleration voltage at working distances of 2 - 5 mm. Each film was cryo-fractured in liquid nitrogen to expose the cross-section, followed by sputter coating utilizing an Emitech K550X equipped with a silver target. All images are representative of the sample and represent the average characteristics of the entire sample.

2.4.5 Fluorescent analysis

In order to measure the fluorescent intensity, a BioTek Synergy Neo microplate reader was utilized. This instrument is capable of performing both the absorbance and fluorescent measurements rapidly. Absorbance measurements of the fluorescent probes in the appropriate solvent were performed to determine the correct excitation wavelength. In the case of fluorescence, it is desirable to excite the molecule at the peak absorbance,

as more energy is absorbed by the fluorophore. A spectral sweep was performed on coated metal substrates with an excitation equal to that of the greatest absorbance value to determine the peak emission wavelength. In doing this method, the instrument only needs to monitor one emission wavelength, increasing the throughput capabilities.

A custom designed script was utilized, measuring 6400 points in a uniwell plate. This script leads to a 1.17mm x 1.16 mm cell size in the array, with a beam width of 1 mm. By utilizing this cell size, the resolution was maximized without beam overlap, which can cause excitation of already measured regions. Each spot was measured three times, of which the excitation was averaged and is the reported value herein. The total area measured was the size of a 2" x 3" steel coupon, meaning the entire panel was scanned within 15 minutes.

2.4.6 Scanning Kelvin Probe

A custom-built scanning Kelvin probe (SKP) was utilized to conduct cathodic delamination rate measurements. This SKP was equipped with a 125 μm gold wire, vibrated normal to the sample surface at an amplitude of 50 μm and a frequency of 280 Hz. The sample stage was equipped with 3-axis micromanipulators to scan an area, with measurements performed every 50 μm. The SKP scanned at the height of 100 μm from the sample surface, resulting in ~140 μm spatial resolution. For PVB films, a Stratmann geometry was utilized (Figure 2.15). This geometry consisted of the creation of a well at one end of the coated steel substrate that was filled with water and allowed the electrolyte to access the substrate directly.

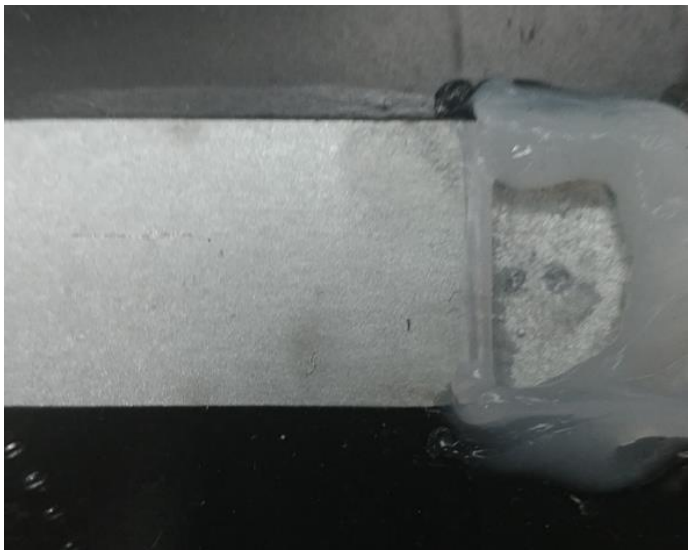

Figure 2.15 Example of the Stratmann geometry used for a cathodic delamination cell.

Well that contained the electrolyte is on the right while cathodic delamination progresses to the left.

Films comprised of poly(hydroxyether) were too brittle to create the Stratmann geometry; therefore, a defect was induced with a razor blade, challenged with 2 μL of 5% NaCl and scanned after the sample was conditioned for 1 hr at ~95% relative humidity (RH). Scans were performed every 2 hours for 24 hrs, while the atmosphere of 95% RH and 20 °C were maintained.

2.4.7 Thermal Analyses

2.4.7.1 Relative Humidity-DMA

Relative humidity DMA (RH-DMA) was performed to determine the polymeric film's response to increased humidity. Measurements were conducted using a TA Instruments Q800 DMA at a strain of 0.1% and a frequency of 1 Hz. Free standing films were first conditioned at 25 °C for one hour at the desired relative humidity (0 and 95%), followed by cooling to 5 °C. After cooling, stabilization at 5 °C was held for five minutes followed by heating at 1 °C/min to 120 °C.

2.4.7.2 DSC

In order to measure the glass transition temperature (Tg) of the polymer, DSC was performed utilizing a TA Instruments Q2000 DSC. Samples were prepared by weighing out ~8 mg of the film *via* punch outs and sealing into hermetic pans. The procedure was a heat-cool-heat cycle in order to eliminate the thermal history of the polymer before measuring the Tg. A heating rate of 10 °C/min and a cooling rate of 5 °C/min was utilized in both sealed and punched pans to determine the effect of exposures and residual solvent, followed by allowing the contaminants to evaporate, respectively.

2.4.7.3 TGA

Thermogravimetric analysis was conducted to determine the amount of residual solvent in the film after drying, and annealing had occurred. A TA Instruments Discovery TGA was utilized in high-resolution dynamic mode at a heating rate of 10 °C and an air atmosphere up to 600 °C. The amount of residual solvent was determined by taking the mass at 250 °C, which was above the boiling point of each solvent constituent used, but below the polymer decomposition temperature.

CHAPTER III - DEVELOPMENT OF STANDARDIZED SCRIBING TEST METHOD FOR ACCELERATED CORROSION TESTING

3.1 Objective

The objective of this chapter was to elucidate the effect of scribing tools and parameters on visual corrosion assessments during two separate accelerated weathering techniques to offer a reproducible methodology that used throughout the other chapters.[170] It was hypothesized and verified that wider scribing tools resulted in greater visual corrosion product. If this hypothesis is thought of in terms of an induction period, then by utilizing wider scribes, the induction period would be diminished as macroscopic changes were observed earlier. Noteworthy, these methods provide very little new understanding of how films without an intentional defect perform or the mechanistic reasons for performance differences between scribed and non-scribed samples. These data resulted in a unified scribe analysis method, by which any tool type can be utilized, and inter-correlated to other tools based upon the original scribed area. If the scribe region is appropriately characterized, accounting for the metal exposed during the scribing process, these coating systems can be quantitatively compared, as the corrosion mechanism will remain unchanged in the absence of inhibitors. While ASTM standards recommend different tool types, this research validated the premise that tool types greatly influence visual corrosion measurements and unnecessarily complicate comparisons.

3.2 Additional experimental details

While much of the experimental details remain similar to the rest of this document, this section will highlight critical differences used to determine the correct scribing parameters for accelerated corrosion measurements.

Two separate techniques were used to mimic the typical means of inducing an intentional defect: manual and mechanical. Manual tools included a standard hobby razor blade (Razor), a carbide scribing pen (Carbide), and a commercial brass padlock key (Key). The mechanical scribing utilized a consumer engraving system (Vision Express; Vision Engraving and Routing Systems, Phoenix AZ) equipped with the following scribe head geometries: 90° and 120° diamond drag tips (90DD and 120DD, respectively), and 200 and 350 μm wide carbide burnishing tips (200B and 350B, respectively) at two distinct scribe rates of 25 and 100 mm s^{-1} denoted as 'S' and 'F', respectively. This variation in the scribe rate allowed for a greater number of spindle rotations per length of material as the spindle rotated at a constant 12k RPM resulting in a smoother scribe on the metal substrate. Samples were scribed with a single, vertical defect (65 mm long) along the center of the panel for ease of analysis and clarity of observation. A set of triplicate panels without a scribe were used as controls for each weathering chamber. Scanning electron microscopy images of each tool's cutting edge are shown in Figures 3.1-3.3.

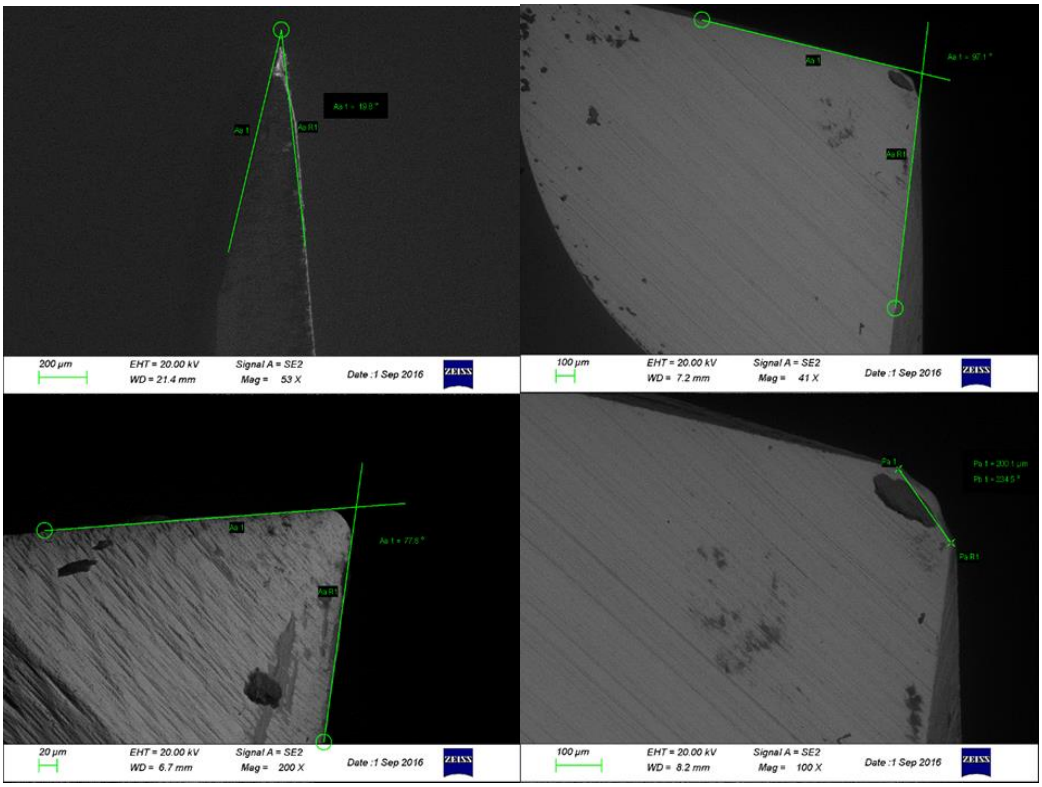

Figure 3.1 SEM micrographs of a razor, carbide pen, and 200B tip.

Razor blade tip (top left), carbide scribing pen (bottom left), and the 200B tip and width (right, top and bottom, respectively).

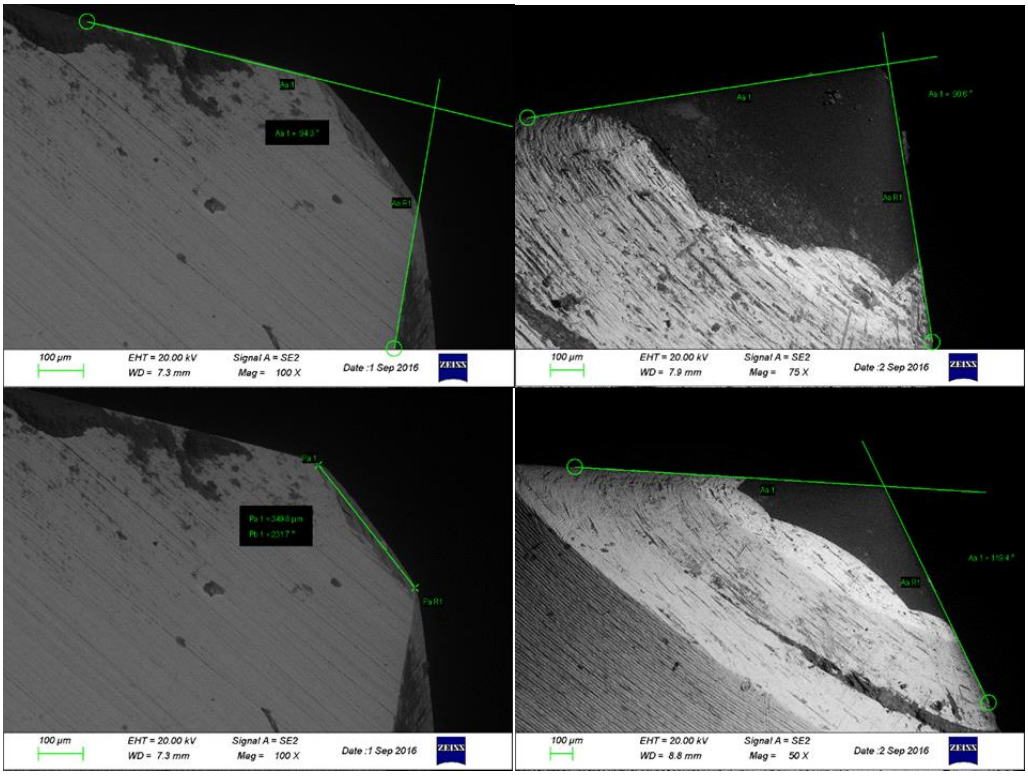

Figure 3.2 SEM micrograph of the 350B, 90DD, and 120DD tools.

350B tip and width (left, top and bottom, respectively), 90DD tip (top right), and 120DD tip (bottom right).

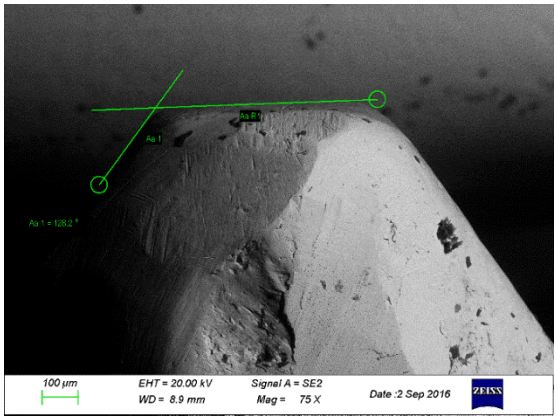

Figure 3.3 SEM micrograph of the key cutting surface.

The key used was a common brass padlock key. The image shown is the cutting surface used.

3.3 Results and Discussion

3.3.1 Scribe profiles prior to exposure

Figure 3.4 depicts three distinct zones that can be classified after scribing was performed. While this represents just one coating, this same trend was observed on all coatings that were scribed. Zone I is the unperturbed coating or the coating that visually demonstrated no influence of the scribe. Zone II, or the region between the dashed lines in Figure 3.4, is the disrupted region, whereby the scribe tool caused a visual change in the film while Zone III (the region between the dotted lines) refers to the area from which the coating was removed. The impact of these three regions was analyzed using Tukey's post-hoc analysis and a one-way ANOVA for statistical relevance, and it was determined that the disrupted region had little relationship with the observed corrosion.

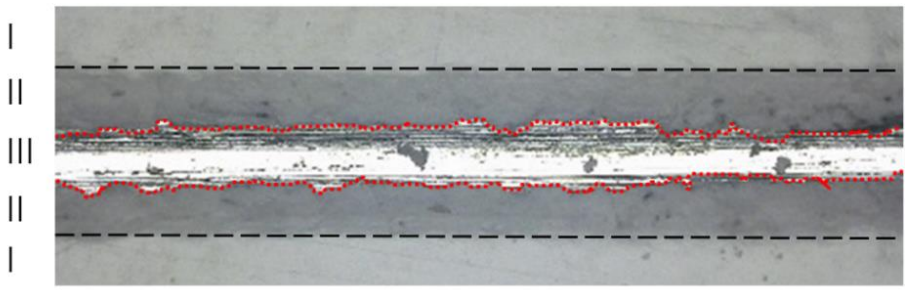

Figure 3.4 Representative scribe regions prior to exposure.

Three distinct zone can be classified: Zone I is the unperturbed coating, Zone II is a damaged or disrupted region, while Zone III is the bare metal due to the coating removal. Only Zone III was used in the initial area measurements.

Table 3.1 lists the diameter and cross-section, the angle of the cutting tool, and the roughness profile after intentionally creating a defect in the coating. The roughness profiles were analyzed using a one-way ANOVA, and again, there was little correlation between the roughness of the defect and the corrosion rate that was measured. The

diameter and cross section and angle of the tool were characterized by SEM analysis, while the roughness was measured using laser profilometry.

Table 3.1 Engraving type, diameter/cross-section, angle, and resultant roughness of the defect.

Tool	Engraving Type	Diameter/Cross Section (μm)	Angle (°)	Sq (μm)	Rsm_l (μm)	Rsm_w (μm)
Razor	Manual	11	9	0.40	35	8
Carbide		31	78	0.92	78	22
Key		630	71	1.24	33	16
90DD	Mechanical	100	90	0.58	42	19
120DD		150	120	0.76	151	26
200BS		200	97	0.95	71	15
200BF				0.92	66	7
350BS		350	94	1.85	109	14
350BS				0.87	63	23

The manual engraving was performed with hand tools, while mechanical engraving was performed with an automated scribe instrument. Diameter/cross-section and angle were determined from SEM micrographs, Roughness was determined with optical laser profilometry. Sq was the RMS roughness of the area within the scribe, Rsm_l was the roughness profile down the scribe, and Rsm_w was the roughness across the scribe.

In Figure 3.5 and 3.6, little correlation between the scribe depth and disrupted zone width, respectively, and the one-year corrosion predicted from the rates obtained experimentally, was observed. A one-way ANOVA resulted in a p-value > 0.05, which statistically indicated scribe depth and the disrupted zone width mattered very little on the measured corrosion rate.

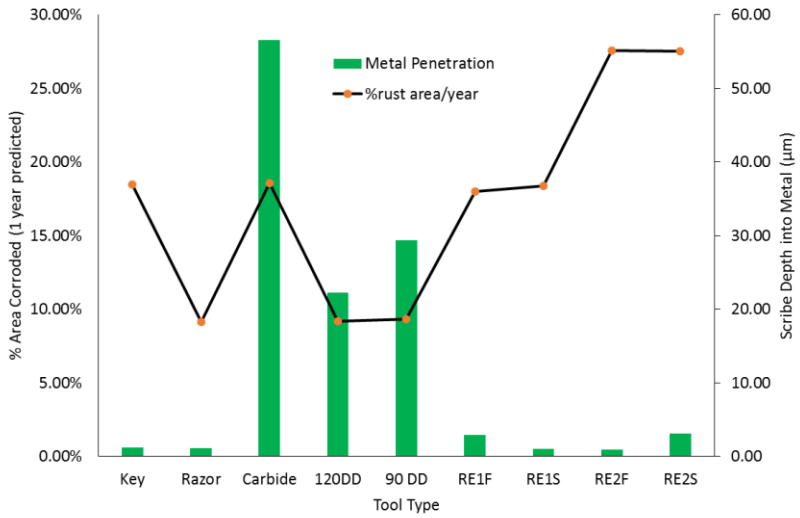

Figure 3.5 Percent of total panel corrosion predicted after 1 year and scribe depth comparison.

The percent of the total corrosion area was predicted using the corrosion rates obtained from experimental data and represent an extrapolation to one year, indicated by the solid line. The bars represent the depth of metal penetration reached by each tool type.

It was expected and confirmed that the amount each scribe tool penetrated into the metal did not correlate well with observed corrosion results. In the case of an artificial defect, the polymer needs to be simply removed from the substrate. It was believed that further penetration into the metal provides an accumulation site for electrolyte and additional exposed metal; however, the rapid oxidation of the raw exposed steel would seal the defect and hinder access for further corrosive materials. As the oxidation is rapid, the corrosion product does not alter the amount or differences of polymer at a delaminating zone.

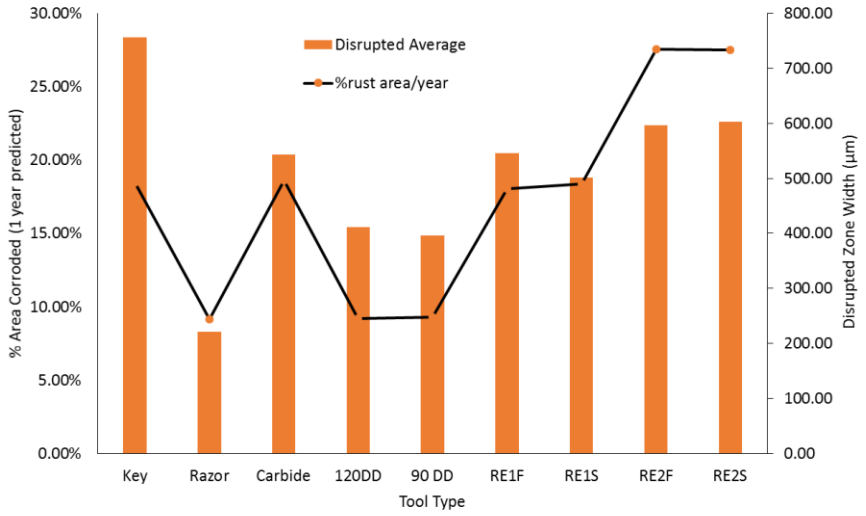

Figure 3.6 Percent of total panel corrosion predicted after 1 year and disrupted region comparison.

The percent of the total corrosion area was predicted using the corrosion rates obtained from experimental data and represent an extrapolation to one year, indicated by the solid line. The bars represent the disrupted zone width induced by each tool type.

Unexpectedly the disrupted region unexpectedly did not contribute to the corrosion product statistically. It was expected that this area would exhibit a decreased adhesion due to mechanical disruption of the coating, which would exacerbate the corrosion progression. However, if the interfacial transport of electrolyte is rapid, then the area around the scribe would be immediately inundated with corrosive electrolyte. Thus, by this rapid transport, it would make sense that the disrupted region would not impact the corrosion measurements.

The average scribe width, average disrupted region, and average depth of metal penetration are shown in Figure 3.7A and B. By using a wide variety of tools, a representative distribution of scribe widths and penetration into the metal substrate was achieved to characterize the visual performance accurately. While the depth of

penetration was not controlled, suitable distributions of depths were achieved to determine statistically if the corrosion rate was influenced by depth.

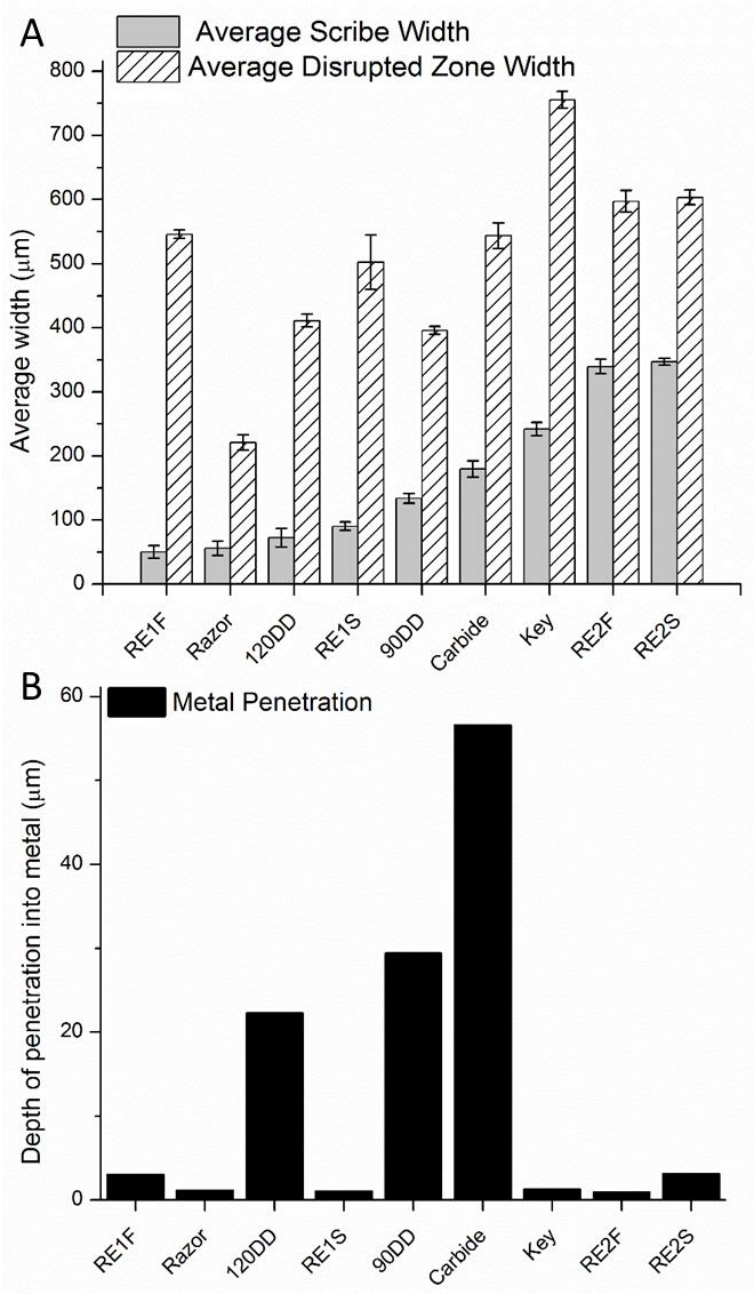

Figure 3.7 Average scribe width, disrupted region, and depth of metal penetration.

A) average scribe width and disrupted region, B) average depth of metal penetration. Error bars are 1 standard deviation from the triplicate mean.

Each of the variables in Figure 3.7 were chosen as it was expected that they would impact quantifiable measurements during the traditional “induction period” associated with the coatings before visual corrosion was measurable. However, this chapter's results validated that the disrupted region and depth of metal penetration at the scribe can be eliminated as characteristics that affect corrosion measurements for film related accelerated corrosion performance. Provably, the scribe width was determined to have a direct impact on the induction period and subsequent corrosion rates as measured visually and yet the results reported herein provide a path to normalize results of common scribe types by normalizing to the original scribe area relative to the total coating area.

Figures 3.8 and 3.9 are the representative profiles that resulted from the manual and mechanical scribing tools, respectively, before exposure *via* laser profilometry. All images are 644 x 644 μm in x and y dimensions and the color scale for all scans, in the case of these data, are relative to the lowest measured point, including substrate topographical variations. The width of the resulting profile from the key (Figure 3.8C) was significantly larger than that of the razor or carbide pen; however, it was similar to that of the profiles from 350B. The razor and carbide pen (Figure 3.8A and B) both exhibited similar scribes to the 90DD and 120DD mechanical scribes (Figure 3.9A and B). Several of the tools exhibited sloughing of material into the surrounding regions. It was also observed that the removal of the coating from the substrate was dictated by the material feed rate for the 200B and 350B spindles (Figure 3.9C - F). The surface of the exposed metal was less perturbed for 200B at 100 mm s^{-1}, whereas 350B exhibited less perturbation at 25 mm s^{-1}. This difference is most likely a factor of the concentration of force relative to the material feed rate during the scribing process.

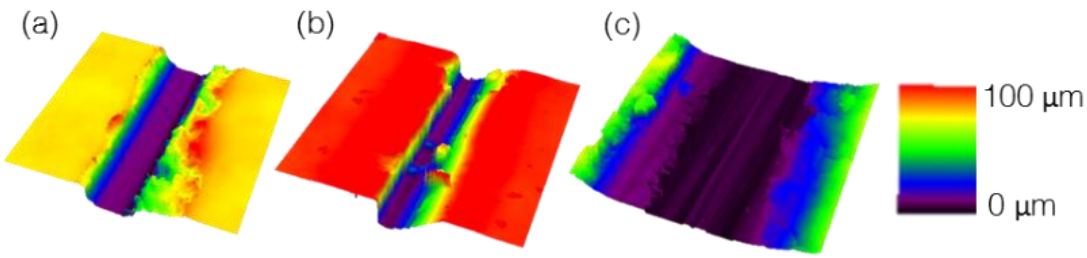

Figure 3.8 Optical surface profile scans of manual tools.

Representative laser profiles resulting from the manual scribing tools: (a) Razor; (b) Carbide; (c) Key. All images represent a scanned area of 644 µm x 644 µm.

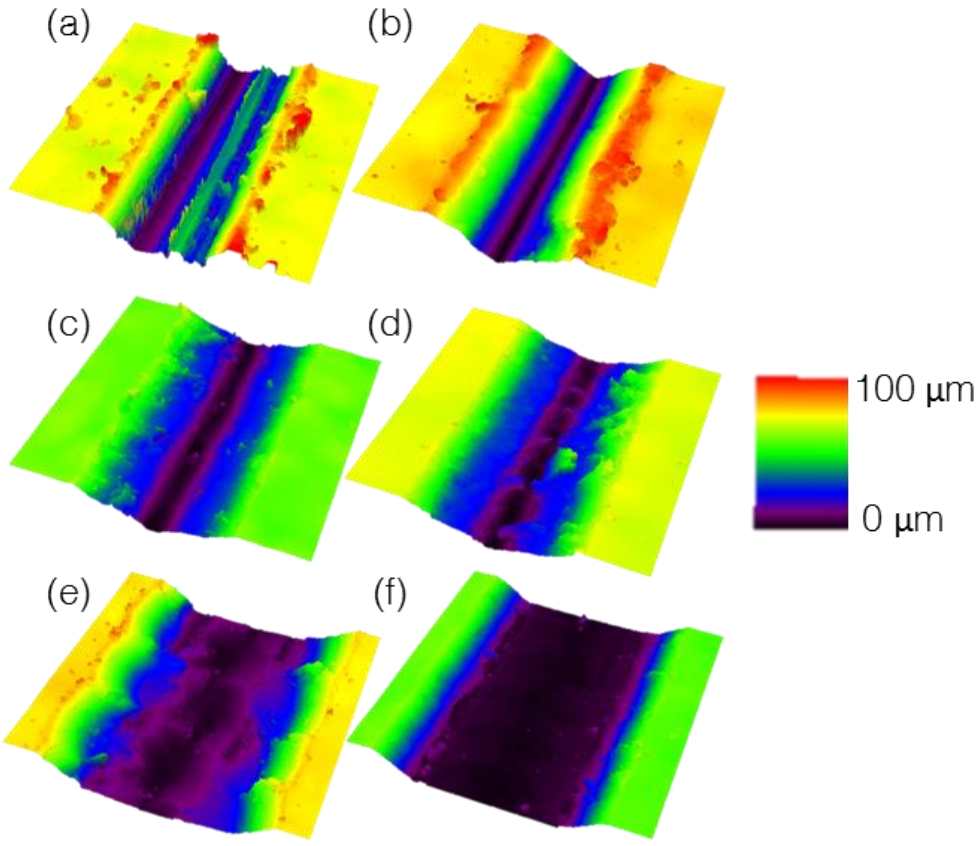

Figure 3.9 Optical surface profile scans of mechanical tools.

Representative laser profiles resulting from the mechanical scribing tools: (a) 90DD; (b) 120DD; (c) 200BF; (d) 200BS; (e) 350BF; (f) 350BS. All images represent a scanned area of 644 µm x 644 µm.

3.3.2 Arrhenius relationships for exposure conditions

The Arrhenius behavior of electrolyte penetration via IR was compared in Figure 3.10 where the measured diffusion coefficients at five temperatures for each chamber's electrolytes and standard DI water were plotted. The activation energy for deionized water transport through the polymer film was measured at 79 kJ/mol K. Activation energy of 5% NaCl-water transport was measured at 70 kJ/mol K. Activation energy of GM14872 solution, containing $CaCl_2$, NaCl, and $NaHCO_3$ transport in the polymer film was measured at 61 kJ/mol K. These differences in activation energies were likely the direct result of different salt ions in the challenge solution and their interaction with both the 02W053 coating and water.

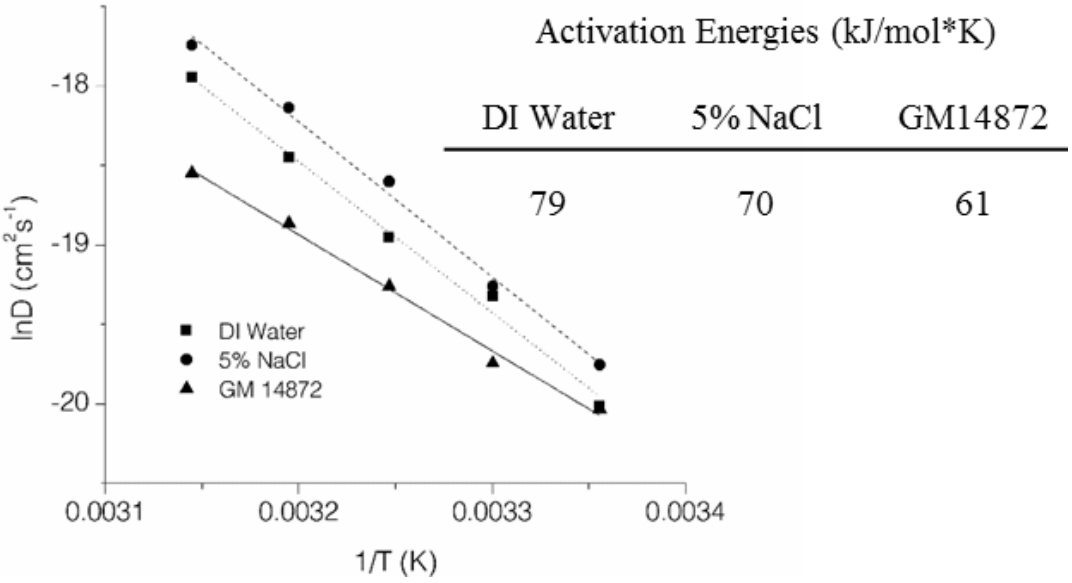

Figure 3.10 Arrhenius relationships and activation energies of exposure conditions.

Arrhenius behavior of each exposure condition and their corresponding activation energies in kJ/mol*K.

The common ions between the two method chambers were Na^+ and Cl^-. GM14872 chamber solution used a lower concentration of NaCl but also had $CaCl_2$ and $NaHCO_3$. The rate of water sorption into the film of DI water was slower than those with

salt, but had a much higher saturation equilibrium, as shown in Figure 3.11. The absence of salt in the water prevented a more organized water structure and resulted in more significant interaction with the polymer film, slowing the rate of diffusion. Conversely, the presence of salt in the exposure solution competitively interacted with the water, diminishing the direct water and salt interaction with the polymer, resulting in a faster diffusion rate. Furthermore, the interaction of the water with the salt and not the polymer resulted in a decrease in polymer relaxation/swelling limiting the saturation concentration within the polymer coating.

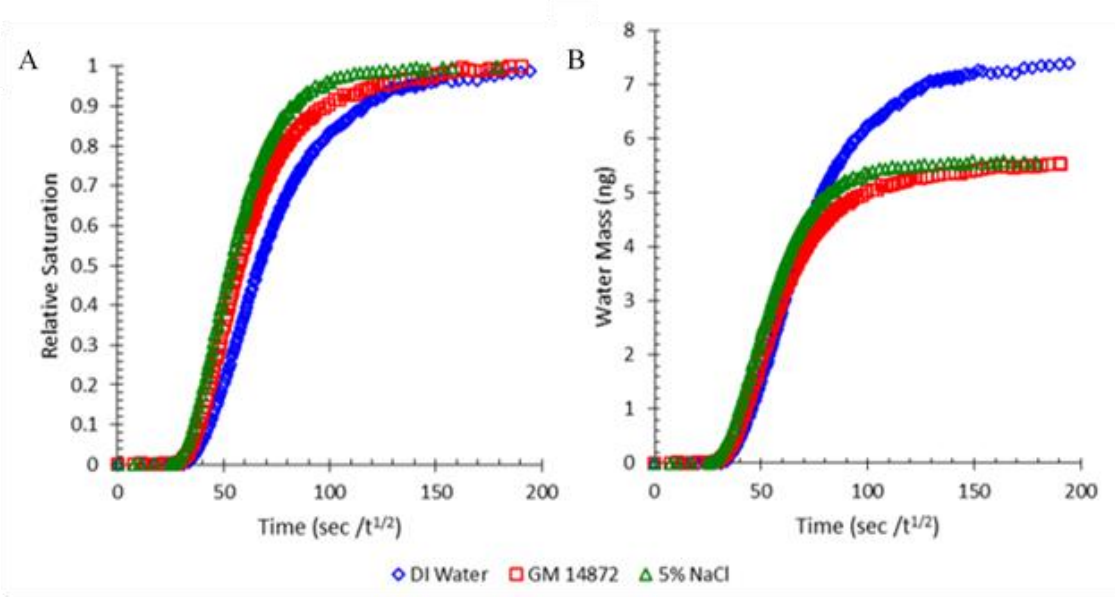

Figure 3.11 The rate of sorption and saturation levels as determined *via* FT-IR.

(A) The rate of water sorption to the substrate-polymer interface with various salts at 25 °C; (B) saturation levels of various exposure solutions at 25 °C.

These data were measured as an effort to explain differences observed in accelerated corrosion measurements from each chamber and relate the results to DI water exposure. As evidenced from the Arrhenius plots, there was a significant difference in the activation energies; however, these changes did not directly correlate to the results

obtained from the accelerated corrosion tests, which indicated that there are other factors that influence the observed rates. These factors include temperature, wet/dry time, and the cyclic nature of each corrosion measurement.

3.3.3 Corrosion measurements from ASTM B117

The averages from each triplicate for each tool type are plotted in Figure 3.12 as a total percentage of the panel exhibiting corrosion ($\bar{A}$) against time$^{1/2}$ (hrs$^{1/2}$). The slopes, or corrosion rates, from Figure 3.12 were then plotted against the scribe width to provide a corrosion rate versus scribe width and are shown in Figure 3.16. 350B scribing tools resulted in approximately 1.1-2.5x faster corrosion rate than observed with all other tools. These data indicated that the wider the path, the higher the corrosion rate and the greater percentage of the panel exhibiting corrosion. However, by measuring the change in total panel corrosion from the pre-exposed scribe area, using Equation 9, it became possible to correlate different scribe profiles simultaneously and accurately.

$$\Delta\, Area\ Percentage\ (\Delta\bar{A}) = \bar{A}_t - \bar{A}_0 \qquad \text{Equation 9}$$

Where $\bar{A}_t$ is the average total panel corrosion product at a given time and $\bar{A}_0$ is the average percentage of metal exposed in the initial as a function of the total panel. By comparing the change in total corrosion product with respect to the square root of time, as found in cathodic delamination literature, a linear correlation was observed.[124] Figure 3.17 indicates the average change in area percentage from triplicate measurements for each tool type and the non-scribed control samples. Trend lines were added to characterize the rate ($\bar{A}$/time$^{1/2}$) with good correlation coefficients ($R^2 \geq 0.9$). A representative image from each tool type at both t=0 hours and t=2000 hours is shown in

Figure 3.13. Only cathodic delamination was observed around the scribe region for all triplicate samples.

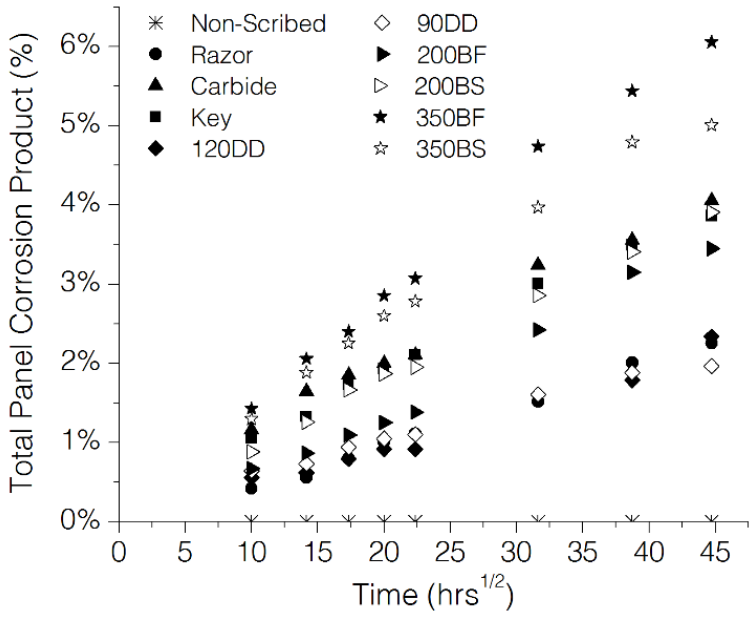

Figure 3.12 Total corrosion area for ASTM B117.

Total panel corrosion product (%) plotted against time$^{1/2}$ (hrs$^{1/2}$) of exposure in ASTM B117 up to 2,000 hours.

While Figure 3.13 depicts a representative image from each scribe tool, all of the panels in each triplicate resulted in statistically similar values. Immediately apparent was the vast difference in corrosion product surrounding the scribe for wider scribe profiles, which qualitatively confirmed that wider scribes result in greater visual corrosion product. Also visible was the collection of corrosion products toward the bottom end of the scribe. The significant amount of corrosion products at the end of the scribe was a direct result of iron oxide and added salt/water spray running down the panel during accelerated corrosion testing due to gravity, which caused a higher concentration of ionic species to accumulate at the bottom of the scribe, giving a larger corrosion product

domain. However, this was consistent among all of the samples, and the data still provided statistical relevance.

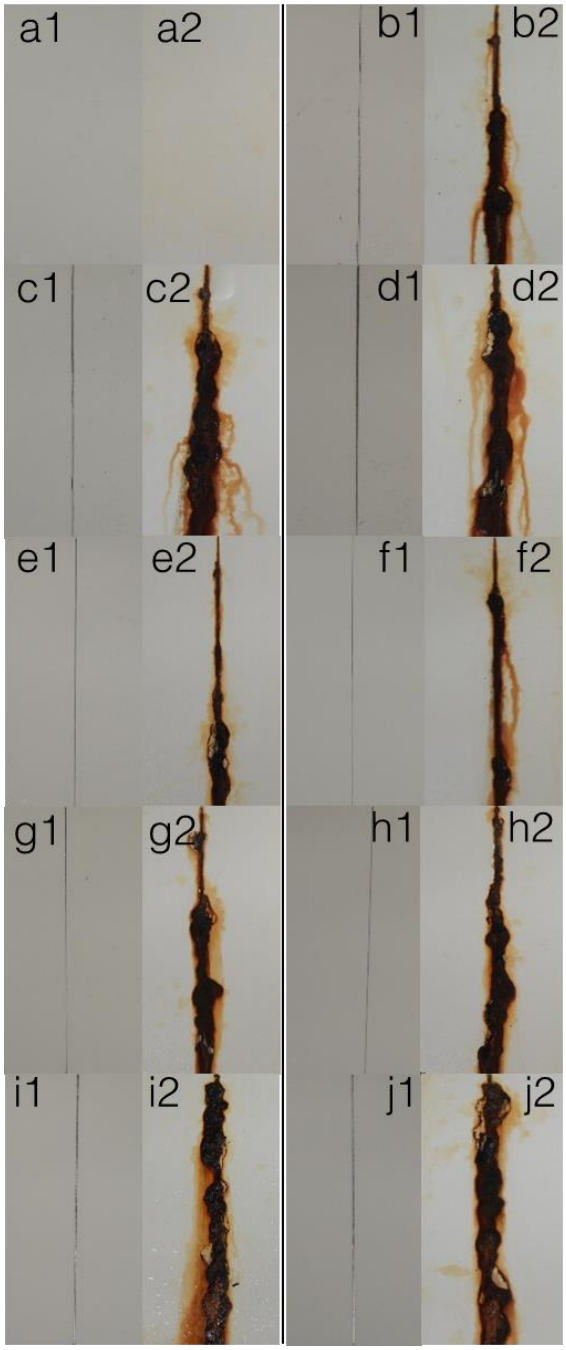

Figure 3.13 Representative images of pre-exposed and 2,000 hr ASTM B117 panels.

Pre-exposed (1) and 2,000 hour (2) exposed ASTM B117 samples: a) non-scribed; b) razor; c) carbide; d) key; e) 90DD; f) 120DD; g) 200BF; h) 200BS; i) 350BF; j) 350BS.

To determine the effect of chamber exposures, ASTM B117 was compared to GM 14872. The comparison delineated visual differences that may occur when exposing the same scribe patterns and coating type to a different accelerated test condition.

3.3.4 Corrosion measurements from GM 14872

As with ASTM B117, the average from triplicate for each tool type are plotted in Figure 3.14 as a total percentage of the panel exhibiting corrosion against time$^{1/2}$ (hrs$^{1/2}$). The rates for GM 14872, as calculated by Equation 9, are plotted against the scribe width in Figure 3.16. As performed with the ASTM B117 measurements, Equation 9 was used to calculate the change in corrosion area percentage from the initial scribe area percentage and plotted against the square root of time. Figure 3.14 indicates the average change in corrosion percent from triplicate measurements for each tool type and the non-scribed samples. As displayed in Figure 3.16, scribe width was less significant with regards to cyclical exposure (GM 14872). A representative image from each tool type at both t=0 hours and t=2000 hours (~83 cycles) is shown in Figure 3.15. While the images depicted were representative, all samples exhibited cathodic delamination around the scribed region. Within the GM14872 data, statistically, there is no difference between the scribing tools, as demonstrated in Figure 3.16.

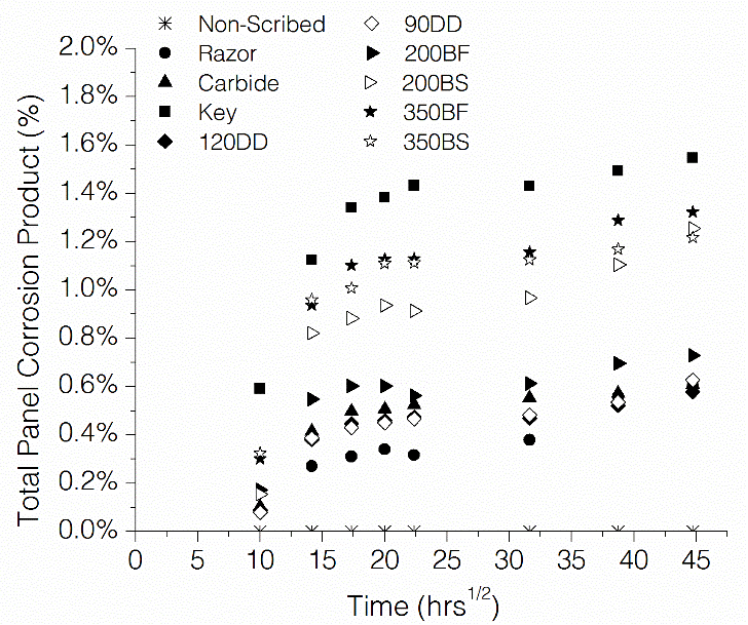

Figure 3.14 Total corrosion area for GM 14872.

Total panel corrosion product (%) plotted against time ($hrs^{1/2}$) of exposure in GM 14872 up to 2,000 hours (~83 cycles).

The images in Figure 3.15 visually exhibited less corrosion product than those exposed to ASTM B117. Comparison of the samples exposed to GM 14872 with those exposed to ASTM B117 qualitatively confirmed the difference in corrosion rates between the two chambers. While the Arrhenius plots indicated that the solution used for GM 14872 had the lower activation energy, the samples were exposed to much less salt spray over the samples' lifetimes in the accelerated chamber. Furthermore, the drying steps in GM 14872 reduced the amount of water accumulation at the metal substrate even further. Different from ASTM B117 was the formation of blistered regions around the scribe. The formation of these blisters indicated that the corrosion mechanisms between the two chambers were most likely different, and therefore should be used to measure different aspects of a coating's corrosion performance. Therefore, it is proposed that ASTM B117 and GM 14872 challenge distinctly different aspects of the coating's fundamental ability

to remain adhered and provide resistance to corrosion. Varying polymers need to be explored further to determine similarities and differences.

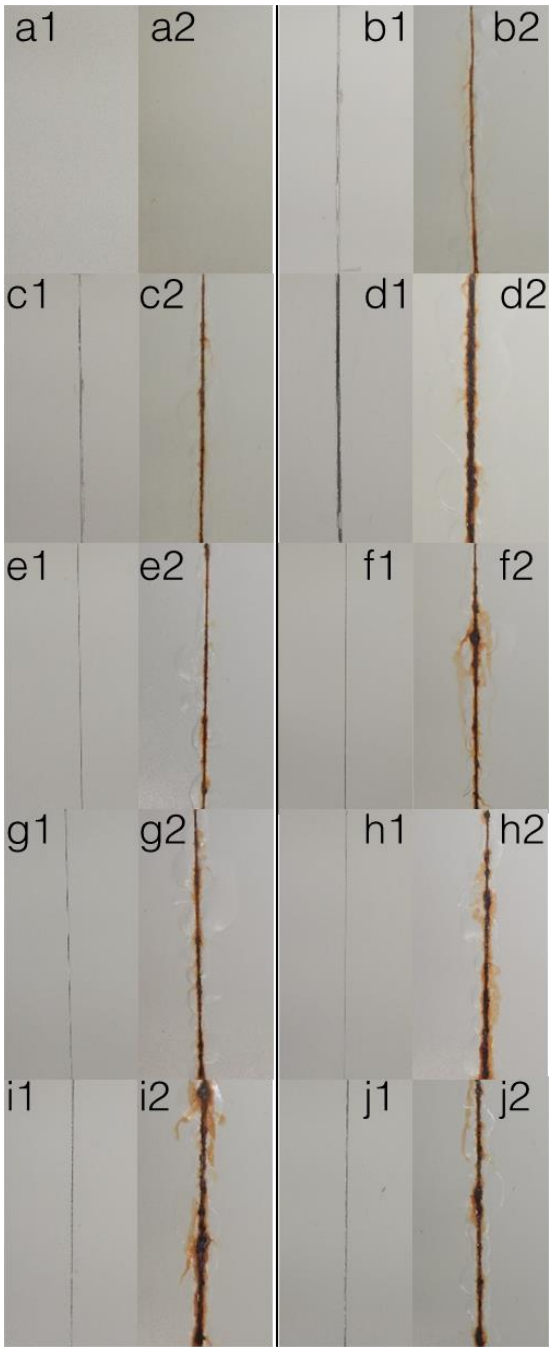

Figure 3.15 Representative images of pre-exposed and 2,000 hr GM 14872 panels.

Pre-exposed (1) and 2,000 hour (2) exposed ASTM B117 samples: a) non-scribed; b) razor; c) carbide; d) key; e) 90DD; f) 120DD; g) 200BF; h) 200BS; i) 350BF; j) 350BS.

The data in Figure 3.16 compares the corrosion rates as calculated from the slopes in 3.12 and 3.14 as a function of the scribe width, resulting in rates of % area/$hr^{1/2}$. As evidenced by these corrosion rates, ASTM B117-exposed samples exhibited a strong dependence on the scribe width, while GM 14872-exposed samples did not. The boxed region indicates two outliers in which the scribe width was narrow, but the samples exhibited a higher corrosion rate. The basis for these two data points will be discussed later utilizing SEM.

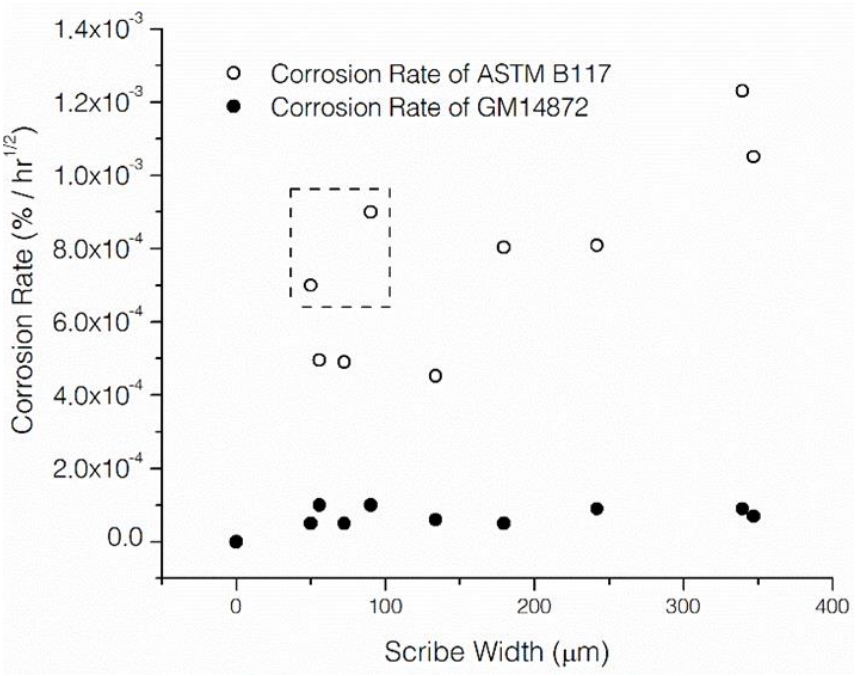

Figure 3.16 Comparison of corrosion rates (% area/$hr^{1/2}$) with scribe width (μm).

The corrosion rate of ASTM B117 (Open circles) and GM 14872 (closed circles) with respect to scribe width in μm.

This same effect was observed by Compère and co-workers.[171] While they measured different coating chemistries, they also changed the average scribe width, thus changing two variables simultaneously. Compère's data indicated that the coating with the widest scribe experienced a catastrophic failure and complete delamination; whereas the coating with the narrowest scribe, of different chemistry, exhibited no degradation.[171]

It is possible that their corrosion results were due to differences in coating chemistry; however, because the scribe width and thickness of the coating were different across coating chemistries, it is not possible to say with certainty that the results were limited to scribe dimensions or chemistry type. Regardless, the data are still consistent in that these results support our hypothesis that wider profiles resulted in greater corrosion area on a faster time scale than narrow profiles, due to the larger surface area for additional oxidation/reduction pathways and ingress of environmental contaminants.

Yasuda's claim that scribe width was inconsequential on corrosion rates can be explained from the basis of the underlying principle of electrochemical impedance spectroscopy (EIS), which was the only method utilized within that paper.[85] In EIS, any macroscopic breach will lead to immediate water and electrolyte penetration, as well as an excess of oxygen available for the corrosion reaction. Several researchers have found that the water, and subsequently, ion movement through a film is slower than movement laterally between the substrate and film.[172-173] From literature, the movement under the film comprised of identical chemistry and regardless of scribe width, would be similar due to the macroscopic nature of the artificial defect, meaning any changes in impedance would be similar. Contradictory to Yasuda's measurements, it was found that when visual assessments for corrosion analysis, rather than EIS measurements were used, wider scribe widths correlated with more corrosion product.

It is important to note that part of these data did correlate with Yasuda, as 200BF and S both exhibited large corrosion areas surrounding the scribe, even though the scribe width was relatively small. Much like Yasuda, metallic debris was observed away from the scribe prior to exposure, due to spalling of the substrate during the scribing process

with only the 200B scribe tool; thus this tool type was considered an outlier with higher corrosion rates from narrower scribes. These two data points are denoted in Figure 3.16 with a box. These metal fragments then became embedded into the surrounding polymeric coating and allowed for an increased metal surface area for corrosion to initiate and propagate. The SEM micrograph depicted a large debris field surrounding the scribe path and is shown in Figure 3.17. It is important to note, that the debris field extended down the length of the scribe, and was prevalent on the ends of the scribe.

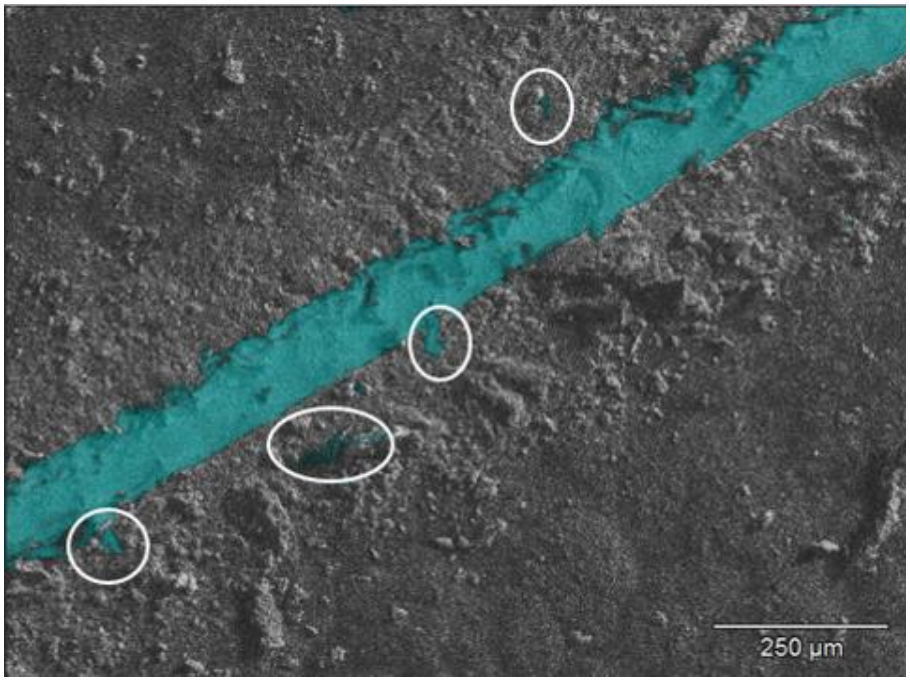

Figure 3.17 SEM micrograph of 200BF scribe profile debris locations.

Large amounts of metallic debris away from the scribe. Circled regions identify Fe detected away from the scribe. Scale bar is 250 µm.

To directly correlate the two exposure chambers and demonstrate a predictive approach, linear functions were generated using shorter time points and plotted against the real data. These predictive capabilities could shorten the amount of time necessary to evaluate coating systems and thus, decrease the time new technologies can be developed

for consumer use. Comparison of the chambers will also allow for inter-laboratory comparisons if the equipment is limited.

3.3.5 Comparison of accelerated corrosion chambers and predictive capabilities

While the tool types resulted in different corrosion rates when measured strictly as a function of the tool and exposure time, Equation 9 accounted for the initial corrosion area. Figure 3.18 plots each data point as an aggregated average of all nine tool types, while the error bars are one standard deviation from the mean. As indicated in Figure 3.18, a linear correlation between the tool types was observed when the initial area was taken into account. Therefore, by normalizing to the original exposed area, various tool types can still be used and are comparable. These results allow for a direct comparison of data, even if the tool type is different among measured panels.

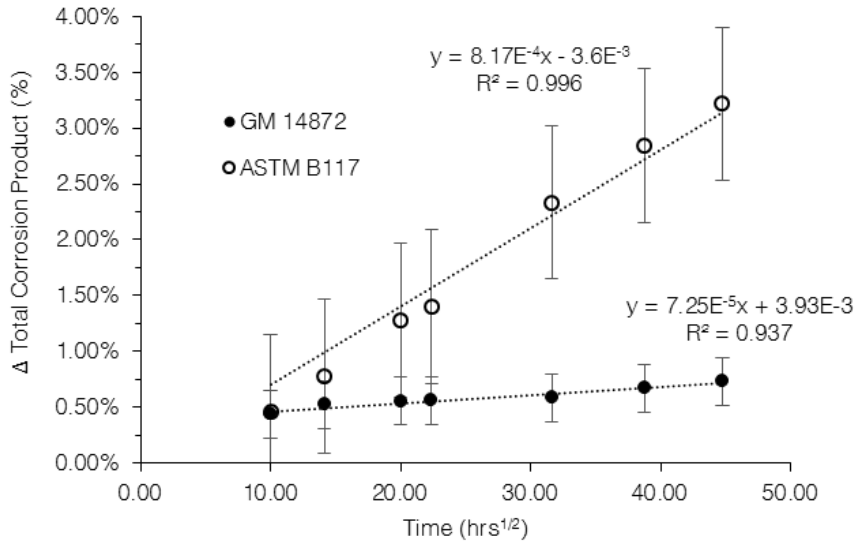

Figure 3.18 Change in total corrosion product for each accelerated corrosion test.

Change in corrosion product (%) for both ASTM B117 (open) and GM 14872 (closed) against time ($hrs^{1/2}$). Each data point contains the aggregate mean of all tools at a given time. Error bars are one standard deviation from the mean.

Both the ASTM B117 and GM14872 accelerated test chambers exhibited different rates of visual corrosion area as compared in Figures 3.18; however, it was found that comparing the two chambers against each other using lead to a nearly one-to-one correlation, even though the percent of corrosion product is statistically different (Figure 3.18). Each tool type's corrosion rate was averaged after normalizing to the original exposed area, and the corrosion products resulting from each chamber were plotted against each other. As indicated by Figure 3.19, there was a constant proportionality between the two methods when considering only cathodic delamination from the scribe. It was expected that other differences would be realized between the two techniques; however, further investigation would be needed to prove these differences, such as adhesion, corrosion product under the film, and color changes.

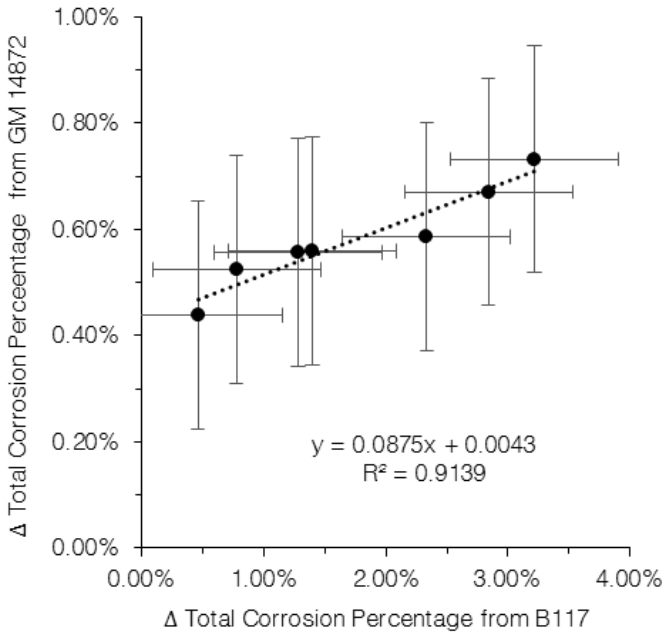

Figure 3.19 Compared change of corrosion between accelerated tests.

Each data point is an aggregate mean of all tool types at that time. Error bars are one standard deviation from the mean.

It is noteworthy that the slope of the $\bar{A}/t^{1/2}$ graphs (Figure 3.12) at 300 and 1,000 hours was accurate in predicting the corrosion product at 2,000 hours (Figure 3.20) for ASTM B117. The predications indicated that while the measurements were carried out to 2,000 hours, 300 hours in ASTM B117 would have been sufficient to predict the results at longer times. This knowledge could fast-track corrosion testing evaluations for future work.

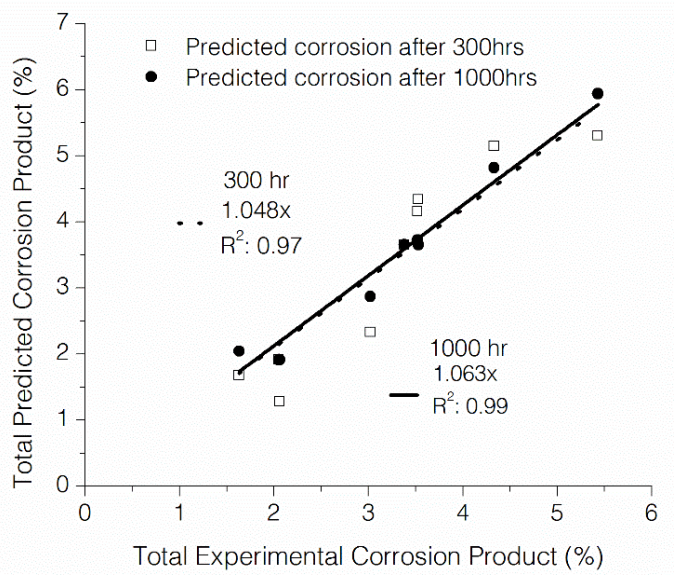

Figure 3.20 Prediction of corrosion product from ASTM B117.

Prediction versus experimental corrosion product at 300 hrs and 1000 hrs of accelerated corrosion testing.

3.4 Conclusions

This research validated scribe width was statistically significant while assessing corrosion performance visually on steel substrates during ASTM B117 exposure. Furthermore, the initial scribe area that was directly accessible to environmental contaminants was correlated to the observed corrosion performance. These experiments resulted in data that describe how scribe methods and profiles directly impact the observed induction period before a critical threshold was met before coating performance

characteristics were measurable. The initially exposed area was determined to directly impact the corrosion performance as the corrosion driven change in area (i.e., normalized to the original scribe area) remained constant at a given time point, regardless of the tool used. While literature very often fails to describe in detail tool types, material feed rates, rotational rates, and scribe width, this research definitively found a statistical correlation between the starting scribe widths and visual corrosion results.

Statistically significant values were found for samples exposed to ASTM B117; however, GM 14872 samples exhibited no statistical differences between tool types, which indicated that the time of wetness and salt composition/content were essential parameters which drive differences in corrosion driven material failure. The corresponding Arrhenius relationships for each method were not the only influencing parameters when the chambers were compared confirming that other mechanistic parameters were involved and need to be understood.

Cathodic delamination was predicted in early stages of ASTM B117 testing for time upwards of 2,000 hours of exposure, which indicated that longer times are not necessarily beneficial for evaluation of scribe delamination. These delamination rates were also linearly correlated between the two exposure chambers, meaning that both cabinets yielded the same data when only measuring delamination from a scribe as the corrosion result.

This research ascertains that salt content and composition, scribe width, wet/dry times, and exposure temperatures are all critical criteria that affect the overall induction period and final performance characteristics measured after the test cycles. Therefore, further investigation into the precise impact of these criterion are required.

CHAPTER IV – CONDITIONALLY SPECIFIC VOID FORMATION AND GROWTH FROM SOLVENT CAST THERMOPLASTIC POLYMER THIN FILMS

4.1 Objective

During some initial research, certain thermoplastic films were observed to have whitened during exposure to water. Upon further interrogation of the films, it appeared that the whitening was conditionally specific, i.e., certain drying conditions affected the whitening of the films. It was hypothesized that the type and content of residual solvents directly influenced the whitening of the films. By altering the content of water-miscible residual solvents, it was expected and verified that water sorption of poly(hydroxyether) thin films would result in differential performance characteristics that independently demonstrated differentials in induction periods. Furthermore, the molecular weight of the polymer was expected to relate to the degree of whitening that could be achieved through solvent efficiency, such that higher molecular weights would need more solvent to accommodate voids that caused whitening. The molecular weight of the polymer and corresponding relative differential in T_g with respect to ambient exposure conditions afforded another tunable variable to tailor the induction period for quantifying critical performance characteristic changes. The goal was to determine the causes and conditions specific to thermoplastic film whitening upon exposure to DI water. The whitening was shown to be rooted in a process whereby some solvent is trapped during film formation and vitrification, and then during immersion in DI water, the solvent rich domains exchange with water. This water-solvent exchange resulted in both swelling and a higher differential in refractive index between water and polymer such that the films appeared white visually. This chapter focused on understanding the relationship between the

drying conditions, residual solvent type and concentration, *in situ* T_g, modulus of the polymeric film, and immersion conditions required to induce whitening. The results are posited using one possible theory with tension measurements as possible predictors of void formation, and subsequently, whitening of the thermoplastic films herein. Internal stress, optical whitening, water diffusion, as well as corrosion analyses were all correlated to the development of ~ 2 μm diameter pores within a free-standing polymer film and when the same polymer films were substrate-bound. Albeit not visually observed, whitening was validated within commercial pigmented coatings, which is probable and likely the potentially weakest link for corrosion control coatings. These data collectively resulted in an understanding of how to combat undesirable void formation within polymer films. While most coatings are evaluated for corrosion performance with intentional defects, the voids formed *in-situ* during exposure could yield insight as to how coatings fail in the absence of defects. These results and understanding could be utilized to estimate the film characteristics' effect on inhibitor transport and how these variables alter inhibitor release profiles.

4.2 Results

4.2.1 Film and thermal properties

The film thickness of all samples was 20 ± 4 μm (excluding the internal stress measurements). After application and drying, the average residual solvent concentration and average film T_g values were measured (Figures 4.1A and 1B). Figure 4.1A represents the average residual solvent as an aggregate average of each molecular weight. These data indicated that the time and temperature of the drying conditions relative to the *in situ* T_g influenced the overall average residual solvent level. However, the low standard

deviations and statistical difference between each residual solvent level suggested that molecular weight did not influence the total amount of retained solvent. The nature of film formation and evaporation was attributed to the cause of low standard deviations as each film was dried and annealed relative to the virgin polymer T_g. Solvent near the coating-air interface can evaporate most easily considering other film locations, while solvent nearest the substrate-coating interface must diffuse through the polymer network, and is inherently occurring at a slower rate.[174] The evaporation was consequently more difficult and increased in difficulty as the air interface and the bulk material average T_g of the poly(hydroxyether) increased. The average T_g values for each polymer sample from varying residual solvent (as a result of different drying profiles) was re-graphed versus each polymer molecular weight, as well as the different drying conditions in Figure 4.1B. It was observed, that at each subsequent drying condition (either at extended times or elevated temperature), the amount of residual solvent was lower than less temperature/time, which was expected. These lower residual solvents resulted in successive higher bulk average film T_g values. Notably, even at low residual solvent (< 1.5 wt%), all systems continued to exhibit solvent softening/plasticization and the T_g values were consistently lower than the solvent-free, melt-processed T_g. These results confirmed that solvents, even when volatile, under the conditions of film formation become trapped and can persist for extended periods of time within the film.[175-176]

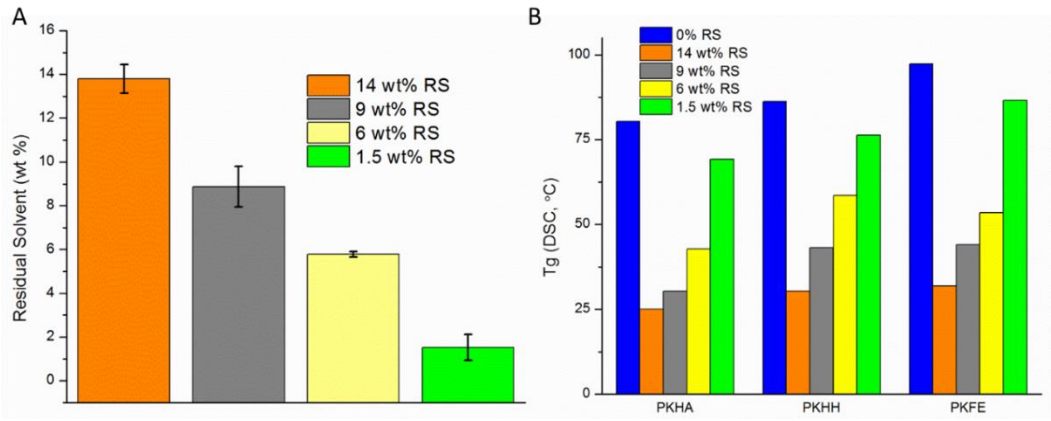

Figure 4.1 Residual solvent and glass transition temperature for each molecular weight thermoplastic and drying conditions.

Residual solvent weight% from each drying profile from all polymers annealed similarly (adjusted for each polymer's T_g) (A) and the absolute T_g values of each film at each drying profile (B). Error bars represent one standard deviation from the aggregated averages of duplicate measurements for each film.

Free-standing films were immersed individual experiments in each DI water or 5% NaCl for 24 hours to determine the wet T_g after exposure. As water plasticization initially occurred and further developed, hydrogen bonding interactions between polymer-water and water-solvent were expected. Poly(hydroxyether) is not water soluble, and therefore should interact with water through hydrogen bonding capabilities and yet have no defined solubility. However, the solvent blend used for applying these films (spray applied) as outlined in Chapter II were each highly water miscible. It was expected that the trapped residual solvent within the poly(hydroxyether) was extracted from the film as the water was absorbed, attributed to the more favorable water-solvent interactions. Each films' residual solvent extraction would result in a net increase in the T_g. Figure 4.2 compares the change in T_g from a non-exposed film as a function of initial residual solvent levels. Films that contained higher amounts of residual solvent exhibited the most substantial post solvent extraction increase in T_g, and not unexpected, the films

with the lowest residual solvent resulted in the lowest increase in T_g. The poly(hydroxyether) films that contained intermediate residual solvent levels (9 wt% RS and 6 wt% RS) exhibited statistically the same change in T_g after immersion.

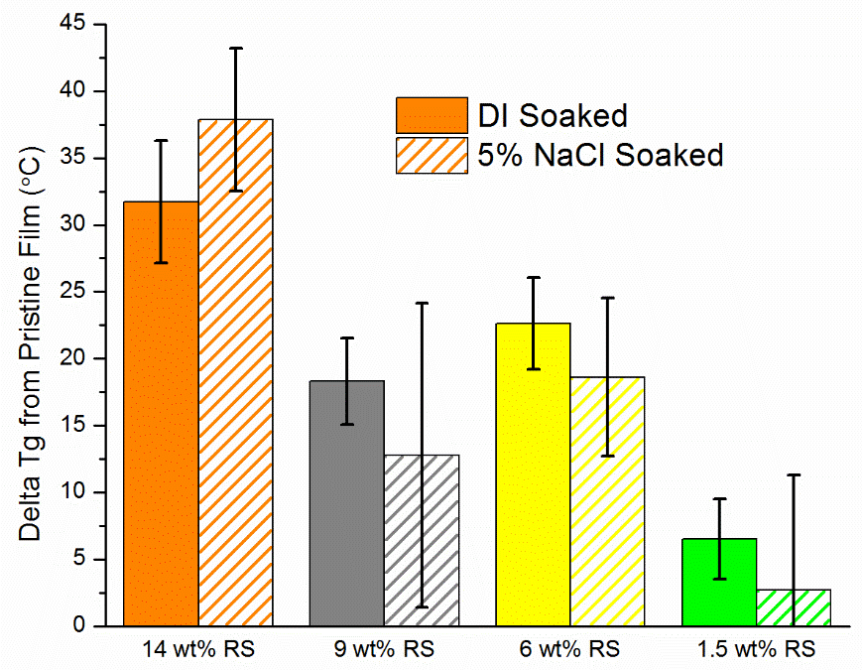

Figure 4.2 Delta T_g from a non-exposed film after DI water and 5% NaCl exposure by residual solvent level

Change in T_g for residual solvent level after exposure to DI water as measured by DSC. Solid bars are DI soaked while striped bars are 5% NaCl soaked.

In all cases, the films exhibited significantly large T_g increases, especially those that contained > 2 wt% residual solvent. While hydroplasticization is a known phenomenon, water is a less effective plasticizer (due to the non-solvent nature) than the solvent the resin was cast from (a good solvent for the polymer).[62, 177] In these films, the solvent was extracted which effectively increased the measured T_g. Extractability of films that were still solvent laden could occur easier as the modulus and T_g of the poly(hydroxyether) films were lower than the starting polymeric materials (in the absence of solvent). The lower modulus correlates with less required thermal energy for polymer

reptation and allowed water to more efficiently infiltrate the film and extract the residual solvent, which resulted in visibly whiter films. As evidenced by the error bars representing one standard deviation from the mean, the difference between the DI water and 5% NaCl soaked samples were not statistically significant at a 95% confidence interval (actual $\alpha = 0.06$). However, in almost all cases, the DI soaked films exhibited a greater T_g increase than those that were soaked in 5% NaCl. Upon addition of NaCl into the solution, there is a competing interaction between the salt/water and the water/polymer and water/salt and solvent. Salt has been shown in the literature to be effective towards inhibition of water interaction with the polymer, thus limiting the amount of solvent that could be extracted.[178] Therefore, the impact of salt concentration and temperature were measured and the data are reported in Figure 4.3. The color scale was indicative of the relative amount of water that reached the substrate after 16 hours of measurements where the red regions indicate the highest water content and the blue regions indicate the lowest.

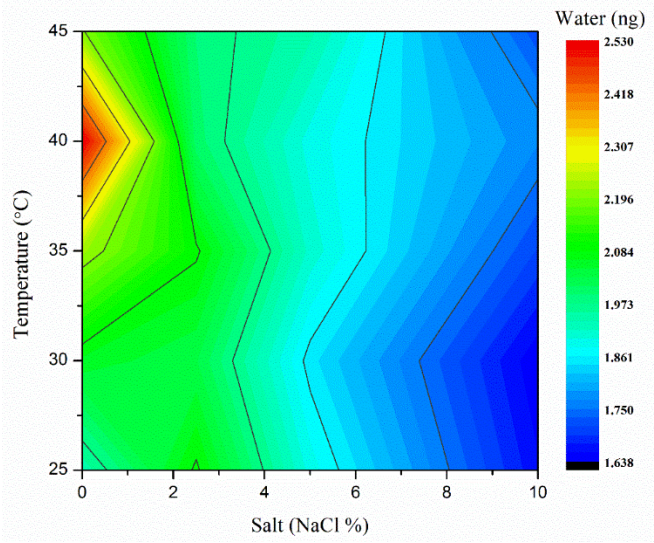

Figure 4.3 PKHH clear coating at 14 wt% residual solvent at different salt concentrations and temperatures.

At low salt content and high temperatures, water aggregated in higher concentrations than at high concentrations of salt or lower temperatures. As the salt content increased, the amount of water that reached the substrate was reduced, which was believed to be an effect of water-salt interaction limiting the interaction of water with the polymer, thus slowing the water sorption into the film to the substrate. Furthermore, even at increased temperature, the salt was effective at slowing the water sorption. Around 40 °C there existed a maximum of water that reached the substrate, whereby further increase of temperature afforded no additional water. This was attributed to the T_g of the polymer being centered in this temperature region. Decreasing the temperature resulted in a glassier film, whereas increasing the temperature would result in a more rubber-like film. Upon increasing the temperature further, there is no additional gains in water sorption.

The solvent swollen nature of these films was such that water could extract the solvent from the films, likely through non-solvent interactions with the polymer, i.e., solvent extraction was efficient and the remaining water was incapable of maintaining polymer in solution. This process resulted in phase separated domains developed from solvent rich and solvent poor domains within the polymeric film. The process, albeit difficult to confirm, is expected to occur in many polymeric materials cast from solvent. The residual solvent extraction process consistently resulted in voids within the film when the materials were adjusted to have a modulus value below a certain range discussed later in this chapter.

The Fox equation was utilized to give a theoretical T_g based on solvent content and water-solvent exchange within the film to understand the influence of water on T_g

changes.[179-180] The Fox equation, albeit simple, accounts for the T_g values of all of the parts by weight fraction to result in a blended T_g. In the case of the non-exposed films, the T_g was dictated by the solvent and the polymer present in the film, while the exposed film calculation assumed all of the solvents were extracted during immersion and water was present in the same concentration.

$$\frac{1}{Tg} = \sum_1^i \frac{w_i}{Tg_i} \qquad \text{Equation 10}$$

Where T_g is the weighted average glass transition temperature of the blend, w_i is the weight fraction of the individual components, and T_{gi} is the glass transition temperature of each component of the blend.

$$\frac{|Tg_{theo} - Tg_{exp}|}{\frac{Tg_{theo} + Tg_{exp}}{2}} \qquad \text{Equation 11}$$

Where T_{gtheo} is the theoretical glass transition temperature and T_{gexp} is the experimental glass transition temperature as measured by DSC.

The percent difference was determined using Equation 11 in which the absolute difference between the theoretical and experimental T_g values was divided by the average T_g. The results are shown in Table 4.1.

Table 4.1 Theoretical and experimentally determined T_g values (exposed indicates water immersion).

Polymer	Residual Solvent	Theoretical non-exposed T_g (°C)	Measured non-exposed T_g (°C)	Percent Difference (%)	Theoretical exposed T_g (°C)	Measured exposed T_g (°C)	Percent Difference (%)
PKHA	14	-1.5	25.1	226.2	15.8	53.3	108.6
	9	23.0	30.3	27.4	36.0	60.5	50.9
	6	40.0	42.8	6.8	49.5	60.6	20.1
	1.5	69.4	69.2	0.3	72.2	76.4	5.7
PKHH	14	1.4	30.4	182.9	19.1	58.2	101.3
	9	26.6	43.2	47.4	40.0	72.0	57.2
	6	44.2	58.6	28.0	54.0	62.1	14.0
	1.5	74.7	76.2	2.0	77.6	85.6	9.8
PKFE	14	6.8	31.9	129.5	25.2	54.0	72.6
	9	33.6	44.1	27.1	47.5	51.1	7.2
	6	52.2	53.5	2.4	62.5	74.8	17.9
	1.5	84.9	86.7	2.1	87.9	91.3	3.7

The theoretical T_g values were calculated using the Fox equation, while the measured T_g values were determined via DSC. Solvent and water T_g values were collected from literature.

In the case of the theoretical non-exposed, or solvent-laden, T_g calculation, the solvent was simplistically assumed to remain homogeneous within the film (i.e., the volume fraction of each component remained constant). At lower residual solvent levels, the percent difference between the theoretical and measured was low, which was thought to the result of the T_g being determined from mostly polymer. At high residual solvents, the percent difference was significant, which indicated that the Fox equation does not account for solvent interactions such as hydrogen bonding with the polymer. In the case of the exposed samples, the residual solvent was assumed to have been entirely replaced by water, i.e., only water and polymer contributed to the T_g. In this case, the overall trend remained the same as the non-exposed films; however, the percent difference between the theoretical and measured T_g at high residual solvent was lower (226% versus 108% difference). The change in percent difference again indicated that water behaved

as a non-solvent as there were reduced interactions with the poly(hydroxyether) film, creating two distinct regions. In the case of the non-exposed samples, the solvent remaining in the film interacted significantly with the polymer, creating a pseudo-single phase, whereby the Fox equation loses utility. Some assumptions were made to produce these data, such as the volume fraction of each solvent does not change during the drying of the film, and that water replaces all of the solvents present.

Further measurements with gas-chromatography mass spectrometry would prove out these subtle differences and are recommended for future studies. In every sample, the theoretical T_g as calculated with the Fox equation under-predicted the measured T_g, which again indicated that the equation does not account for polymer/solvent/water interactions. The samples exposed to 5% NaCl solution would also have been predicted to have the same T_g as the DI exposed samples. The Fox equation does not take into account the addition of salt, which was shown to cause a reduction in water/polymer interactions, both in this chapter and in Chapter III. However, the effective T_g of water is most likely altered by the addition of salt, which has not been reported in the literature.

4.2.2 Polymer Adhesion

Dry adhesion measurements were performed to determine the effect molecular weight and residual solvent had on adhesion to steel substrates, and the results are compared in Figure 4.4.

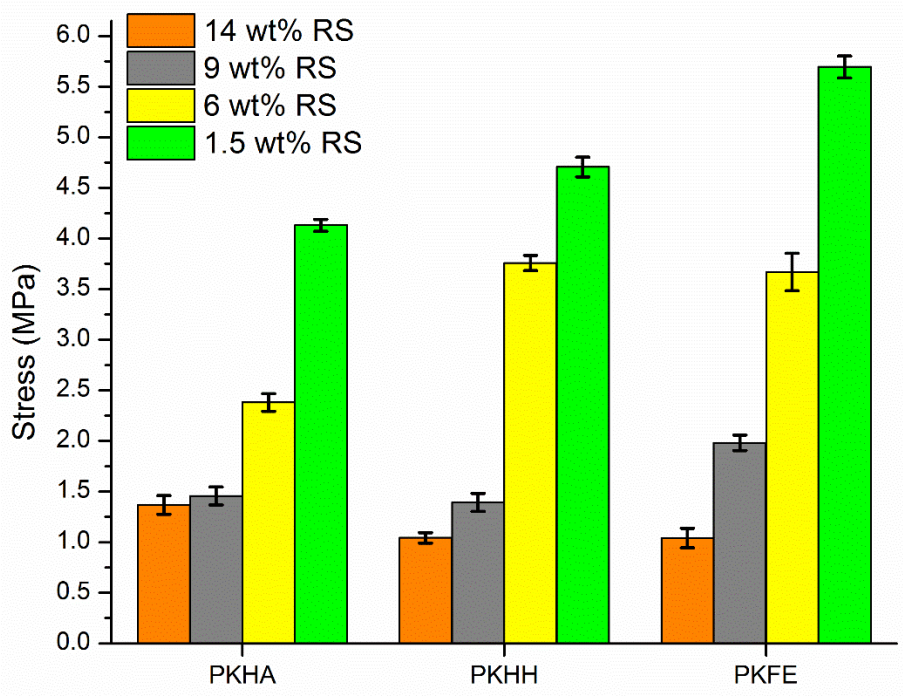

Figure 4.4 Pull-off adhesion measurements of each molecular weight and residual solvent level.

Each value represents an aggregated average of a minimum of 5 samples. Error bars are one standard deviation from mean for n=5.

From these data, it was readily apparent that adhesion increases with increasing molecular weight for this series of polymers (PKFE>PKHH>PKHA) when equal residual solvent levels were compared. At higher residual solvent levels (14 and 9 wt% residual solvent), each molecular weight exhibited similar pull off adhesion stress. This was thought to be a plasticization effect and increased solvent rich domains that lacked adhesion to the substrate caused by greater solvent concentration in the vitrified film. Upon reduction of the residual solvent to 6 wt%, adhesion increased dramatically. PKHH and PKFE films at 6 wt% residual solvent exhibited similar adhesion, while PKHA film adhesion was lower. It was believed that this difference between molecular weight contributions was a result of the molecular weight being lower which increased the polymer-solvent interactions within the good solvent. These polymer-solvent

interactions led to vitrification at later times and temperatures used for drying. These favorable interactions induced a more solvent-like character, although reduced from high residual solvent levels, than the equivalent films composed of PKHH and PKFE. This same trend was observed with a further decrease in residual solvent level to 1.5 wt%. At 1.5 wt% residual solvent, there existed a clear distinction between each of the molecular weights. The lack of residual solvent at the polymer-substrate interface for all molecular weights at 1.5 wt% likely resulted in minimized bond disruptions at the polymer-substrate interface, which lead to the adhesion increase. The same trends in molecular mobility of the polymer dictated by molecular weight were also observed during optical transparency measurements and internal stress values discussed later in this chapter.

4.2.3 Optical Transparency

Optical transparency was characterized by monitoring the absorbance of the poly(hydroxyether) films during DI water exposure for 24 hours. Measurements were collected between 300-800 nm in steps of 100 nm every 2.5 minutes and plotted using the averages of three distinct samples. The %transmittance was determined from the absorbance values by Equation 12.

$$\%T = 10^{2-abs} \qquad \text{Equation 12}$$

Where %T is the percent transmittance and abs is the absorbance value at a given wavelength.

Figures 4.5 - 4.7 report the decrease in the %transmittance of films during DI water exposure. All films regardless of thermal history exhibited less than 100% transmittance through the polymer film due to inherent absorbance and micro scratches that were imprinted on the films during preparation and removal from the substrate. The

size domains that form within the film dictate the wavelength of light absorbed. For example, 300 nm light is absorbed by smaller domains, while 800 nm light requires larger domains to be absorbed. Thus by probing a range of wavelengths, a qualitative assessment could be performed to understand the size scale of voids that formed and expanded within the film.

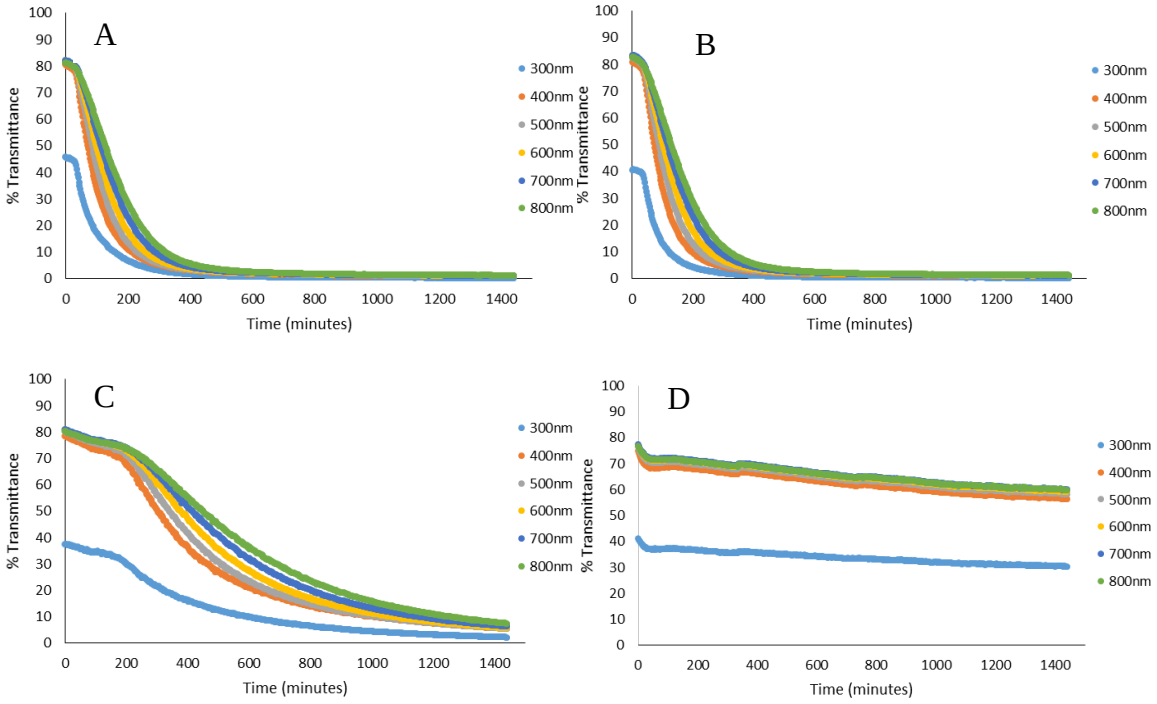

Figure 4.5 Optical transparency measurements PKHA at each drying condition.

% Transmittance as a function of time of exposure to DI water. All data points represent the average of three samples. A) 14 wt% RS; B) 9 wt% RS; C) 6 wt% RS; D) 1.5 wt% RS.

As evidenced by the data in Figure 4.5, the 14 wt% and 9 wt% residual solvent samples (A and B) exhibited very similar reductions in optical transparency with respect to time. The polystyrene sample holder induced an artificial decrease in the %transmittance for all data due to the absorption band of polystyrene being centered at 300 nm.[181] However, any changes to the spectra at 300 nm were due to the formation of microvoids during solvent extraction. All of the samples, regardless of residual solvent,

at 300 nm exhibited a small reduction up to about 45-50 minutes of immersion, likely due to saturation of the film with water. Samples A and B then exhibited a rapid drop in transmittance consistent with the formation of voids within the film. Each of the wavelengths in A and B followed the same trend (slight decrease, followed by a rapid loss of transmittance) until nearly 0% transmittance was achieved, which indicated a fully opaque film. The curves implied the high residual solvent lead to faster water uptake and solvent extraction as compared with other annealing conditions for the same polymer, which resulted in the greatest void growth within the polymer film. With decreasing solvent content (C and D) there was a slower reduction in transmittance (C), to almost no change in transmittance (D). While both the 14 wt% and 9 wt% residual solvent samples decrease to nearly 0% transmittance, the 6 wt% solvent only decreases to ~10 %T while the 1.5 wt% reached just 60% transmittance after 24 hours of exposure to DI water. Visibly, the 14 wt% - 6 wt% films appeared white, but the 1.5 wt% residual solvent films did not exhibit any whitening in the visual range (*ca* 500 nm).

Figure 4.6 reported the same measurements of PKHH films to afford a comparison of molecular weight derived modulus. While the overall trends remained the same as the PKHA samples, the time for whitening to occur increased with the increased molecular weight.

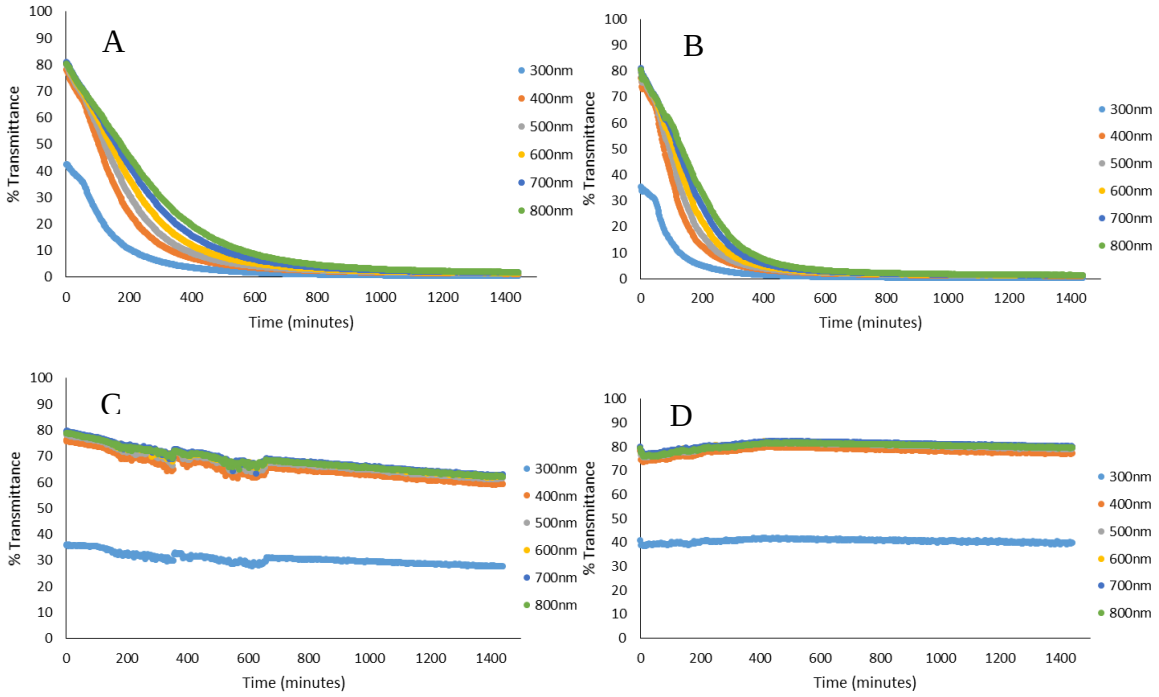

Figure 4.6 Optical transparency measurements of PKHH at each drying condition.

% Transmittance as a function of time of exposure to DI water. All data points represent the average of three samples. A) 14 wt% RS; B) 9 wt% RS; C) 6 wt% RS; D) 1.5 wt% RS.

As in the case with PKHA, the higher residual solvent films of PKHH (Figure 4.6 A and B) exhibited the same shallow reduction in transparency, followed by a sharp decrease. However, the time to reach 0% transmittance was extended to ~1,000 minutes, or nearly double that of PKHA films that contained the same amount of residual solvent. Deviating from the trends observed with PKHA, PKHH 6 wt% (Figure 4.6C) residual solvent films exhibited a prolonged whitening process, reaching just 60% transmittance after 24hrs of exposure. As with the adhesion measurements, it was likely that the higher molecular weight required more solvent to undergo molecular motions, such as swelling to accommodate the void growth within the film. Also notably different was the 1.5 wt% residual solvent PKHH film (Figure 4.6D). This film increased in transmittance for the first ~3 hours, which indicated the polymer was becoming more "clear." Polymer

relaxation within the film likely resulted in a reduction of air/water/polymer refractive indices difference. The % transmittance then remained constant for the duration of the measurement, which suggested no voids had formed within the bulk of the polymer and confirmed with cross-section SEM. Therefore, it was postulated that molecular weight limited the ability of voids to form within the film through a physical constraint, such as polymer modulus.

A continued trend of maintained %transmittance was observed for PKFE films, reported in Figure 4.7. These data exhibited the same overall trend that greater residual solvent resulted in a reduced %transmittance during exposure.

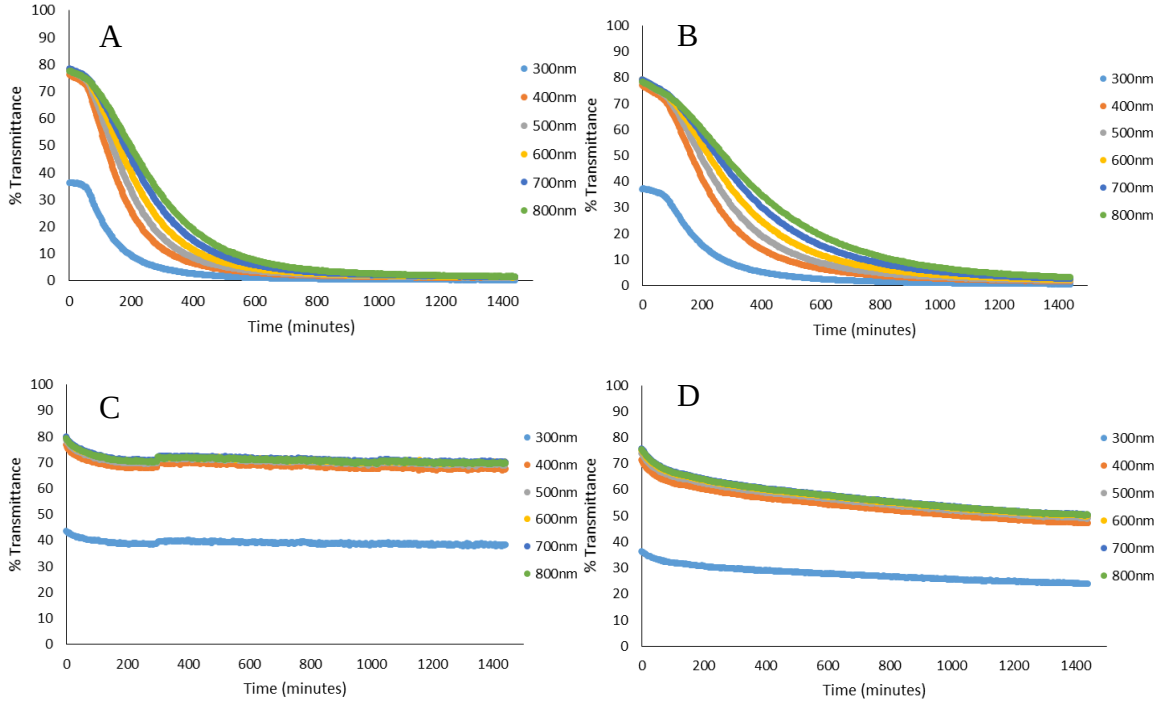

Figure 4.7 Optical transparency measurements for PKFE at each drying condition.

% Transmittance as a function of time of exposure to DI water. All data points represent the average of three samples. A) 14 wt% RS; B) 9 wt% RS; C) 6 wt% RS; D) 1.5 wt% RS

PKFE films exhibited very similar trends as PKHH, but the length of time to reach 0% transmittance was extended. The films reached 0% transmittance at all

wavelengths immediately prior to ending the measurements for the films that contained 14 and 9 wt% residual solvent. The 6 wt% residual solvent PKFE film (Figure 4.7C) exhibited a slight decrease followed by a plateau after which no additional whitening occurred. The reduction in % transmittance for Figure 4.7C was most likely caused by an instrument or measurement error as there was no visual whitening, nor were there voids during cross-sectional SEM studies.

When directly comparing the same residual solvent levels across the three poly(hydroxyether) molecular weights (PKHA, PKHH, and PKFE), an explicit dependency on molecular weight (directly impacting T_g and modulus) was established. These optical transparency data, along with the corresponding SEM cross-sections discussed later in this chapter, suggested that void formation and growth could be tailored based on the modulus of the film through molecular weight changes, residual solvent, and time of immersion in DI water. Most probably was that the higher molecular weight films consisted of longer polymer chains which required more energy to displace with voids.[182-183] The data suggested that greater osmotic pressure or more energy was needed to form voids in a lower residual solvent film or higher molecular weight polymer film.

These data also directly correlated with the void concentration and void sizes within the bulk of the film as determined from SEM discussed later in this chapter. Thus, even slight residual solvent content decreased the polymer modulus, film T_g, hardness, and increased polymer mobility for void formation. The polymer modulus will be discussed in more detail in this chapter using RH-DMA to refine further the differences observed during transmittance experiments.

These data support Fedors' and Sundberg *et al.*'s relation of plasticized modulus and void formation. A localized reduction in the film modulus likely caused by higher residual solvent content accommodating water and water cluster formation directly related to the measured degree of whitening.

4.2.4 SEM Morphology

In order to visually confirm what was measured using UV-Vis, electron micrographs were collected. In each case, free films were immersed for 24 hours in DI water, removed, patted dry, and cryo-fractured in liquid nitrogen to preserve the morphology induced by exposure. Also, a set of samples were immersed for defined periods such that a fractured surface was created every hour to monitor the progression of voids with respect to time and to afford a visual analysis of where and when the voids appeared. In all the subsequent images, the air interface of the film is at the top of the image, while the interface that was in contact with the polypropylene sheet is at the bottom. Figure 4.8 compares representative 0 hour and 24-hour films of PKHH and PKFE films containing 14wt% residual solvent.

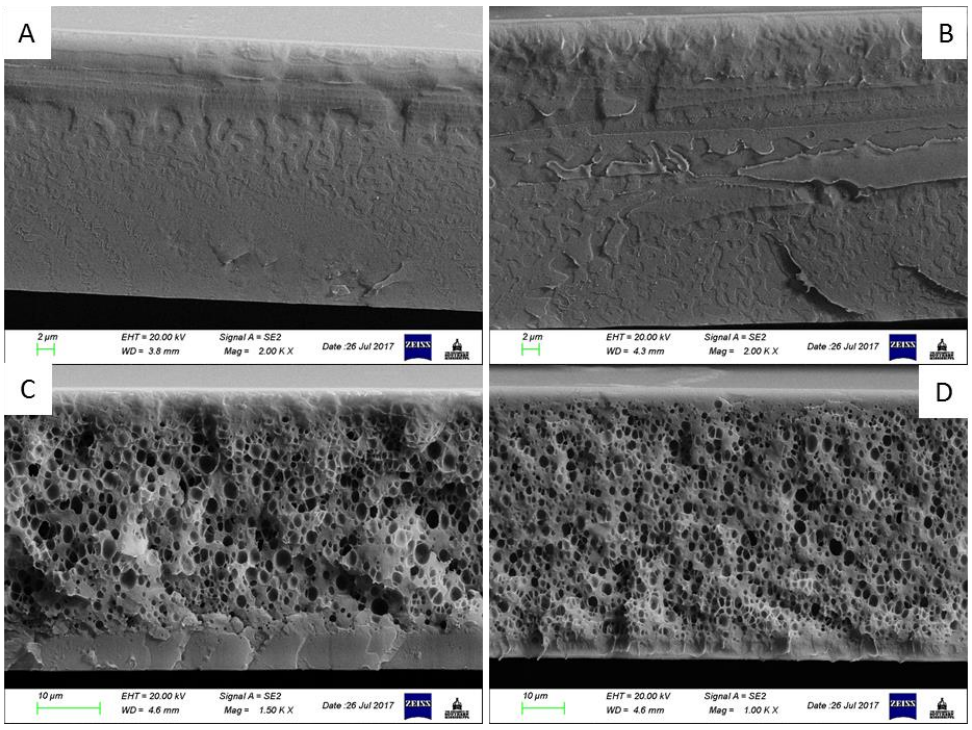

Figure 4.8 SEM micrographs of PKHH and PKFE films containing 14 wt% residual solvent before and after exposure to DI water.

Pre-exposed films (top; A and B) and 24 hour DI water exposed (bottom, C and D) films. PKHH (Left, A and C) and PKFE (Right, B and D) films containing ~14 wt% RS. The film-air interface during drying is oriented up for consistency in all SEM micrographs.

Each of the films that contained 14 wt% residual solvent that were exposed to DI water exhibited cellular-like structure after 24 hours of immersion. These micrographs afford a visual bulk polymer morphology to relate to the optical transparency data discussed previously. There were two distinct regions after exposure: the surfaces (both air and substrate) and the polymer bulk in which the voids formed. There existed little or no voids at the interfaces of the film, which suggested there is a tension force that restricted the formation of the voids at these interfaces. Furthermore, it was expected the center of the film would be comprised of the most and largest voids as it should have the most residual solvent after drying and the solvent would have the most difficult time escaping the center of the film due to longer diffusion paths.

As a comparison, Figure 4.9 shows SEM micrographs of the same PKHH and PKFE films at 0 and 24 hours of exposure; however, these films only contained 1.5 wt% residual solvent. These micrographs revealed the absence of any detectable voids after DI water exposure at ambient temperature, unlike those observed in Figure 4.8. In the case of 1.5 wt% residual solvent samples, it was likely the remaining solvent content was below a threshold necessary for water alone to drive detectable void formation. The lack of void formation and corresponding whitneing suggested a lack of polymer chain mobility, mirrored in the internal stress data discussed later. Upon the removal of solvent from the film, the polymer chains become more locked in their conformation and require more energy than water can provide at 20 °C (ambient laboratory temperature).

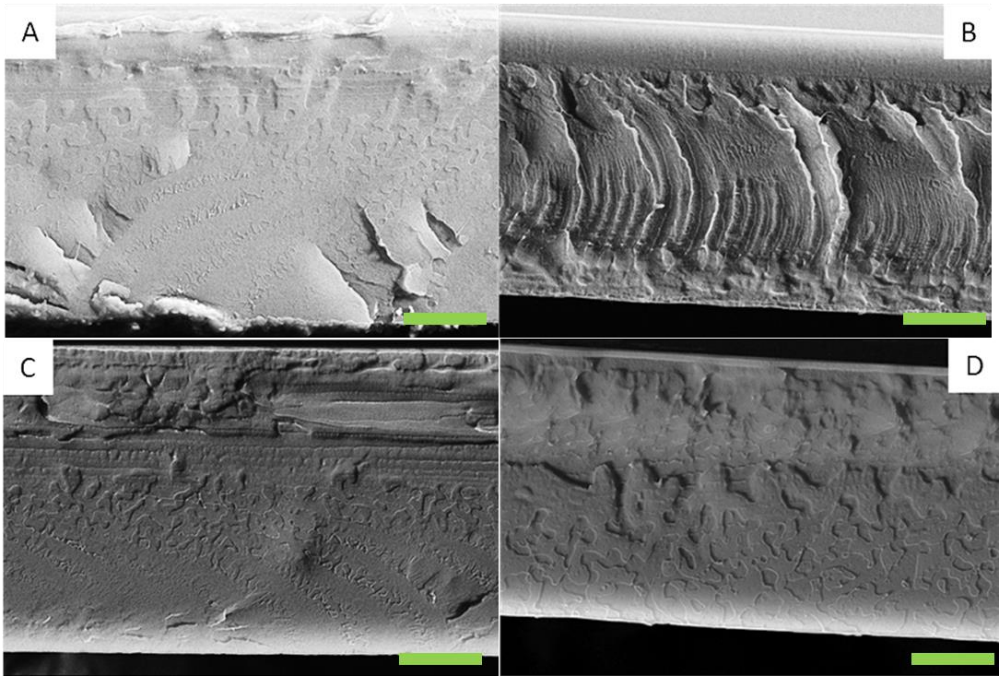

Figure 4.9 SEM micrographs of PKHH and PKFE containing 1.5 wt% RS pre and post DI water exposure.

Pre-exposed films (top; A and B) and 24 hour DI water exposed (bottom, C and D) films. PKHH (Left, A and C) and PKFE (Right, B and D) films containing ~1.5 wt% RS. The film-air interface during drying is oriented up for consistency in all SEM micrographs. Scale bar is 10 μm.

Figure 4.10 reports the evolution of voids of a PKHA film that contained 14 wt% residual solvent at various times of DI water immersion. The non-exposed film depicted a clean fracture plane, free from voids or any apparent defects in the bulk of the film. After one hour, small pinholes formed in the central region of the film. These pinholes grew into voids and increased in number with each subsequent time point. The voids formed in the center of the film first, subsequently expanded and increased density outwardly from the center. In contrast to the PKHH and PKFE samples depicted previously, the PKHA film did exhibit voids at the interfaces of the film; however, these only formed near the end of the measurement time and were composed of smaller voids than those in the bulk of the film. It is also important to note that each time point was a different sample, as once the sample was cryo-fractured and sputter-coated, the sample was considered used and could be re-immersed for further measurements.

In the case of the high residual solvent films, the micrographs exhibited that as the length of DI water exposure continued, more and larger voids were formed, which suggested that the polymer/solvent and water combined modulus was sufficiently low to allow the osmotic pressure to continue to rise within the bulk film during water driven solvent extraction. Furthermore, PKHA polymer films with 14 wt% residual solvent swelled to twice the original thickness after 24 hours of immersion in DI water. In contrast, PKFE films of equal residual solvent levels swelled to 1.5 times the original thickness during the same exposure duration. The difference in swelling implied that the molecular weight also directly influenced the void formation process.

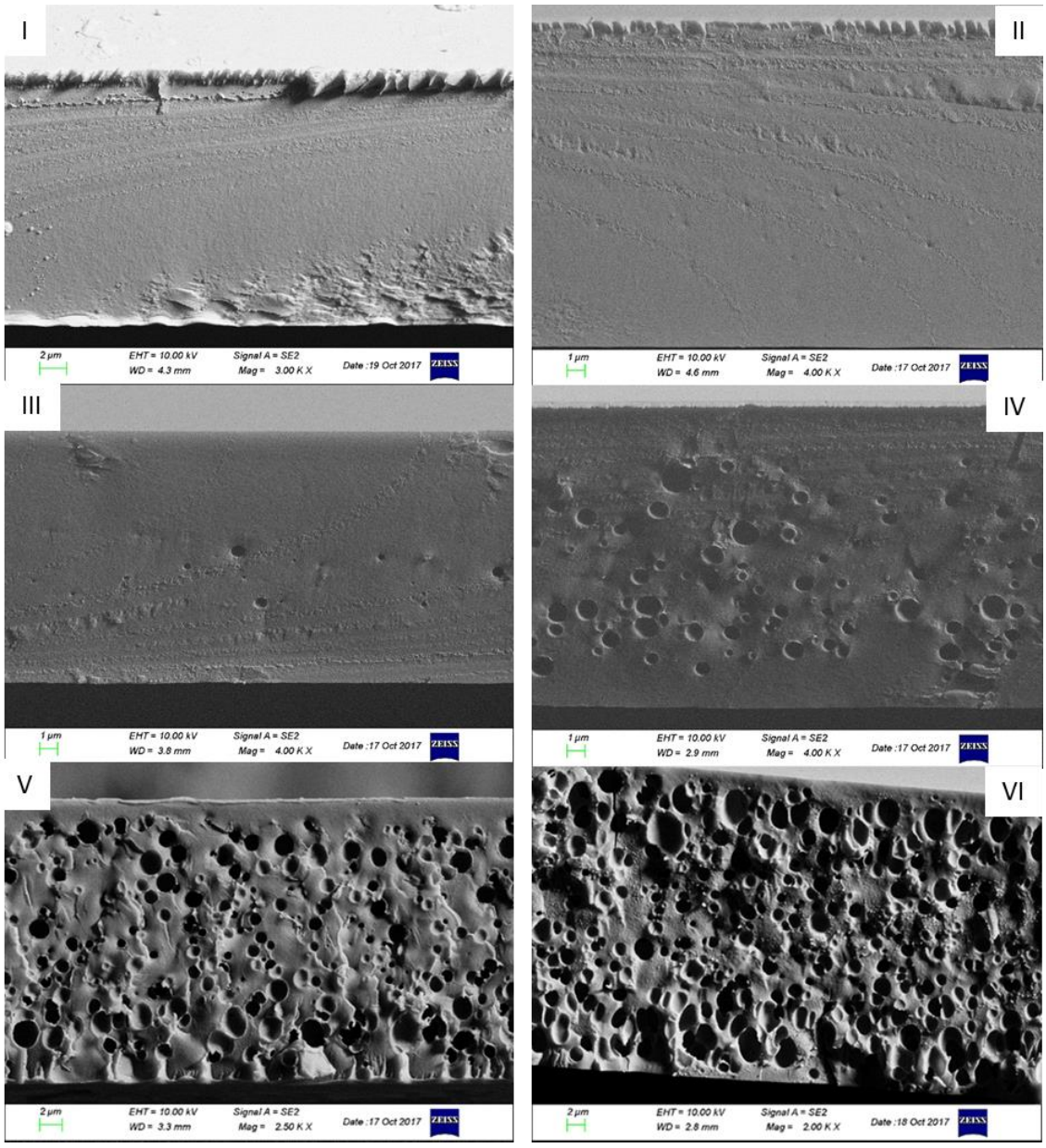

Figure 4.10 SEM micrographs of PKHA containing 14 wt% RS at various time intervals of DI water immersion.

Pre-exposure (I), 1 hour (II), 2 hours (III), 4 hours (IV), 14 hours (V), and 24 hours (VI) after DI water exposure at RT. The film-air interface during annealing is oriented up for consistency in all SEM micrographs. Scale bars are 2 µm.

To compare the results of the free films, cross-sectional SEM was performed of DI water exposed substrate bound films after 24 hours of exposure. Poly(hydroxyether) films were spray applied to a stainless steel substrate, exposed to DI water at the air-

polymer interface, and subsequently removed and cross-sectioned. Figure 4.11 compares the SEM micrographs of PKHA at three different solvent levels after substrate-bound exposure.

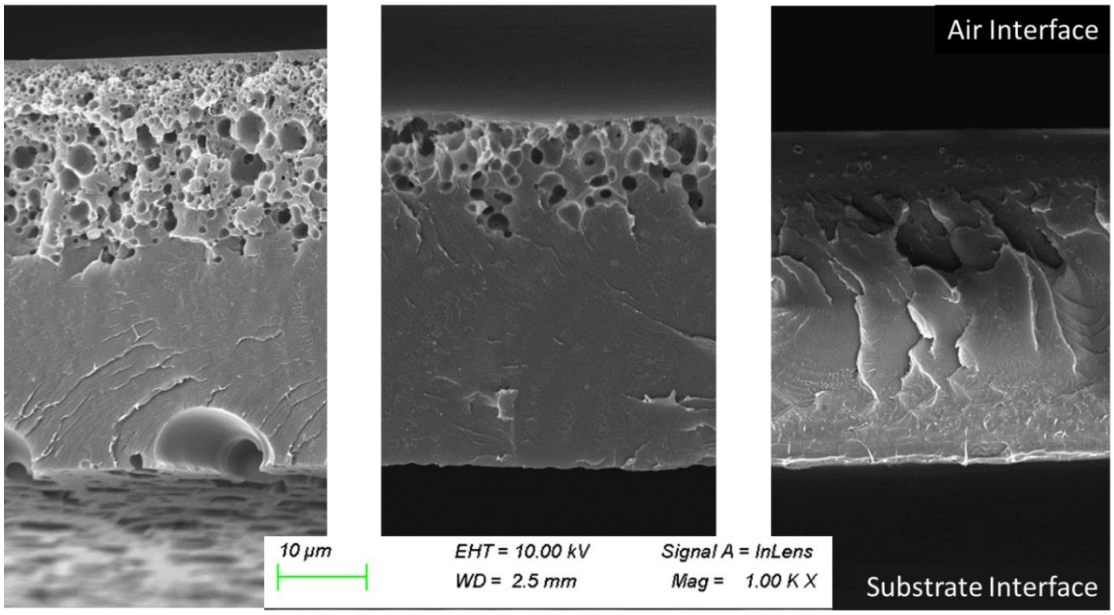

Figure 4.11 SEM micrographs of substrate-bound PKHA from most to least residual solvent.

Films that contained 14 wt%, 9 wt %, and 6 wt% RS (L-R) after exposure to DI water while bound to a stainless steel substrate.

The void formation was observed for substrate bound films, as indicated in Figure 4.11. The PKHA film that contained 14 wt% residual solvent (left, Figure 4.11) was observed to have voids at both the air and substrate-polymer interface. The voids at the air interface, which was directly in contact with the DI water during the exposure, exhibited smaller, but a higher density of voids, indicative of rapid water uptake into the film. The rapid formation and higher density of these voids inhibited the growth, so only small voids were present. The substrate-polymer interface was found to have a lower density of voids, but of much larger size scales. These voids would be formed by water reaching and accumulating at the substrate at a slower rate than at the exposure interface.

Also observed in the out of plane SEM micrographs were more voids, which indicated that water not only reached the substrate but migrated at the substrate-polymer interface under the film and formed more voids.

The PKHA film that contained 9 wt% residual solvent (middle, Figure 4.11) only had void formation and growth at the polymer-air interface or the area that was in direct contact with the DI water during exposure. Although the film appeared white visually, the voids did not form within the bulk of the polymer film. Given sufficient time, it was expected that there would be voids; however, the adhesion to the substrate may have slowed the formation, as the water could not overcome the modulus of the adhered film to create voids. PKHA films that contained just 6 wt% residual solvent (right, Figure 4.11) did not have any detectable voids at either interface, which again suggested that the plasticized threshold of the polymer film was more significant than the water pressure within the film.

4.2.5 Water Diffusion

Water transport from the air-polymer interface, through the bulk film, and to the substrate-polymer interface was hypothesized by Adamson for films exposed at temperatures below T_g. In his postulation, water is transported in three stages: 1) free volume is occupied first and quickly; 2) water binds to the polar moieties on the polymer chain through hydrogen bonding, causing swelling; and 3) water slowly percolates into the densely pack and/or crosslinked regions of the film.[184] While Gupta *et al.* postulated diffusion models based on T_g and exposure conditions, what should be considered is the difference between the T_g and the exposure temperature.[185] This ΔT_g is more representative of the diffusion kinetics, i.e., Langmuir models are used for exposure

temperature below T_g and Henry's law for above T_g.[185] Due to the significant difference in T_g, highly solvent laden systems should be less impacted by free volume considerations than those that contain less solvent.

Water sorption kinetics for the three different residual solvent samples are described in Figures 4.12A-C. At 14 wt% residual solvent (Figure 4.12C) PKFE films exhibited faster water sorption kinetics and an increase in water present on a time basis, normalized to the film thickness (PKFE>PKHH>PKHA). Most probable, heterogeneity on a localized scale (water, residual solvent, and polymer) in the high residual solvent films resulted in both faster diffusion and higher water content within the time frame of measurement.[185]

Figure 4.12B reports the water sorption kinetics for PKHH films at 14, 9, and 6 wt% residual solvent. These results trended with expected chain end contribution to hole free volume. As molecular weight decreased and the chains lost mobility from a lack of solvency, the greater number of chain ends present in the low molecular weight polymer films resulted in an increase in hole free volume, which contributed to a faster and higher degree of water permeation.[186] When comparing Figure 4.12 on a residual solvent concentration basis, films that contained a higher amount of solvent after annealing exhibited greater water content at the substrate at earlier times, as the water could more easily penetrate the film through the water-solvent exchange. When the solvent concentration was reduced, the water was forced to permeate through interstitial voids or along polar groups of the polymer backbone, thus slowing the rate of water sorption.

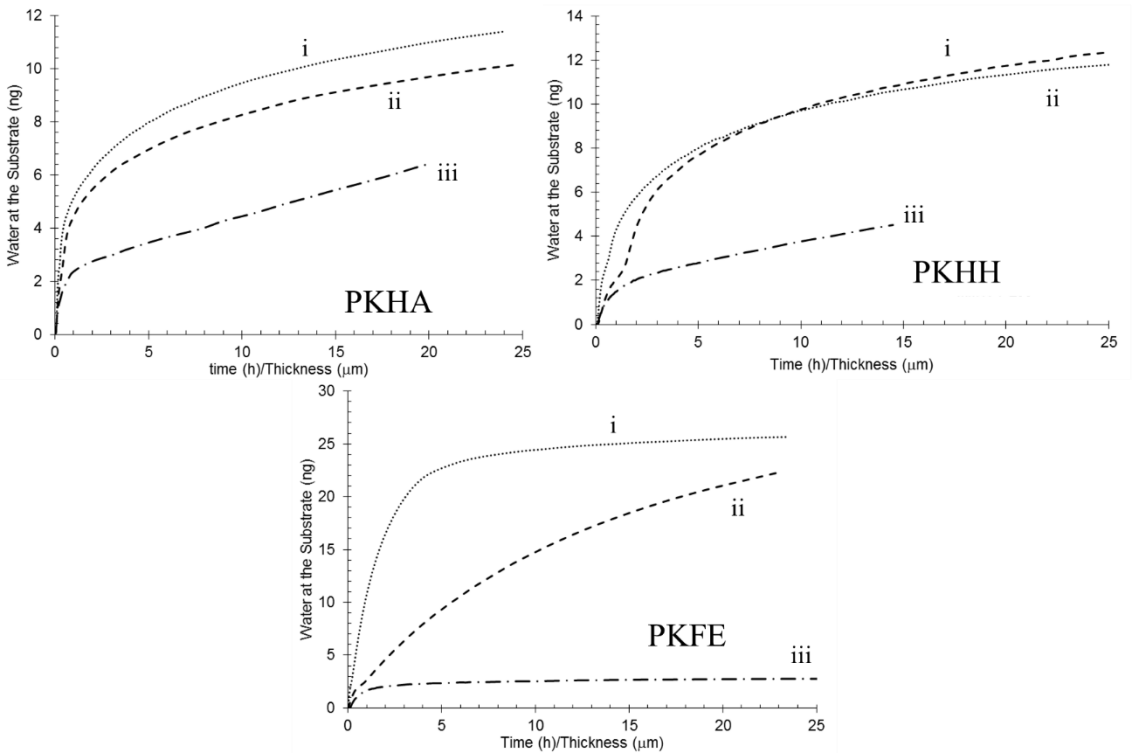

Figure 4.12 ATR-FTIR water diffusion results for PKHA, PKHH, and PKFE, and the resultant diffusion coefficients.

DI water saturation time-based sorption kinetics for drying condition and polymer molecular weight via ATR-FTIR at 25 °C. PKHA (A), PKHH (B), and PKFE (C) are represented on a time basis and normalized to film thickness. Residual solvents are i) 14 wt%, ii) 9 wt%, iii) 6 wt%. The diffusion rates are listed next to Figure 10C.

Both PKFE 14 wt% and 6 wt% residual solvent films reached saturation within the time frame of measurements, indicated by the plateau in the spectra in Figure 4.12C. PKHA and PKHH samples continued to increase in water content at the substrate such that a saturation limit was not reached in the time span of these measurements. This correlated well with the swelling observed in the SEM micrographs. Swelling of the polymer films allowed for greater water to accumulate in the film and consequently, the film could not reach saturation within the exposure time. The diffusion coefficients, compared in Figure 4.13 indicated that for all polymer molecular weights samples that

contained 14 wt% residual had the fastest diffusion and that higher molecular weight polymers exhibited slower diffusion (PKHA>PKHH>PKFE).

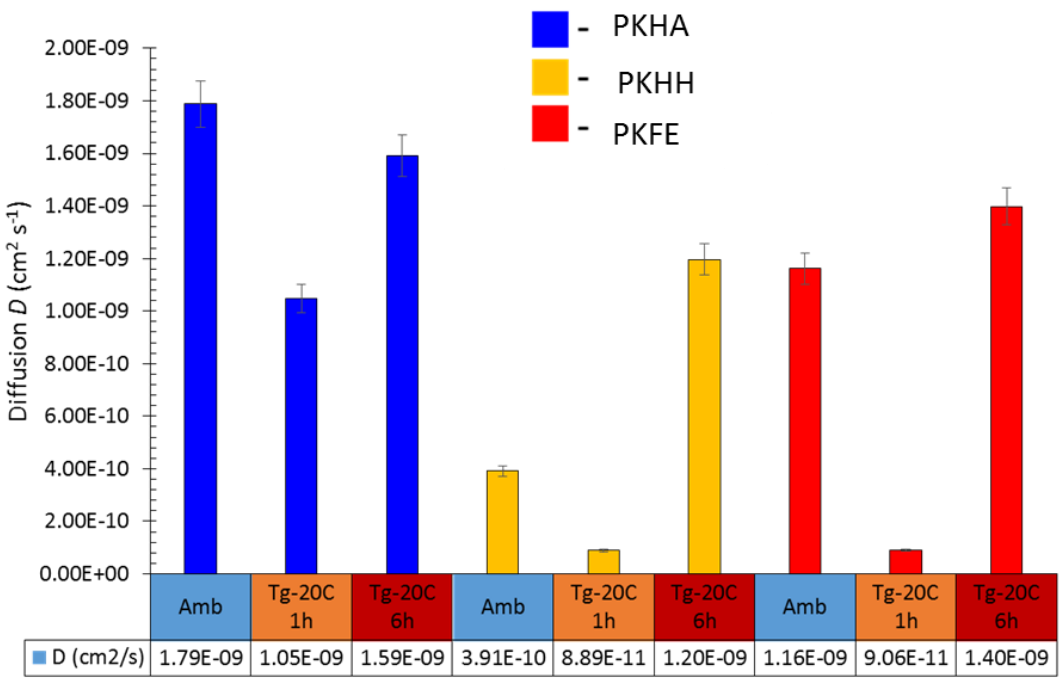

Figure 4.13 Diffusion coefficient for each molecular weight and drying condition.

Thickness normalized diffusion coefficients as determined via ATR-FTIR spectroscopy.

The diffusion coefficients for each molecular weight and drying condition was derived from the linear region of the sorption curves using Equation 6. Molecular weight, along with the residual solvent, altered the diffusion rates of the poly(hydroxyether) films. Immediately apparent was the low diffusion coefficient of films that contained 9 wt% residual solvent in comparison with films that contained 14 wt% and 6 wt%. While unexpected, this most likely represented a critical solvent threshold that allowed for better chain relaxation as the films were still plasticized sufficiently to afford chain mobility.

Molecular weight increase also decreased the diffusion coefficient when compared to films that contained similar amounts of residual solvent. During exposure to DI water, the water could interact with the hydroxyl pendent groups of the poly(hydroxyether) chain, slowing the water diffusion to the substrate. These longer chains, or higher molecular weight polymers, effectively behaved to increase the tortuosity of the water through the film through interaction with the polymer.

4.2.6 Internal Stress

Internal stress studies were performed to monitor the evolution of both expansive and compressive stress as the films were cycled between wet and dry conditions. The internal stress of each drying condition are reported in Figure 4.14-4.17. These measurements were performed utilizing the single cantilever method outlined in Chapter II. Residual solvent levels and molecular weight differences between poly(hydroxyether) films were interrogated through five wet-dry cycles to determine if internal stress would increase throughout multiple exposures. The data in Figure 4.14 compares the internal stress profiles of PKHA, PKHH, and PKFE at 14 wt% residual solvent.

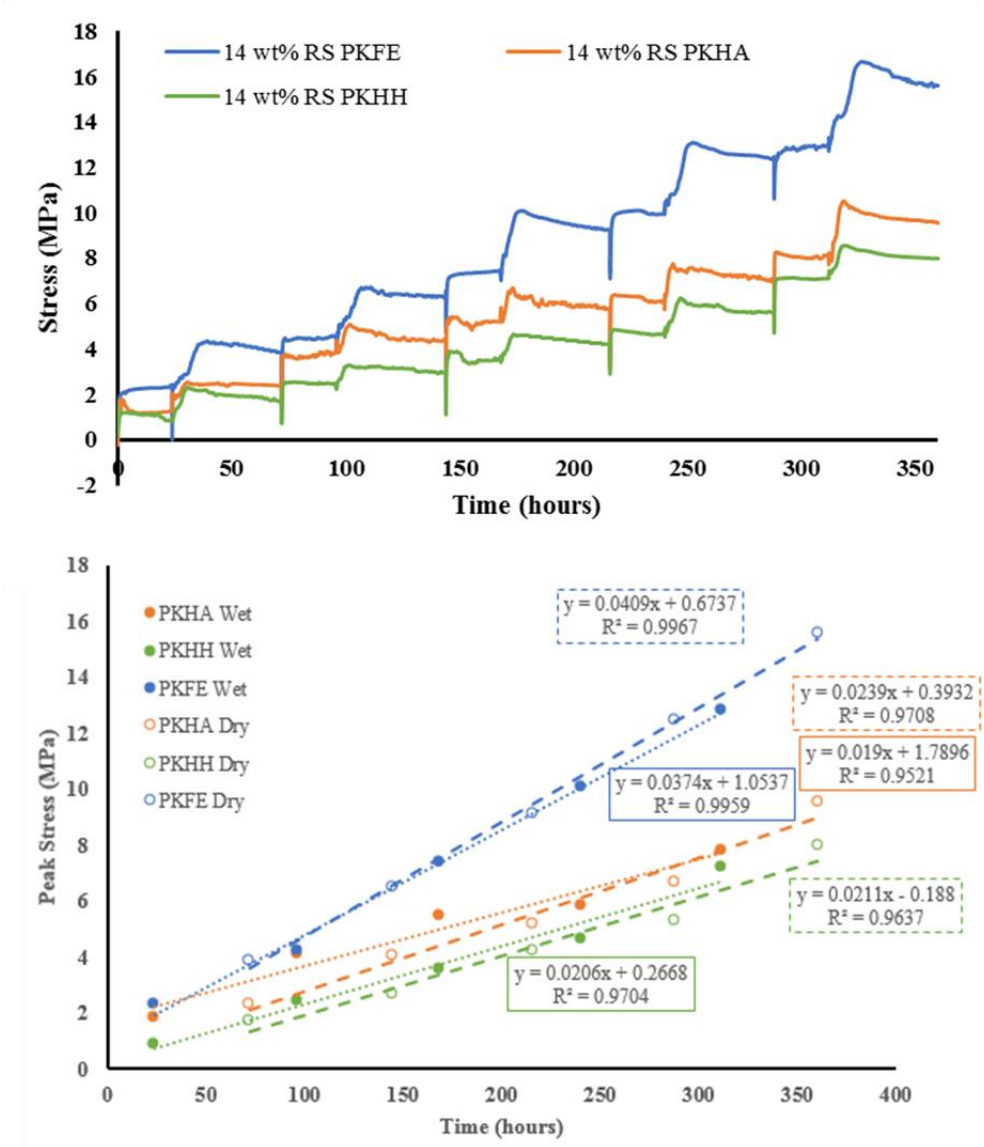

Figure 4.14 Internal stress profiles for PKHA, PKHH, and PKFE containing 14 wt% RS during cyclical DI water and dry exposure.

(Top) Internal stress of ambient dried films of each polymer molecular weight during wet (24 hours) and dry (48 hours) cycling.

(Bottom) Peak stress before changing from wet-to-dry measurements.

As shown in Figure 4.14, the films that contained 14 wt% residual solvent all exhibited initial or residual stress of ~ 0 MPa. The internal stress increased with each subsequent dry cycle, which indicated non-recoverable stress due to swelling and loss of solvent through a water-driven solvent extraction.[60-61] Furthermore, these films exhibited

a rapid drop and immediate increase during each change to the wet cycle, consistent with the higher diffusion coefficients from ATR-FTIR. This rapid decrease represented the diffusion of water during immersion to the polymer-substrate interface, which induced a compressive force. Upon additional water sorption, the polymer film swelled, which caused an increase and plateau as the water saturated the film.[94, 187] In the case of films that contained 14 wt% residual solvent, regardless of molecular weight, stress steadily increased. Stress increase was further evidence of the solvent extraction postulated during thermal analysis and immersion measurements. As water replaced the solvent within the film, the sample became less plasticized, resulting in a measurable increase in the internal stress profile. This loss of plasticization correlated with results predicted by the Fox equation, as described in Equation 10.[188]

All of the poly(hydroxyether) films that contained 14 wt% residual solvent exhibited a near linear maximum stress (Figure 4.14 bottom) between wet and dry cycles that increased with each cycle. Because of this, it stood to reason that the original stress was not fully recoverable upon drying the film out. The lack of stress recovery was mirrored in optical transparency measurements in which films had to be exposed to higher heat to regain optical clarity.

The higher molecular weight polymers exhibited a higher degree of internal stress, which would agree with the SEM morphological measurements. As the molecular weight increased, it was likely that chain mobility decreased, which resulted in a decreased stress recovery during exposure and subsequent drying.

Figure 4.15 reports the internal stress profiles for samples that contained 9 wt% residual solvent. From these data, a similar trend of increased internal with sequential cycles occurred.

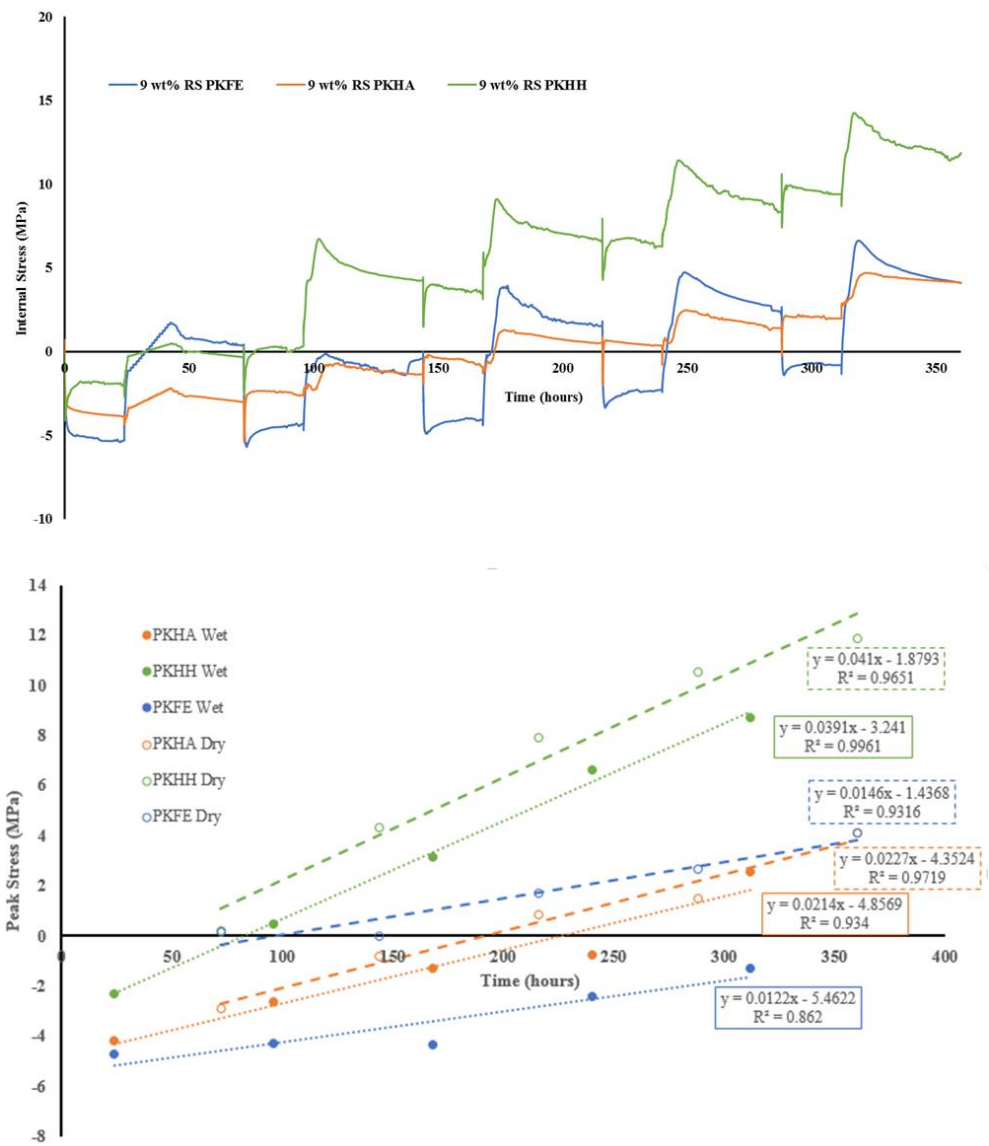

Figure 4.15 Internal stress profiles for PKHA, PKHH, and PKFE containing 9 wt% RSA during cyclical DI water and dry exposure.

(Top) Internal stress of ambient dried films of each polymer molecular weight during wet (24 hours) and dry (48 hours) cycling.

(Bottom) Peak stress before changing from wet-to-dry measurements.

The wet and dry exposures of films that contained 9 wt% solvent also exhibited nearly parallel measured peak stress between the wet and dry exposures. The internal stress profiles of the max stress (Figure 4.15 bottom) indicated that the closeness between wet and dry conditions differed by molecular weight. While the slopes between wet and dry are nearly the same between each molecular weight, the delta value between the trend lines at equivalent time points increased with molecular weight. The differential in wet and dry cycle internal stress measurements implied that the onset and recovery of internal stresses were most similar for polymers of lower molecular weight (PKHA), and increased with increased molecular weight.

Films that contained 6 wt% residual solvent are compared in Figure 4.16. Again, the trend of increasing internal stress was observed. However, a shoulder appeared on the internal stress profile (Figure 4.16 top) that was not exhibited in films that contained more residual solvent than 6 wt% (Figures 4.14 and 4.15). This shoulder was most likely indicative of water binding with the polymer during the immersion cycles and diffusing slower out of the polymer film during the dry cycle. Furthermore, the wet cycles exhibited a distinct plateaued region, whereas the films that contained 14 and 9 wt% residual solvent did not.

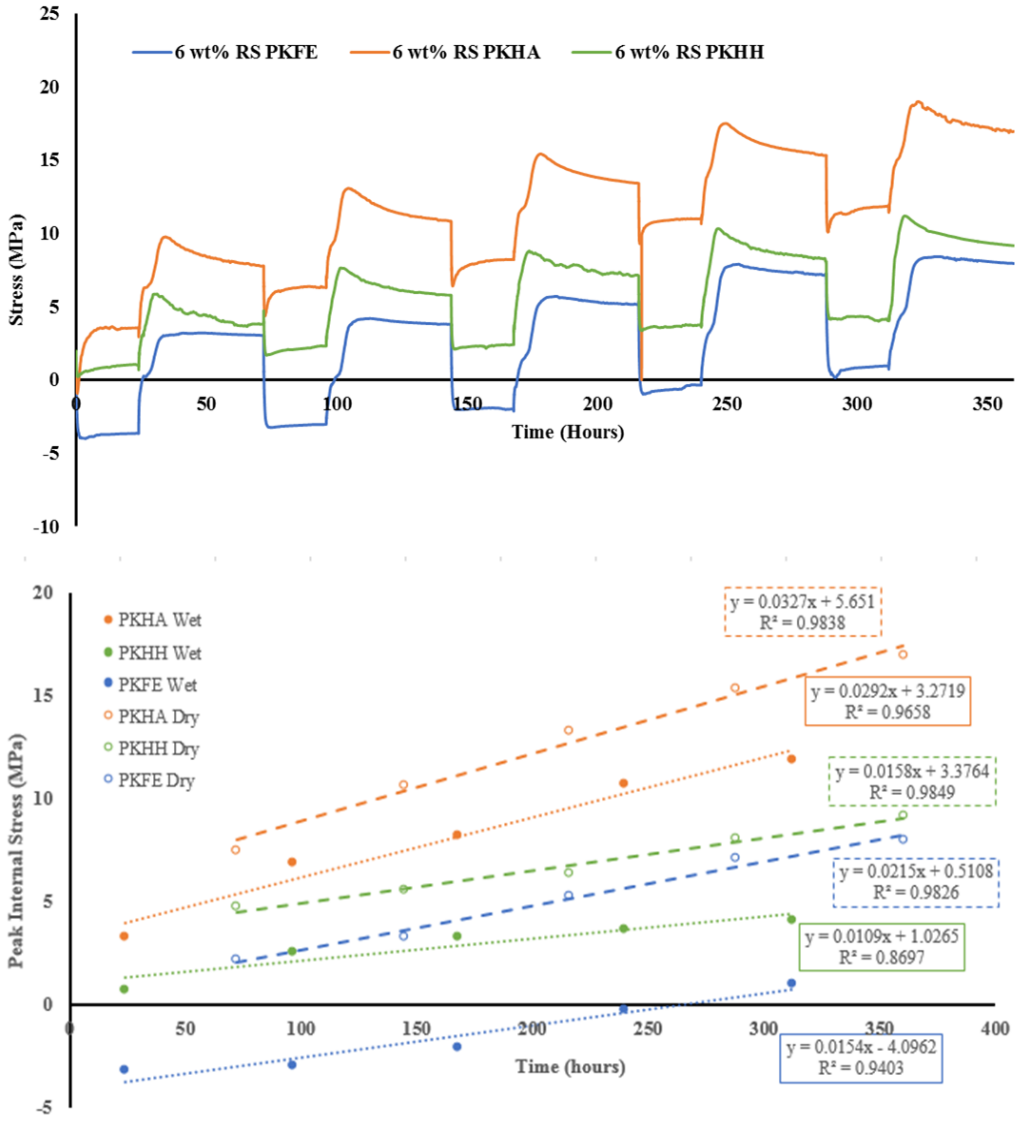

Figure 4.16 Internal stress profiles for PKHA, PKHH, and PKFE containing 6 wt% RSA during cyclical DI water and dry exposure.

(Top) Internal stress of ambient dried films of each polymer molecular weight during wet (24 hours) and dry (48 hours) cycling.

(Bottom) Peak stress before changing from wet-to-dry measurements.

Figure 4.17 compares the internal stress measurements of the different molecular weight polymeric films that contained 1.5 wt% residual solvent. Similarly to the films that contained 6 wt% residual solvent, a shoulder was present on the stress profiles (Figure 4.17 top) during the dry cycle.

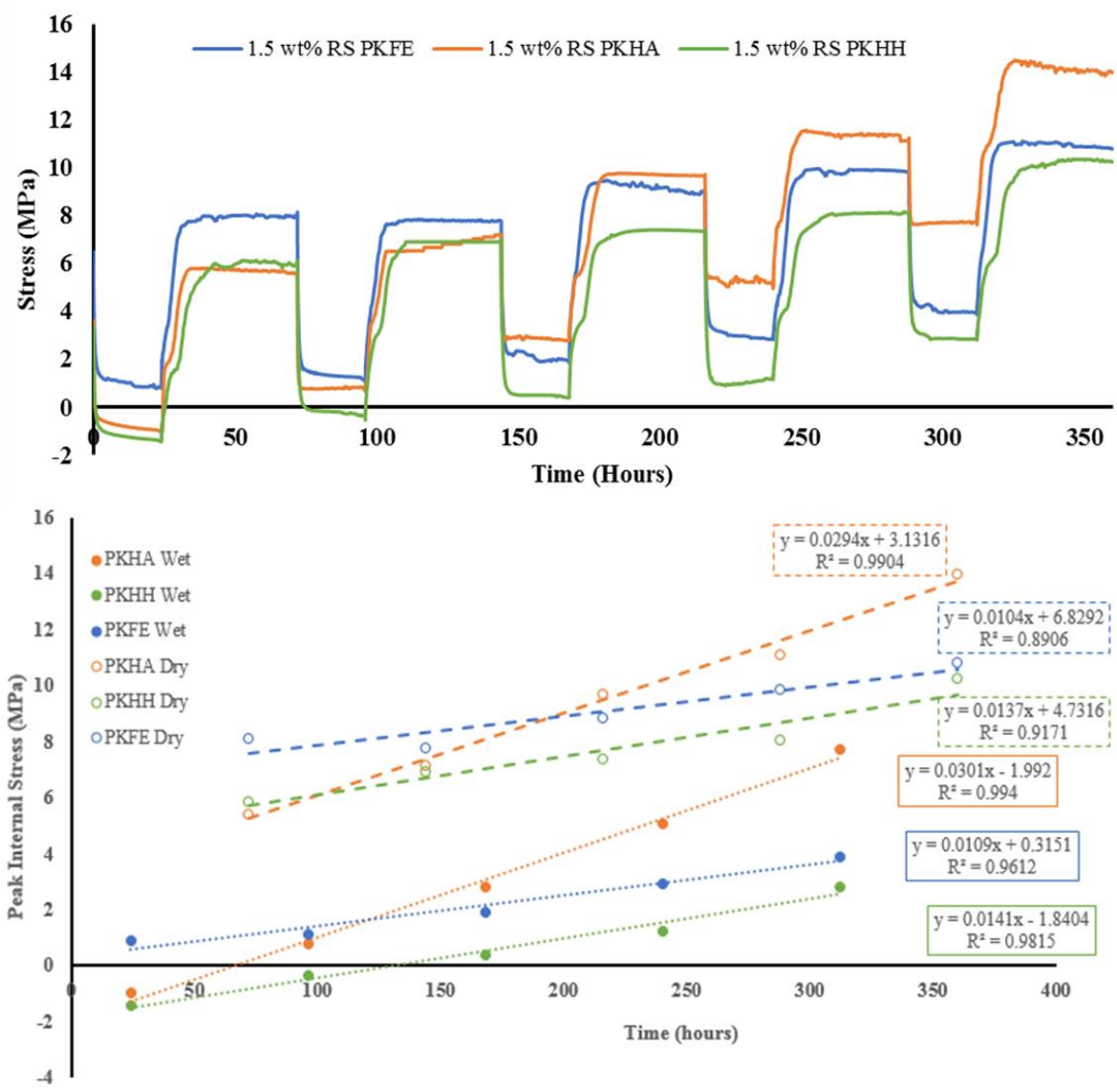

Figure 4.17 Internal stress profiles for PKHA, PKHH, and PKFE containing 1.5 wt% RSA during cyclical DI water and dry exposure.

(Top) Internal stress of ambient dried films of each polymer molecular weight during wet (24 hours) and dry (48 hours) cycling. (Bottom) Peak stress before changing from wet-to-dry measurements.

Again it was hypothesized these shoulders were the result of the removal of bulk water, leading to polymer densification. This densification resulted in more water exclusion from within the bulk matrix, and the evolution of more free water. Higher molecular weight films exhibited a slow increase in measured stress during the dry

cycles, which indicated that water ingress during the wet cycle was slower. These data correlated well with the diffusion coefficients *via* ATR-FTIR measurements. PKHA films exhibited a measurable difference after the second wet/dry cycle, whereby the third dry cycle was 4 MPa greater than the original dry cycle. The rapid increase in stress likely indicated that the lower molecular weight film is more easily swollen during the wet cycle due to a decreased bulk polymer modulus, resulting in easier water removal during early stages in the dry cycle.

Figure 4.18 reports the average change in peak internal stress for each molecular weight poly(hydroxyether). Each value was obtained by subtracting the wet peak stress from the dry peak stress in subsequent cycles, and the values reported herein are the average of 5 cycles. PKHA exhibited a statistical difference for each of the residual solvent levels, whereas PKHH and PKFE both had regions of statistical insignificance. For example, between the 9 and 6 wt% residual solvent samples of PKHH, there was no statistical difference in the peak internal stress differential. Likewise, between the 6 and 1.5 wt% residual solvent samples of PKFE, there existed no statistical difference. The lack of statistical difference further indicated a critical threshold of solvent that still allowed for some molecular rearrangement based on the molecular weight.[189-190] For PKHH, there existed enough molecular mobility at 6 wt% residual solvent to behave similarly to the 9 wt% residual solvent film. A critical loss of solvent was reached at 1.5 wt% residual solvent, whereby the stress remaining in the film was statistically greater than at higher wt% residual solvents. The critical loss of solvent was also observed in the 6 wt% and 1.5 wt% residual solvent films for PKFE.

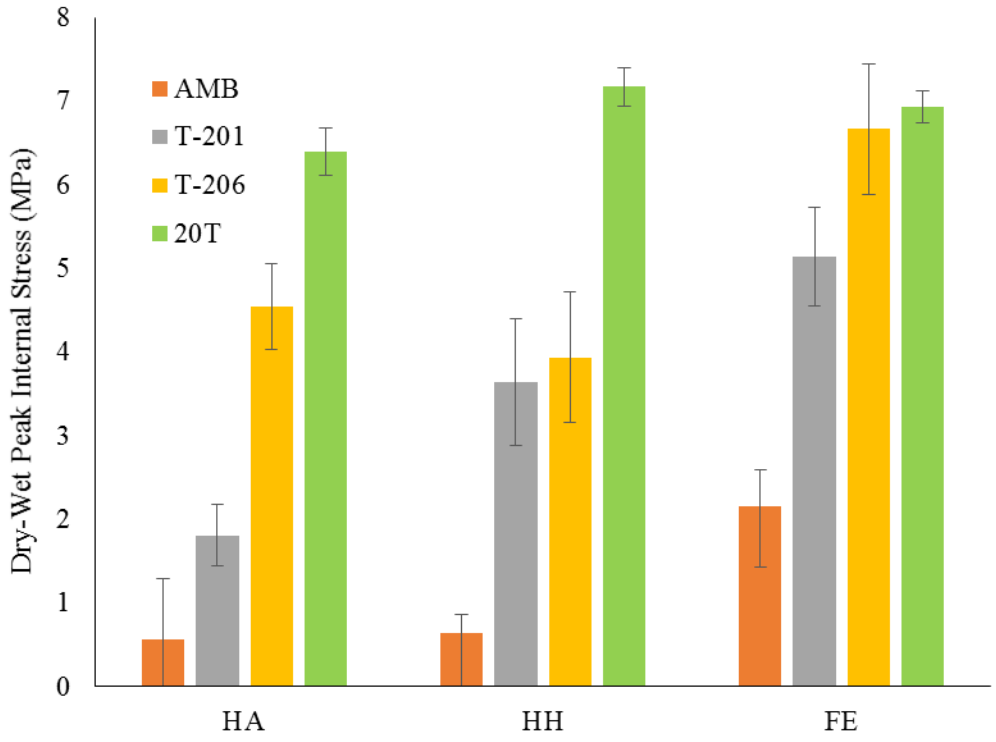

Figure 4.18 Average change in peak internal stress between the wet and dry cycles by residual solvent levels.

Values were obtained by subtracting the wet peak stress from the subsequent dry peak stress and averaging the four values. Error bars are 1 standard deviation from the mean of the aggregated average.

Figure 4.19 was plotted to visualize the impact of molecular weight and for trendlines to be included. These data suggested that the internal stress of a film could be empirically derived for films containing 0 wt% residual solvent by using the y-intercept of the linear fit. Even more surprising was the lack of spread within the y-intercept values. There was only approximately 1 MPa difference between the three vastly different molecular weights (25k, 52k, and 60k g/mol), which suggested that for this polymeric backbone, the residual stress remains approximately the same for films containing 0 wt% residual solvent.

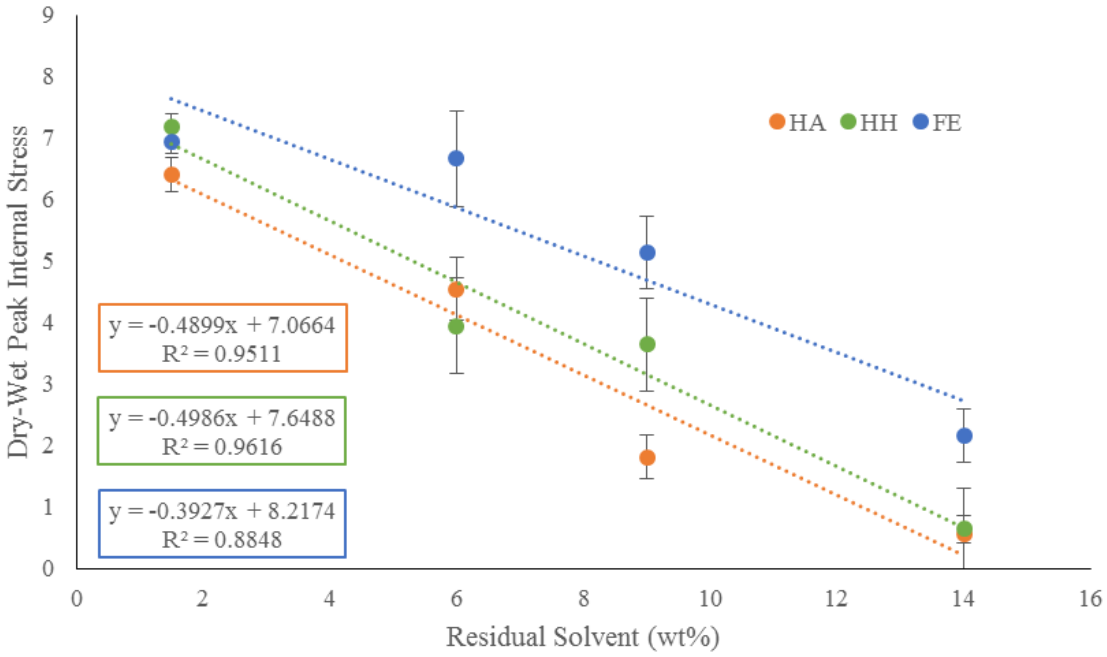

Figure 4.19 Difference in wet and dry peak internal stress values by molecular weight.

Values were obtained by subtracting the wet peak stress from the subsequent dry peak stress and averaging the four values. Error bars are 1 standard deviation from the mean of the aggregated average.

By performing measurements of various polymeric backbones, it may be possible to correlate structure of the polymer with the amount of residual stress that can be measured *via* single cantilever internal stress measurements.

4.2.7 RH-DMA

Figure 4.20 indicates the DMA results for both 0 and 95% RH measurements for both pre and post-exposed PKHA and PKFE films containing 14 wt% residual solvent. RH-DMA afforded mechanical confirmation that the T_g of the films increased after exposure to DI water. Each of the films reported in Figure 4.20 exhibited an increased storage modulus, at both 0 and 95% RH, after they were immersed in DI water for 24 hours.

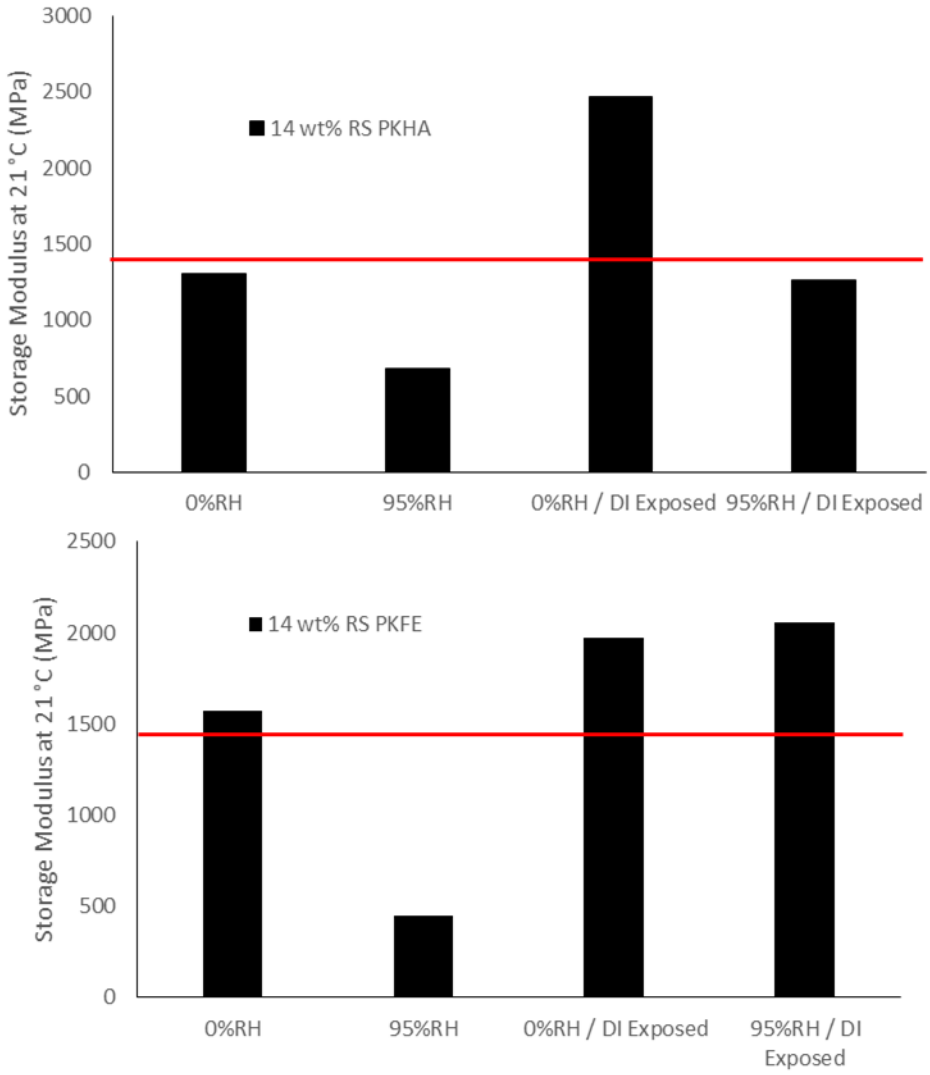

Figure 4.20 Storage modulus at 21 °C for PKHA and PKFE containing 14 wt% residual solvent at 0 and 95 % RH.

In these representative cases (Figure 4.20), films that exhibited a storage modulus of under ~1,450 MPa during the 95% RH measured tensile modulus whitened. This zone is marked by the horizontal line in Figure 4.19. Below the critical threshold, films underwent void formation and subsequent whitening. Films that had a storage modulus of >1,450 MPa did not whiten. A representative storage modulus value comparison of PKFE that contained 1.5 wt% residual solvent is compared in Figure 4.21. Similarly to

the optical transparency measurements, these films did not exhibit whitening during immersion in DI water. The data obtained from RH-DMA also confirmed the extraction of the plasticizing solvent, determined by storage modulus increase after exposure. If the threshold mentioned previously is applied (indicated by the horizontal line), it was apparent that in all measured cases for 1.5 wt% PKFE, the storage modulus never decreased below the critical value. This finding was consistent with the optical measurements discussed earlier in this chapter.

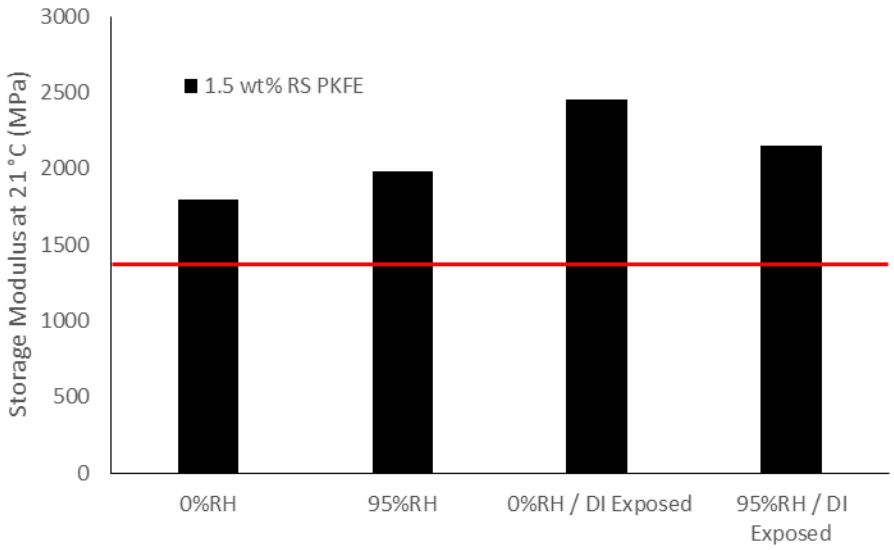

Figure 4.21 Storage modulus at 21 °C for PKFE containing 1.5 wt% residual solvent at 0 and 95 % RH.

4.2.8 Other resins

In order to determine if these same variables (modulus, T_g, residual solvent, etc.) impacted other materials or combinations of materials, an in-service MIL-SPEC thermoplastic used to line water tanks was studied under the same conditions as the poly(hydroxyether)s.

The commercial V-766E tank lining coating was utilized as it is a fully formulated commercial pigmented coating system. RH-DMA was performed to determine the temperature at which the storage modulus in tension reached ~1,450 MPa, which previously was indicated by the poly(hydroxyether) films. Furthermore, surfactants and high boiling point solvents used within the coating should afford water centers for aggregation and void formation. However, unlike the poly(hydroxyether films), the V-766E coating was pigmented, which masked the presences of void formation as the films did not turn optically white. Figure 4.22 reports the cross-section of this coating after exposure to DI water for 24 hours at 30 °C or the threshold at which the film reached ~1,450 MPa, the film was cryo-fractured and SEM analysis was performed to visually determine if voids had formed within the bulk of the film.

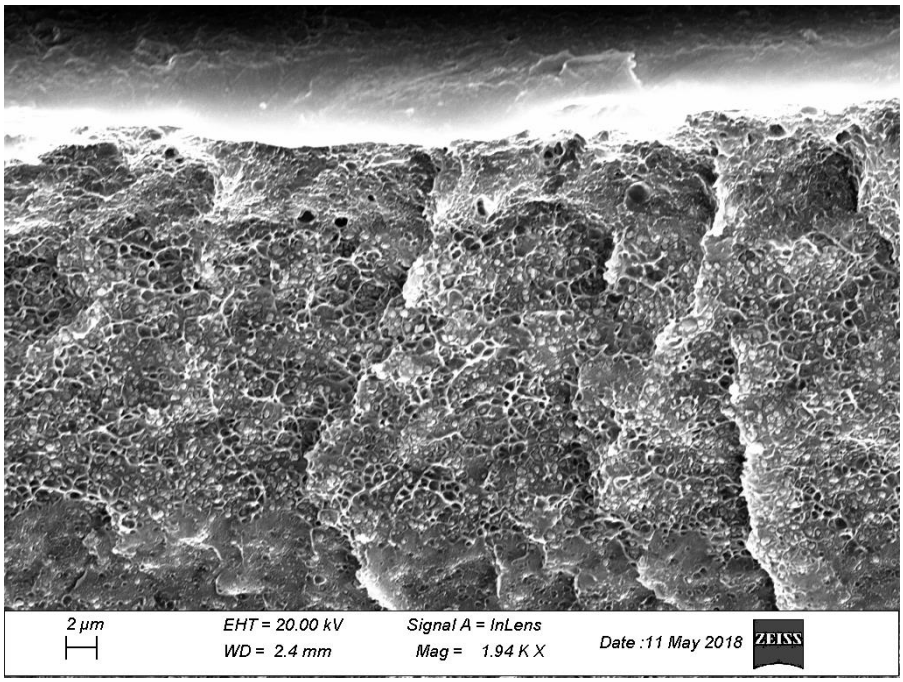

Figure 4.22 SEM morphology of V-766e coating cross-section after 24 hours of DI water exposure.

While the films did not appear white, the presence of voids near the interfaces of the film was observed, as indicated in Figure 4.21. These voids were smaller and did not penetrate as deeply into the coating as the poly(hydroxyether)s did; however, these films were thicker and composed of halogenated polymers, which would result in a slower diffusion of water. Therefore, complete water ingress into the film was not achieved in 24 hours, so voids could not form in the bulk of the polymer.

4.2.9 Conclusions

In this chapter, film whitening was determined to be a direct result of sufficiently sized voids caused by solvent extraction with water. It was believed that these voids formed and grew within solvent-rich domains of poly(hydroxyether) thin films. Similarly, voids were also visually identified within fully formulated commercial coating materials. It is likely that these findings occurred similarly to previous reports on rubber chemistries and acrylics in that a water-soluble species allowed for water accumulation and clustering within the polymeric matrix to create water-rich domains that were phase separated and sufficiently large in both size and difference in refractive index to facilitate a white appearance. In the previously reported cases, these water-soluble species were surfactants or intentionally included salts intended to drive water transport. However, in the case of solvent-borne films, this same phenomenon was realized with water-miscible solvents that were originally used to cast the films. When higher levels of residual solvent were present in the film, there was a more significant degree of whitening within the film, larger voids, and a faster void growth rate. This whitening was directly correlated to the polymer molecular weight as well, as indicated by the fact that higher molecular weight films were more resistant to whitening during room temperature DI

water exposure. The lack of whitening in the higher molecular weight films was likely caused by a higher polymer modulus under a given set of conditions, greater polymer entanglement and higher energy required to bend/stretch the polymer chains apart. Optical transparency was measured via percent light transmission and provided a facile measurement to monitor the frequency specific whitening of the films *in situ* and allowed for the direct comparison between each polymer molecular weight with measurable T_g differences and residual solvent concentration. SEM was used to monitor and capture images of the void formation by utilizing a cryo-fracture process to directly interrogate the polymer morphology of the air interfaces and the internal bulk surface of the film, after both free film and substrate-bound exposures.

Moreover, the substrate-bound internal stress results corroborated the microscopy and optical transparency data, i.e., internal stress measured within samples containing minimal residual solvents shifted between wet and dry values, but remained relatively unchanged in magnitude throughout multiple environmental exposure cycles. The lack of change in the wet-dry differentials of internal stress confirmed that the wet and dry polymer properties and morphology were, in the main and as currently quantifiable, recovered after exposure. Films annealed above the polymer-specific T_g (driven to the range of 1.5 wt% residual solvent samples) did not exhibit definitive whitening when evaluated during exposure to DI water at ambient temperatures. The 14 wt% residual solvent exposed films exhibited rapid whitening and shifted from whitened to optically clear films during wet-dry cycling, which indicated changes within the film, captured with SEM measurements. Through higher solvent concentration and hydroplasticization, *in situ* formed voids were more substantial due to the allowed greater polymer mobility,

and reduced modulus. These combined results confirm that surface coating materials cast for film formation with the potential of trapped residual solvents and even low water affinity are prone to physical void formation after application, cure, and annealing during environmental exposure. These voids directly result in different physical properties, transport, and adhesion performance.

Of more significant contribution was the determination that above storage moduli of 1,450 MPa, films did not whiten or whitened at a much slower rate. Films below 1,450 MPa whitened rapidly, often diminishing to less than 10% transparency after just 3 hours of exposure to DI water. These data may be related to results found in the biological sciences, as the theoretical pressure driven by water cohesion and tension should achieve 1,400-1,500 MPa, which would supply sufficient osmotic pressure to create voids within the polymeric films when the polymer was in a solvent plasticized state that allowed water pressure limits to shift concentration and distribution.

This Chapter indicated several organic coating attributes that could be adjusted (e.g., residual solvent content and composition, polymer molecular weight and corresponding modulus and T_g, exposure conditions) to alter the induction period prior to macroscopic changes, whether those changes are visual corrosion or film whitening. By reducing the residual solvent in above virgin polymer T_g annealed films to approximately $1/10^{th}$ of the ambient dried film, the induction period for film whitening was increased by at least>4x, but likely longer. This lack of residual solvent also correlated to a 4x increase in the storage modulus of measured films at 95% RH.

CHAPTER V –DETECTION OF PRE-MACROSCOPIC CORROSION EVENTS UTILIZING pH SENSITIVE FLUORESCENT PROBES

5.1 Objective

The objective of this work was to quantifiably demonstrate the ability of a pH-sensitive probe, fluorescein (FSCN), to detect corrosion in a spatially specific manner on steel substrates. It was hypothesized that the pH at the cathodic delamination front would be sufficiently high that FSCN would be able to accurately detect and quantify the extent of cathodic delamination. In the case of fluorescent detection, it was believed the FSCN embedded in the polymer that was in direct contact with the heterogeneous reaction space between the substrate and the polymer detected cathodic delamination driven OH^- production such that the concentration of OH^- and ability for FSCN to interact with these OH was believed to be the rate-limiting step for detection of fluorescence increase. To further elucidate organic coating properties that affect detection, again poly(hydroxyether) molecular weight and residual solvent levels were utilized as tunable variables, i.e., altered to intentionally shift the timing for each system's "induction period". It is critically important to reaffirm that each of these polymers, albeit different molecular weight, are based upon the same identical building blocks. Therefore, while the molecular weights were different, the T_g of conditionally dried and annealed films and their corresponding moduli were the parameters of interest. By altering the T_g with respect to ambient exposures, differences in mechanical properties and barrier properties, with respect to the residual solvent content were adjusted to force shifts in the "induction period" to detect difference in material properties early and *in-situ.* HPTSA fluorescence was utilized to offer a comparison to more traditional spectroscopic methods such as

FTIR and was effective at measuring the rate of water saturation of the model polymeric film. Through this work, quantifiable correlation of increased fluorescence of a pH-sensitive probe to the cathodic delamination mechanism exhibited by steel and zinc-plated substrates as measured by scanning Kelvin probe was achieved. Furthermore, the limitations of the use of fluorescein on aluminum alloys due to the indiscreet nature of the corrosion process induced by the alloying process is discussed.

5.2 Results and Discussion

5.2.1 Fluorescent Response

In order to measure the response of FSCN to its environment, the wet and dry response based on concentration in the solvent was determined. As the films prepared were cast from solvent, FSCN's response to the solvent needed to be qualified. These data are reported in Figure 5.1 where the fluorescent response of solvent-dispersed and dried FSCN was graphed against the concentration.

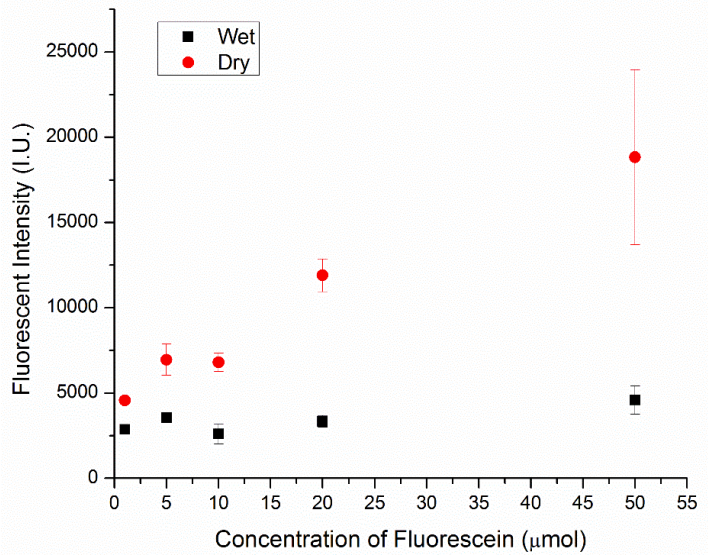

Figure 5.1 Fluorescent intensity of FSCN in both the wet and dry state.

From these data, the fluorescent intensity was higher for fluorescein in the dry state, i.e., after the solvent had evaporated than in the wet state (solvent-borne). The aprotic nature of anhydrous THF caused the fluorescein to remain in a non-ionic, specifically, a largely lactone state (Figure 1.10, Chapter I). Upon evaporation of the solvent in the open air, water was able to cause a local environmental shift due to humidity, altering the ionic state of fluorescein to that of neutral, ring-opened, or even anionic state. By undergoing a tautomerization or change in protolytic form, the fluorescence intensity increased. Furthermore, as the solvent evaporated the molecular motions of fluorescein became constrained, causing more absorbed energy during excitation to be emitted as fluorescence. Once the fluorescent response was determined for the solvent, FSCN was incorporated into poly(vinylbutyral) films at different concentrations to determine the correct concentration for future measurements. Figure 5.2 depicts the fluorescence spectra and peak intensities based on the concentration within the PVB film. PVB was utilized as it was cast from a protic solvent, which shifted the protolytic species towards to the quinoid and zwitterionic states, which exhibited both an absorption and weakly fluorescent signal.

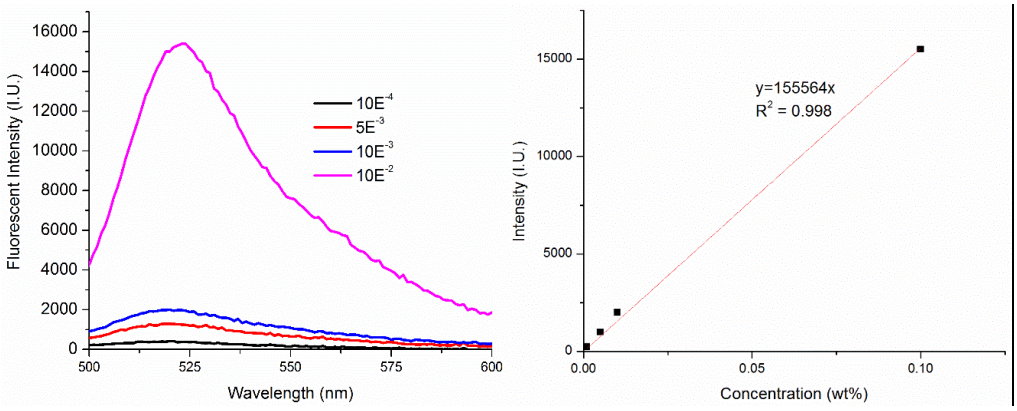

Figure 5.2 Fluorescent intensity for different [FSCN] in solvent-borne resin.

Spectral emission scan (left) and peak emission intensity (right) with respect to concentration.

The fluorescent intensity linearly increased (Figure 5.2 right) at each concentration measured which indicated that the probe concentration was below the threshold for self-quenching at all concentrations.[191] Due to the sharp response at $10E^{-2}$ wt% FSCN, subsequent samples were prepared at $1.7E^{-2}$ wt% FSCN against resin solids. Preparing the samples at this concentration ensured that upon increasing the pH of the local environment, the fluorescein response would not overwhelm the fluorescent detector within the fluorimeter, but was sufficiently high enough concentration to measure pH changes.

Additionally, to ensure the fluorescein was being dispersed in the film and was not aggregating, UV-Vis was utilized to measure the absorbance of FSCN in both the solution (cuvette) and in the dried resin (glass slide), demonstrated in Figure 5.3. While the concentration of the FSCN remained constant between these samples, the number of molecules excited during measurements decreased in the film as it is more compact and does not exhibit the Brownian motions that occur in solution. The peak width of each measurement provided a qualitative measurement of aggregation of FSCN within the film. If FSCN aggregated or resulted in regions of inhomogeneity, literature has shown that a peak broadening would have been observed.[192-193]

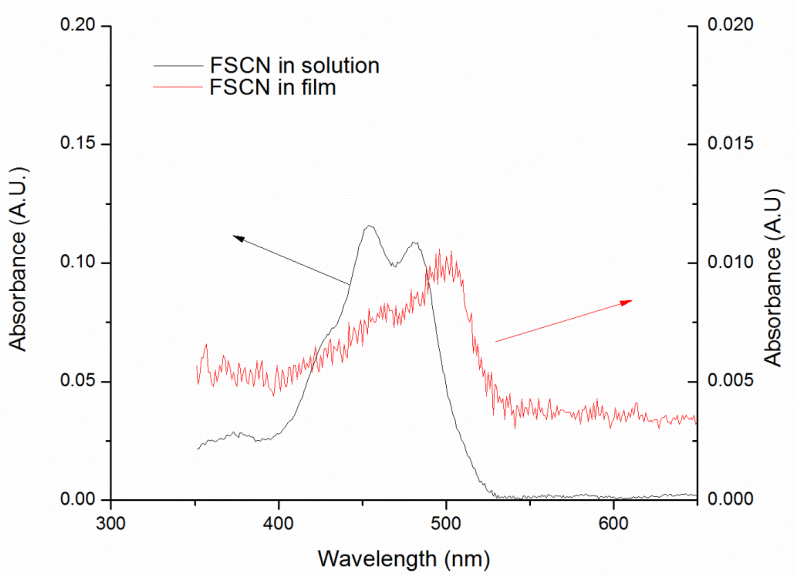

Figure 5.3 Absorbance profiles for FSCN in a solvent-borne resin vs. in a dry film.

The measured absorbance for FSCN in solution was higher than that of the polymer, which was expected. Furthermore, there was a slight blue shift to the absorbance values of the fluorescein in PVB likely caused by interactions such as hydrogen bonding with the polymer. However, the peak width remained approximately the same for both the solution (88 nm) and the polymer cast FSCN (94 nm), indicating an effective dispersion of FSCN was achieved and there was little agglomeration of the fluorophore within the PVB. The fluorescent response was measured on glass slides to ensure FSCN still exhibited the pH responsiveness once incorporated into the resin. FSCN was dispersed into PVB and cast from ethanol and measured for a baseline fluorescent response. To artificially force a pH change, a 2M NaOH (pH ~14) solution was placed on the surface for 10 minutes. The non-exposed and NaOH exposed data are reported in Figure 5.4.

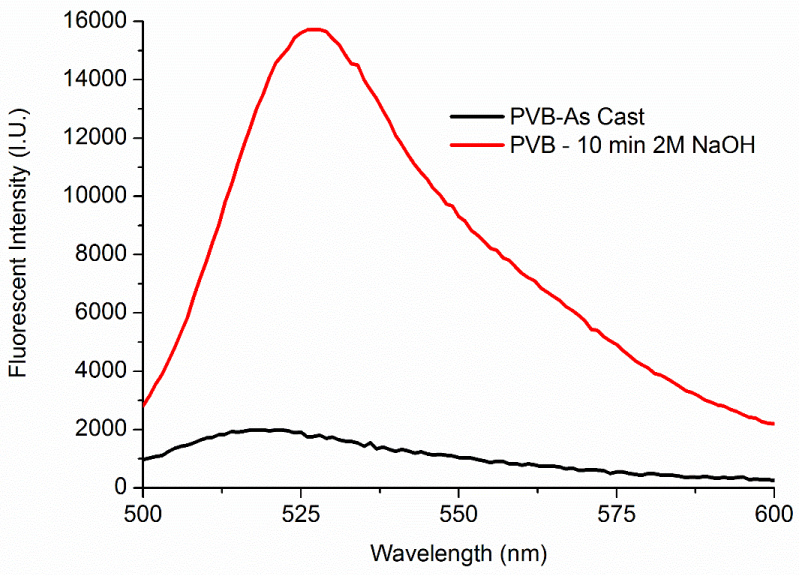

Figure 5.4 Fluorescent intensity of a film containing FSCN as cast and after exposure to 2M NaOH.

Figure 5.4 indicated that the pH responsiveness of FSCN was not altered by the polymeric film in such a way that inhibited the use of FSCN. Upon exposure, the fluorescent intensity increased by 4x after 10 minutes, which further indicated that FSCN could be used to detect pH changes within the film.

During corrosion, the development of cathodic and anodic regions occur and have distinct pH profiles. To determine the response of FSCN as a probe to monitor corrosion, FSCN was dispersed into PVB and cast on a steel substrate. Following the Stratmann geometry discussed in Chapter II, cathodic delamination was forced to occur. Direct measurement of the delaminating edge and comparison to the intact coating was enabled through the use of the Stratmann geometry. Figure 5.5 summarizes the fluorescent response of a PVB film both at the delamination front and away from this region. The image inset in Figure 5.5 indicated where the two separate measurements were performed.

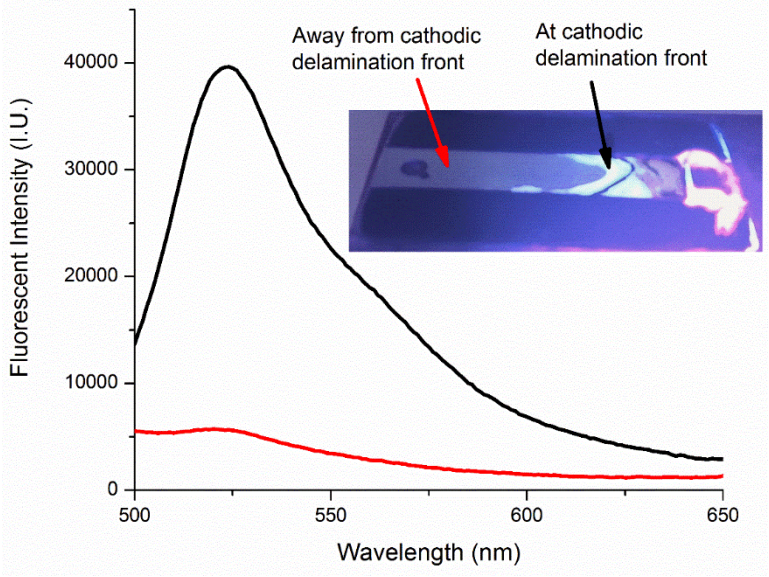

Figure 5.5 Fluorescent response of a delamination cell both at and away from the delamination front.

The leading edge of the cathodically delaminated region was visually observed in the image inset in Figure 5.5. At the delaminated front, it was expected that the reduction process in the corrosion mechanism would yield OH^- species causing a locally elevated pH that would be detectable with FSCN. The sample was allowed to delaminate for 72 hours to produce a defined region so that the sample could be measured in the fluorimeter while being spatially defined. The fluorescent response at the delamination front resulted in an 8x increase in intensity compared with unexposed sample area, thus qualitatively confirming that FSCN could be used to monitor the cathodic delamination of an organic film during the corrosion process.

The polymer-rich film was mostly aprotic; however, upon water absorption, it was expected that the local environment would become protic. To ensure FSCN was responding to the pH change rather than the change to a protic environment, FSCN was

dissolved in anhydrous THF and was dosed with specific amounts of water to increase the polarity of the solvent (Figure 5.6).

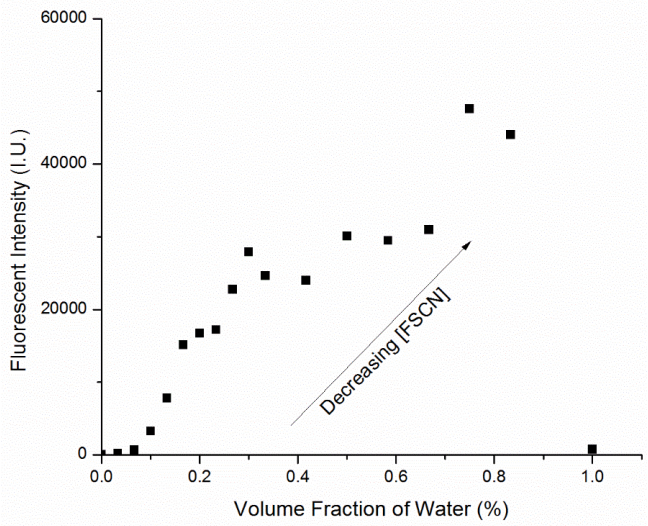

Figure 5.6 Fluorescent intensity of FSCN in anhydrous THF with increasing water content.

Figure 5.6 reports the fluorescent intensity of FSCN dissolved in the THF phase with increasing water content. In this experiment, the concentration of FSCN decreased with increasing water content, as it was dissolved in the THF phase before dosing with water. However, the fluorescent intensity also increased. While the effective concentration was lower with increased water content, the increased intensity suggested that water alone was enough to cause a fluorescent signal increase.

To further confirm that the change in intensity of FSCN directly attributable to water, a second experiment that utilized an equimolar concentration of fluorescein in both the water and THF phase such that the total effective concentration of FSCN did not change upon addition of water to the THF was performed. Figure 5.7 indicated the same

trend response, whereby the fluorescent signal increased with increasing water content, even at equimolar concentrations of FSCN.

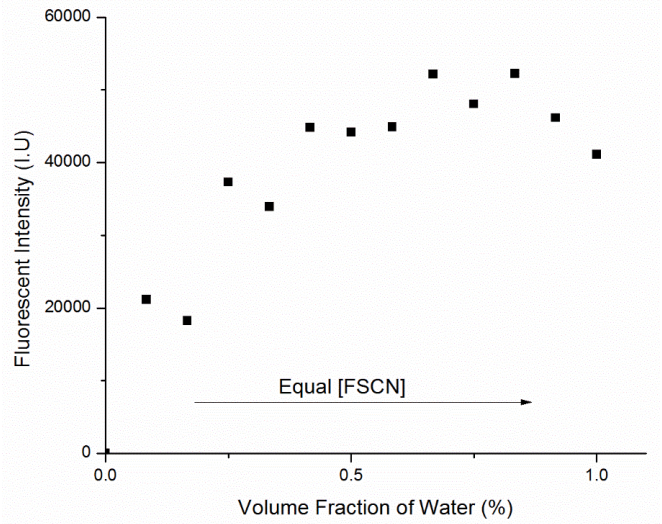

Figure 5.7 Fluorescent intensity of equimolar water and anhydrous THF blends.

Due to FSCN responding to water in the liquid phase, RhB was added as an environmental control. While RhB does not fluoresce to the same extent as FSCN, they are both affected by environmental conditions. During water immersion and corrosion measurements, when water entered the film, it was possible to delineate the causes of fluorescence increase. When the RhB signal plateaued, any additional increase in the FSCN intensity was attributed to a change in local pH rather than the change in the localized protic environment, i.e., water concentration.

For validation of the aforementioned concepts, water addition to an RhB containing solution was used to determine the fluorescent response of RhB to changing local environment conditions (i.e., more water), similarly to those performed with FSCN. RhB was dissolved in the PGME and water was added sequentially to provide a similar graph to Figure 5.6. As reported in Figure 5.7, an increase in fluorescent intensity at low

concentrations of water followed by a plateau with additional water concentration increase was observed. Again, while the effective concentration of RhB decreased, the fluorescent response increased initially and then remained constant. RhB and FSCN are both affected by the local shift in polarity at low concentrations of water. Furthermore, this knowledge allows for the relationship of RhB and FSCN to determine an apparent pH based on ratiometric calculations. Thus, RhB was incorporated into coatings with FSCN to provide an internal standard during fluorescent spectroscopy.

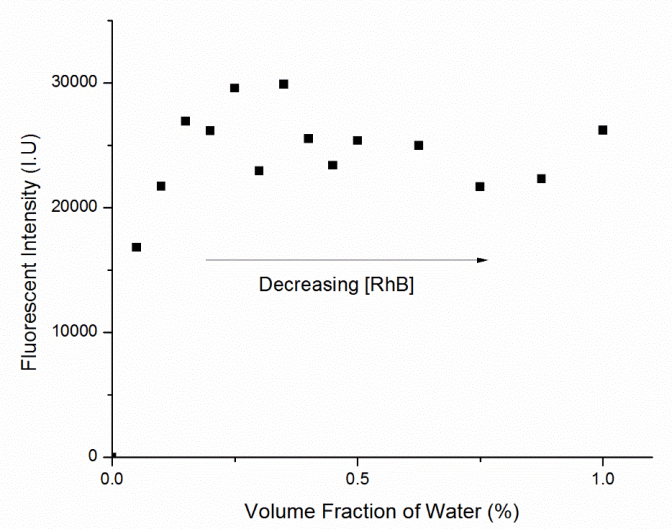

Figure 5.8 RhB response to the addition of water.

Because the FSCN and RhB both are environmentally sensitive, but FSCN is pH sensitive, an effective pH can be determined by taking the ratio of each of these measurements in a dual probe film. While this is not an exact pH as there is a limitation due to the solid polymeric film inhibiting a direct interrogation of the pH gradient, an apparent pH can be determined by plotting the ratio of the intensities of FSCN/RhB. The measured ratios can then be compared to a calibration curve in which the ratios were measured at known pHs, indicated in Figure 5.9. FSCN exhibited a linear response from

pH ~5-9, limiting the valid range for a calibration curve to this region. Other probes could be used in a cocktail to increase the breadth of pH ranges detectable.

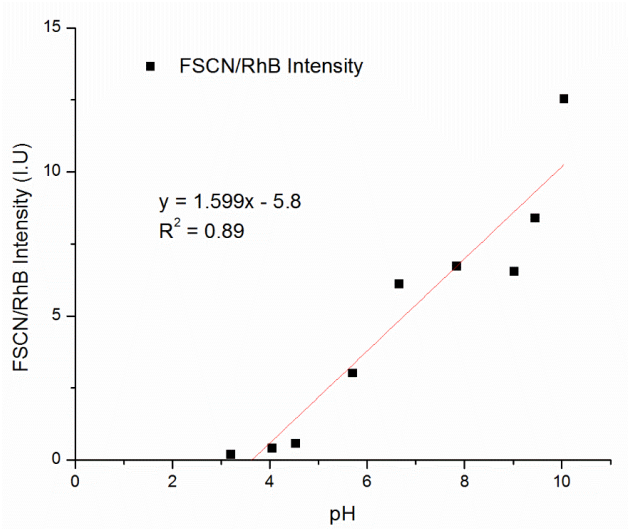

Figure 5.9 FSCN/RhB ratiometric calibration curve.

Due to the knowledge obtained concerning internal standard comparisons, RhB was incorporated into every film to monitor environmental effects, while FSCN could then be used to monitor pH changes exclusively due to the corroding substrate.

While it was shown that FSCN is pH-responsive in this study and it is known the corrosion reaction produces regions of distinct pH gradients, SKP was used to directly interrogate the substrate while the corresponding fluorescent measurements were collected for comparison.[100, 102, 194] These correlative measurements supported the hypothesis and confirmed with certainty that FSCN actually measured the corrosion response from the shift to basic (>7) pHs at the substrate-polymer interface.

5.2.1.2 Water-induced fluorescence

Water sensitive probes were utilized to determine if water could be spatially defined within the polymer thin film. HPTSA has been shown in the literature to detect water in organic solvents. Thus it was adopted for use in solvent-borne clear coats.[195]

Figure 5.15 compares the fluorescent response of HPTSA containing poly(hydroxyether) films during exposure to DI water. A slight fluorescent signal was observed in the film before exposure to DI water (Figure 5.15A). After 3 hours of exposure to DI water, a sharp increase in the fluorescent intensity was recorded (Figure 5.15C).

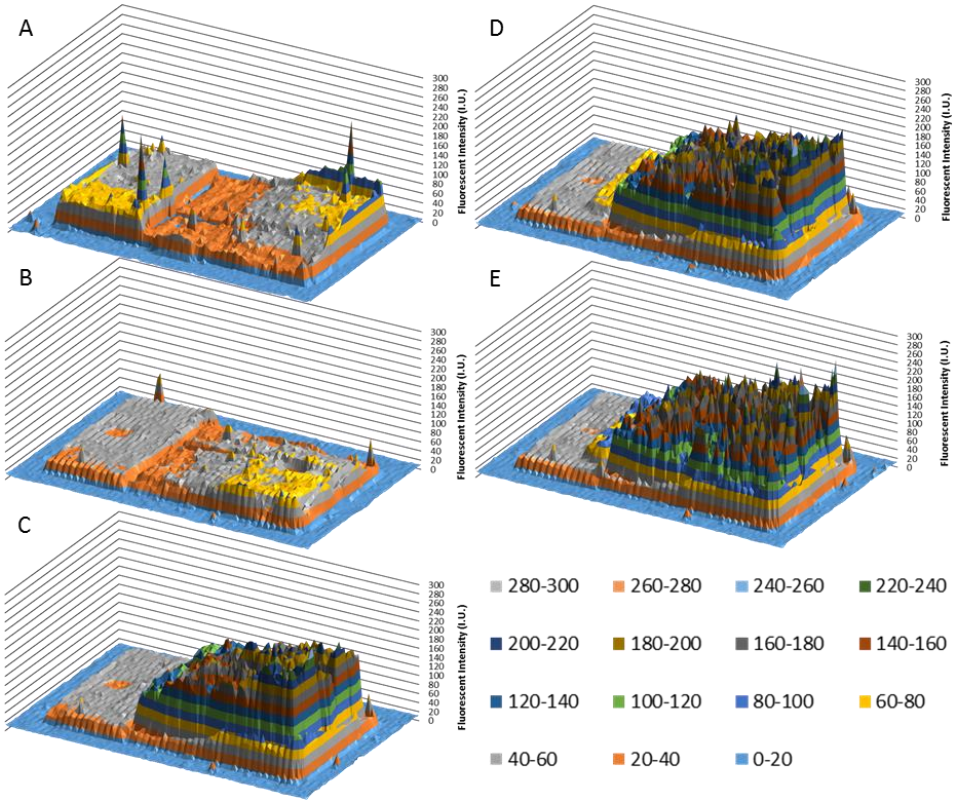

Figure 5.10 Fluorescent scans of HPTSA-containing PKHH during immersion in DI water

PKHH pre-exposure (A), after 1 hour (B), 6 hours (C), 12 hours (D), and 24 hours (E) of exposure to DI water. For clarification, the exposed area is on the right-hand side of each image, while the taped, non-exposed region is on the left.

Upon further exposure (Figure 5.10D and E), a plateau and decrease in the fluorescent intensity were observed. Figure 5.11 reports the average fluorescent intensity of the panels shown in Figure 5.10 with respect to time. A substantial increase in the fluorescent response of the panel that was exposed due to water ingress after 3 hours was observed from this data. After 3 hours, there was a slight additional increase in the fluorescent intensity. After immersion for 6 hours, there was no further increase in the measured fluorescent intensity. After this point, a loss of intensity was observed. It was believed that the polymer film had swelled sufficiently that a loss of resolution of the fluorescent probe had occurred. However, these data correlate with ATR-FTIR measurements that water was rapidly sorbed into the polymeric film. The fluorescent intensity increase and saturation limit observed with HPTSA directly correlated with the linear region of the water diffusion curves shown previously (Figure 4.11).

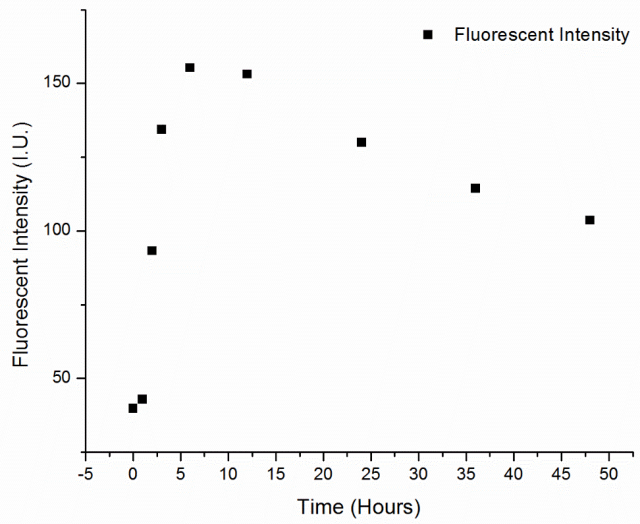

Figure 5.11 Average fluorescent intensity of HPTSA-containing PKHH exposed to DI water.

These data provided another experimental technique from which water penetration into the coating could be estimated and possibly measured. By incorporating

HPTSA, RhB, and FSCN into the film, it was possible to account for more of the overall process, water uptake, swelling, and corrosion all in combination. However, because of the spectral overlap of HPTSA and FSCN, these probes should be used in pairwise experiments, rather than incorporated as a cocktail to avoid confounding self-induced fluorescence.

5.2.2 Scanning Kelvin probe

Scanning Kelvin probe was utilized to monitor the cathodic delamination of poly(hydroxyether) and acrylic thin films from mild steel substrates to quantitatively determine the relationship between FSCN and SKP. Figure 5.10 summarizes the 3-dimensional contour plots obtained from scanning in the X and Y planes, while the Z-axis represents volts, as measured against a standard hydrogen electrode (SHE).

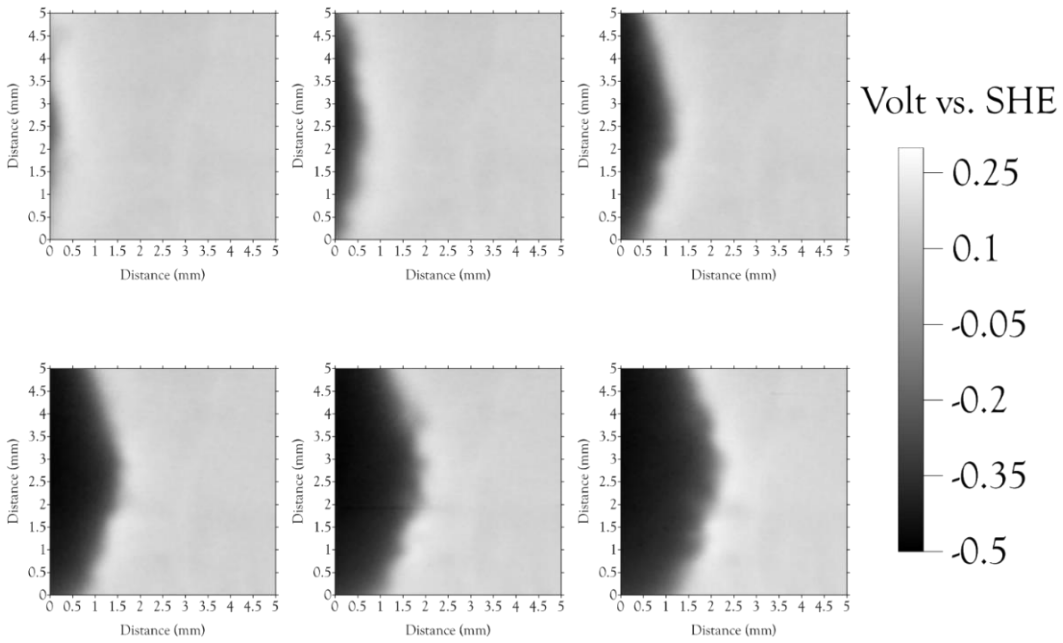

Figure 5.12 Time-based SKP potential map of PKHA containing 6 wt% residual solvent. Scans were performed every 2 hours.

The lighter regions represent adhered polymer in which there is a more positive potential as the substrate has not begun corroding. As time progressed, the potential became more negative, especially near the periphery of the delaminating film. The progression of the delaminated (or more negative) region correlated well with literature discussions. Once the film wholly delaminated, a potential of ~450 mV was measured, which was indicative of a freely corroding iron substrate. This area was indicated by the near black regions on the contour plots in Figure 5.10. Over time, this region became larger as the delamination front progressed outwards from the defect.

The potential versus distance data was then averaged to show individual measurements in a 2-dimensional fashion to measure the kinetics of the cathodic delamination. Figure 5.11 indicates the potential versus distance from the defect in a time-based fashion. The potential versus distance curve for 14 wt% RS PKHA (25K g/mol) was representative of the whole scribed region measured. Due to the length of time for each scan and the variability of corrosion occurring in regions during this time, measurements were only performed on half of the scribe. In doing this, measurements could be performed every 1-2 hours rather than the 5 hours required for measuring the entire area. To demonstrate that the measured delamination front was not impacted by only scanning half of the scribe, a dotted line was place in 14 wt% PKHA where the scribe was located. The resultant profiles maintained similar sigmoidal curves as the scans performed on only half of the scribed region.

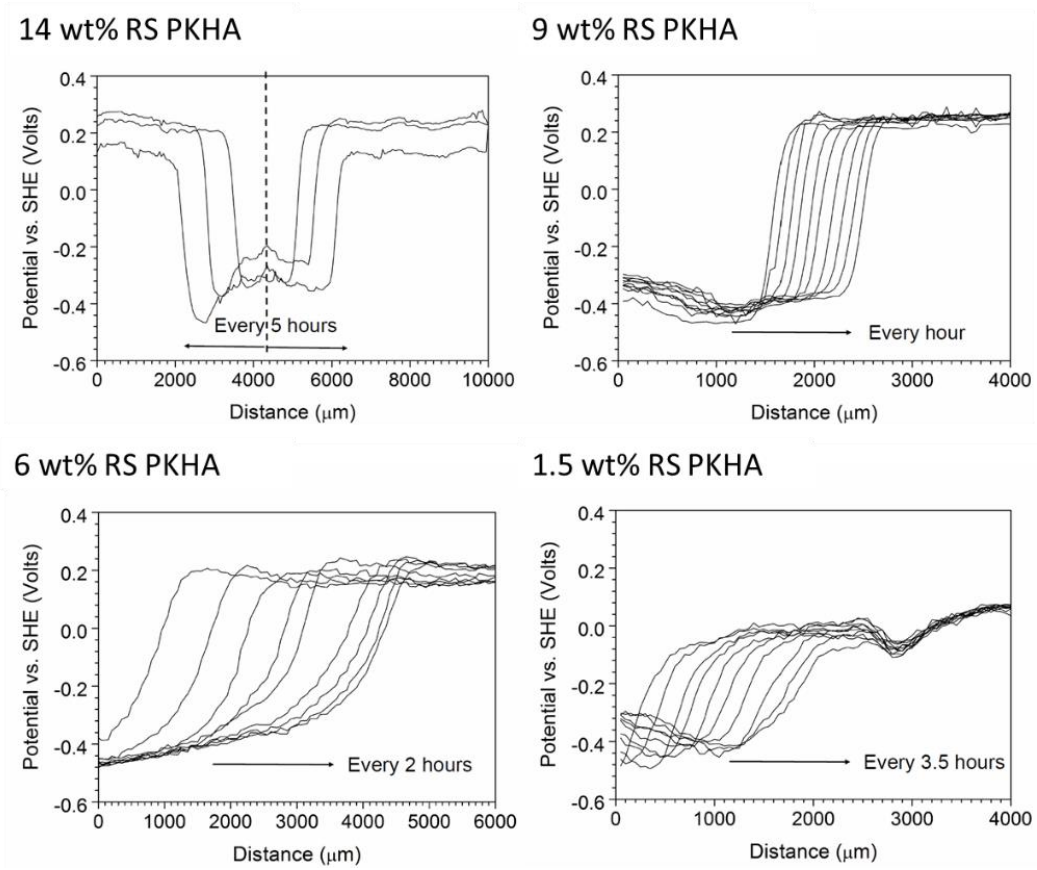

Figure 5.13 Potential vs. distance profiles for PKHA at different residual solvent levels measured via SKP.

Samples were measured that contained 14 wt% residual solvent, 9 wt% residual solvent, 6 wt% residual solvent, and 1.5 wt% residual solvent.

An increased residual solvent content resulted in the cathodic delamination front moving further away from the defect in shorter time spans. The increased rate of cathodic delamination was a direct result of a decreased adhesion to the metal substrate, as well as the ability of water to transport along the coating-metal interface easier due to the water miscibility of the solvents used in spray applying the poly(hydroxyether) film. The measurements were performed near the scribe, indicated by distance = 0 μm in Figure 5.13 and 5.14, with increasing delamination distance as time progressed. Further away from defect (increasing x-axis), a steady potential of 200-300 mV versus SHE was

measured, which indicated that the film remained intact and no corrosion occurred under the film. As time progressed, the delaminated region extended further from the defect, indicated by the sharp increase in potential. The extent of change in the x-axis was indicative that cathodic delamination had occurred and the diffusion of cations to the reduction site had occurred such a loss of adhesion, along with the corroding substrate, produced a delaminated film. The measured corrosion potential was *ca* -450 mV, again, indicative of freely corroding iron. While each of the curve shapes are slightly different, there is no literature discussion of the shapes outside of the distinct regions discussed: most negative potential indicated the delaminated coating, a sharp transition from negative to positive potentials which was indicative of the cathodic delamination front, and the positive potentials which indicated an intact coating. Representative scans are reported in Figure 5.14 to demonstrate the effect of molecular weight and chemistry on cathodic delamination. Both of the plots in Figure 5.14 represent a coating that contained 14 wt% residual solvent; however the left graph was representative of PKFE (60K g/mol) and the right graph was a commerical acrylic co-polymer.

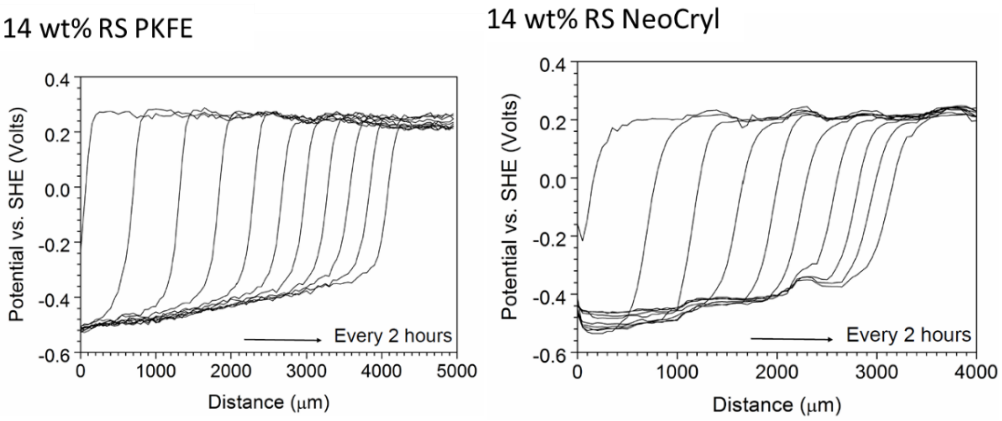

Figure 5.14 Potential versus distance SKP scans for PKFE and NeoCryl containing 14 wt% residual solvent.

From these data, it was observed that while the molecular weight and chemistry both impacted the delamination rate, each of the rates for PKFE and NeoCryl was similar to the PKHA films that contained 14 wt% residual solvent, which indicated that the residual solvent has a more significant impact on the cathodic delamination rate than the polymer molecular weight (25K versus 60K g/mol) or chemistry (poly(hydroxyether) versus acrylic co-polymer) when cast from the same solvents. To better understand the impact of chemistry, more thermoplastic polymers would have to be measured. E_{corr} values obtained from Figure 5.13 and 5.14 were plotted against measurement time to determine the actual delamination rate, and are compared in Figure 5.15. The distance at which E_{corr} was measured, with respect to the square root of time for parabolic corrosion kinetics resulted in the measured corrosion rate from the slopes indicated in Figure 5.15. It is important to note that the trend lines do not cross through 0,0 as would be expected due to the conditioning step utilized to achieve an equilibrium surface water content required to minimize surface charging during the measurements. Therefore, 0 on the x axis in these data are represented as the first measurement, rather than the start of conditioning in which some delamination may have already occurred.

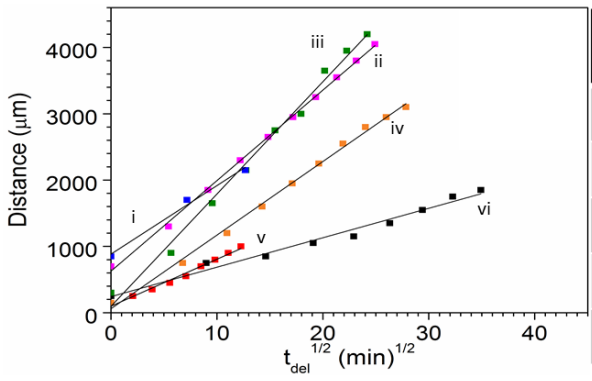

Coating	Delamination Rate (μm/min$^{1/2}$)
14 wt% RS PKHA	103.3
14 wt% RS PKFE	136.5
14 wt% RS NeoCryl	111
9 wt% RS PKHA	70.9
1.5 wt% RS PKHA	44.7

Figure 5.15 Delamination time vs. distance for each coating system.

i) 14 wt% RS PKHA; ii) 14 wt% RS PKFE; iii) 6 wt% RS PKHA; iv) 14 wt% RS NeoCryl; v) 9 wt% RS PKHA; vi) 1.5 wt% RS PKHA.

On a molecular weight comparison, 14 wt% residual solvent PKHA and PKFE measurements resulted in similar cathodic delamination rates, although the PKFE rate was slightly greater than PKHA. Across different chemistries (i.e., acrylic versus poly(hydroxyether) at the same 14 wt% residual solvent, the delamination rate measured with SKP was relatively similar. Comparatively, decreased residual solvent present in the film also decreased the cathodic delamination rate. Increased residual solvent in the film likely allowed for easier water and ion transport to the delamination site through the water-miscible solvent. The lower residual solvent films also demonstrated better pull off adhesion, which suggested an increased intimacy with the steel substrate. The SKP data were collected to afford direct comparisons with fluorescent spectroscopy on identically prepared films.

5.2.3 Fluorescence

Fluorescence was compared with the delamination rates measured from SKP due to the wide acceptance of SKP in determining cathodic delamination rate in literature. From the corrosion process and evidenced by the qualitative measurements obtained, it

was expected that FSCN would accurately measure the cathodic delamination rate, albeit with a small time lag due to the concentration of basic species that would cause a pH increase. Figure 5.16 reveals a representative image of time-lapse monitoring that utilized a confocal laser scanning microscope. The image was then overlaid with a polarized light microscope to observed developments of micro blisters, further supported by the concentric rings. It was believed these rings are cathodic blister sites, which only occurred when a large excess of the electrolyte was used, such that the entire scribe was covered with solution. Comparatively, the SKP and scribe fluorescent studies (depicted in Figure 5.17) were only exposed to 2 μL of 5% NaCl. Blisters were not observed in these films which were attributed to the deficient volume of electrolyte used. This low volume did not contain sufficient osmotic pressure to induce blister formation. However, similarly to these blisters, it was expected that FSCN would be more responsive in these regions due to the increased pH from the reduction reaction that occurs at the cathode. Consistently, FSCN exhibited detectable increases in fluorescence intensity around regions of cathodic delamination.

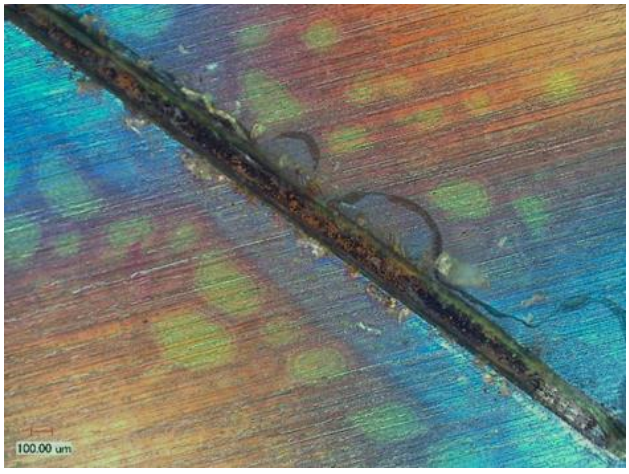

Figure 5.16 Overlay of confocal laser scanning microscope and polarized light microscope images.

Figure 5.17 compares representative scans of the different residual solvent levels of PKHA films that contained FSCN. In these data, scribes are located at 0 on the x-axis while the delamination zone radiated outward from that location. With increasing time, there was an increase in intensity and a broadening of the emission peak, which indicated that the local pH had increased. In Figure 5.17A, a unimodal peak was present until 12 hours of exposure. Upon increased exposure to 24 hours, a bimodal peak formed and each side of the peak widened as the time of exposure progressed. The change in modality was most likely caused by the resolution of the measurement with respect to the defect size. The beam on the scanning fluorimeter was 1 mm in diameter, whereas the defect was only 200 μm wide. Because of this excess measurement, it appeared that the fluorescent intensity increase was at the scribe, rather than surrounding the scribe; however, the spatial resolution is only 1 mm in the x and y plane. Therefore, at late times, a prominent scribe region can be realized with the bimodality of the fluorescent signal because the delamination had reached sufficiently far distances from the scribe such that the scribe was clearly defined.

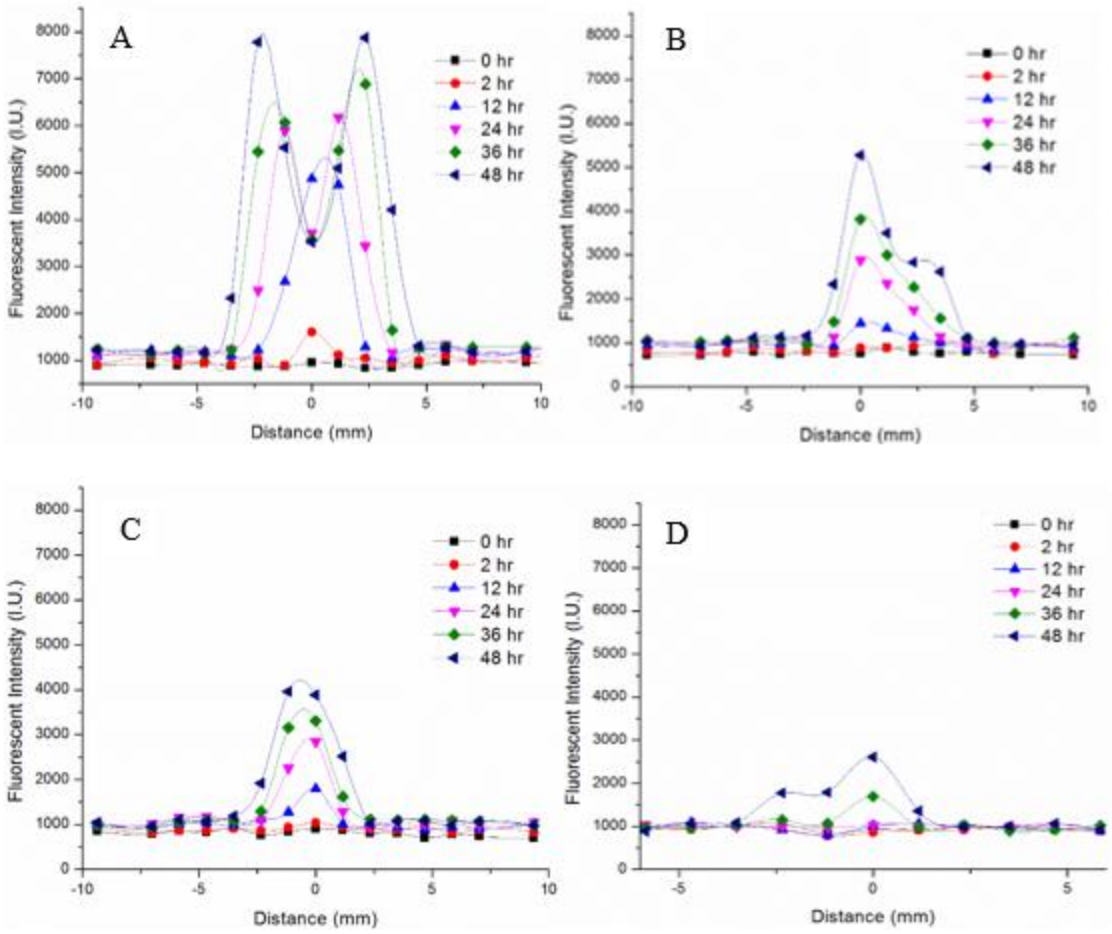

Figure 5.17 Fluorescence measurements of scribed PKHA delamination studies.

PKHA with A) 14 wt% residual solvent; B) 9 wt% residual solvent; C) 6 wt% residual solvent; D) 1.5 wt% residual solvent

As the residual solvent content of the polymeric film was decreased, there was a decrease in the cathodic delamination rate for PKHA films. Most notably was the drop from 8000 intensity units for PKHA with 14 wt% residual solvent to 3000 intensity units for PKHA that contained 1.5 wt% residual solvent. By measuring the point at which fluorescence intensity deviated from the baseline, it was possible to measure the distance from the scribe. The distances are plotted in Figure 5.18 with respect to time$^{1/2}$.

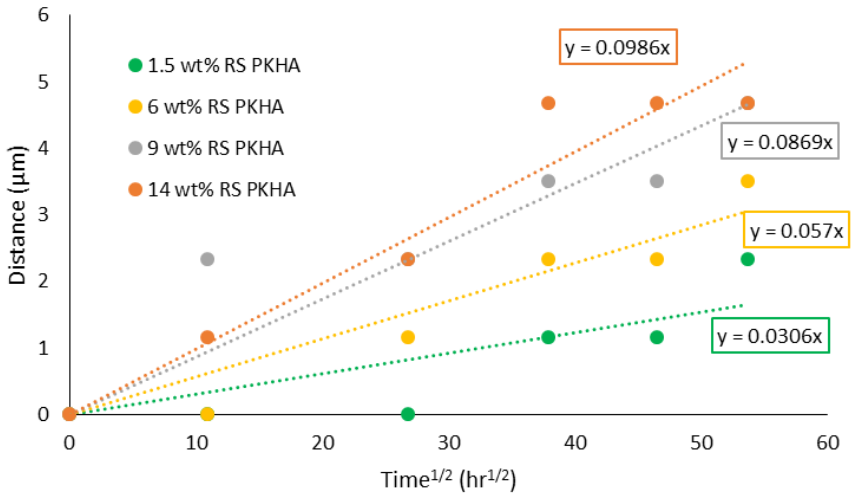

Figure 5.18 Delamination distance as a function of time$^{1/2}$ for PKHA as various residual solvent levels as determined *via* fluorescent scanning spectroscopy.

The slope of each SKP and fluorescence measurement were compared to determine the correlation between the two individual techniques. The slopes obtained from SKP and fluorescence measurements are compared in Figure 5.19. From these data, it was observed that results from both methods were similar.

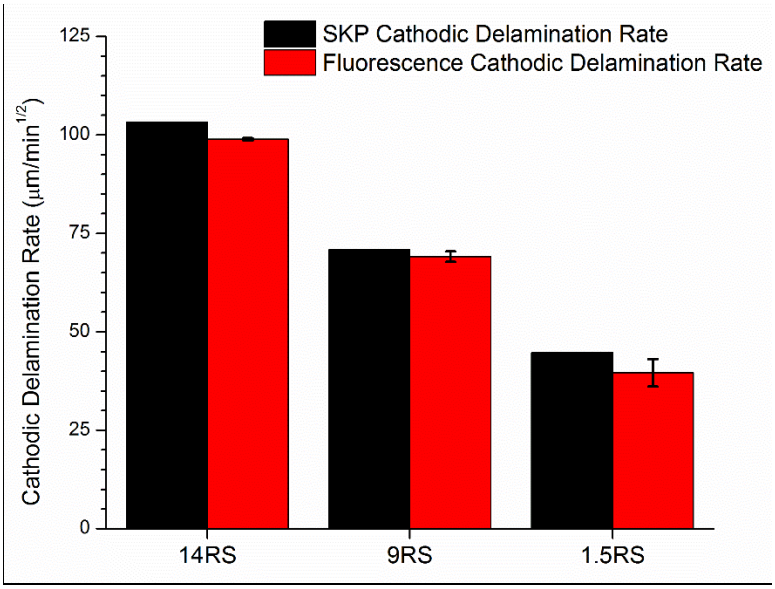

Figure 5.19 Comparison of SKP and fluorescence-derived delamination rates.

The error bars are one standard deviation from the mean of the triplicate.

Primarily, it was determined that the delamination rate decreased with decreasing residual solvent within the films. Furthermore, the percent difference in measured delamination rate between each technique was ~9%, or within the expected noise contributions from each technique. These data support the concept of utilizing FSCN as a probe for direct interrogation of clear films from metallic substrates, provided that the substrate's corrosion mechanism is similar to iron.

5.2.4 Effect of inhibitors

Once FSCN was confirmed to correlate with SKP measurements, a series of films were cast and placed vertically in a solution so that the scribe was immersed 1mm beyond the bare metal. These solutions were prepared and contained a variety of salts and inhibitors to monitor the delamination progress. Figures 5.20 and 5.21 report the time-based fluorescent measurements of different salt and inhibitor immersion conditions of PKHH films cast from EEP at 30 wt% resin solution onto steel substrates. The resultant films contained 14 wt% residual solvent at the time of measurement. To determine the effect of salt concentration, 3.5 wt% and 5 wt% solutions of NaCl were utilized. Furthermore, to determine if fluorescence could be used to assess corrosion inhibitor performance, solutions that contained an industry standard, $SrCrO_4$, were prepared.

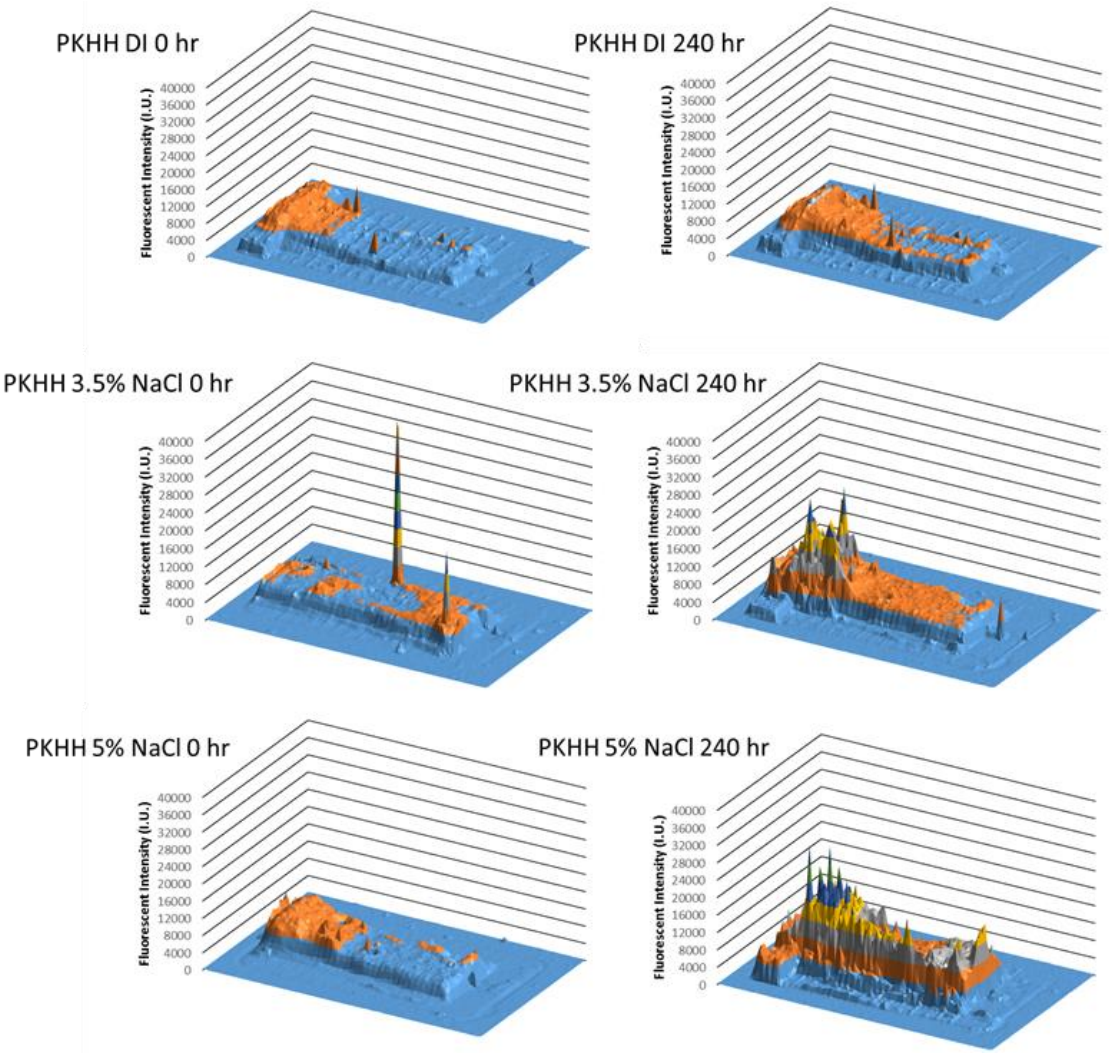

Figure 5.20 Fluorescent response of PKHH cast from EEP and exposed to various salt solutions

Films contained 14 st% solvent. Samples were measured at 0 and 240 hours of exposure.

As evidenced from the graphs in Figure 5.20, increasing the salt concentration directly increased the propagation of cathodic delamination measured after 240 hours of exposure. PKHH exposed to DI water (Figure 5.20 top)_exhibited minor delamination near the scribe (left side of graphs). Upon increased salt content to 3.5 wt%, a significant increase in fluorescent intensity was observed, where approximately 9 cm^2 of the sample exhibited cathodic delamination. When the salt content was increased to 5 wt% the entire

sample exhibited cathodic delamination, which represented an area of ~27 cm^2. Figure 5.20 reports the influence of adding $SrCrO_4$ to the immersion solution to inhibit cathodic delamination.

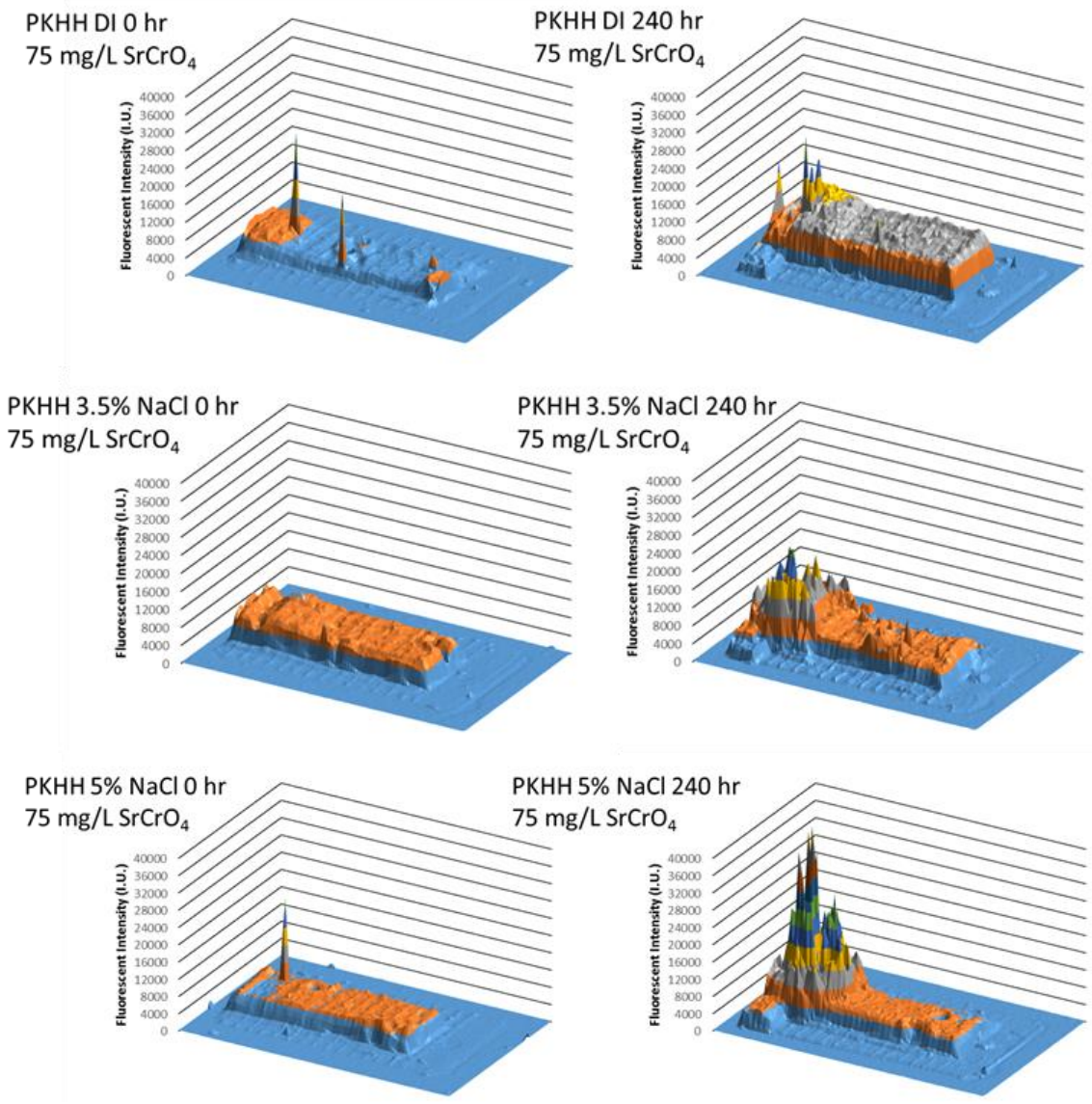

Figure 5.21 Fluorescent response of PKHH cast from EEP and exposed to various salt solutions containing $SrCrO_4$ as an inhibitor.

Films contained 14 st% solvent. Samples were measured at 0 and 240 hours of exposure.

From these data in Figure 5.20, two primary results are noteworthy. The first is that the DI exposed film with the chromate addition exhibited a higher fluorescent

intensity than the equivalent film exposed to just DI water. This was likely caused by inhibitor migration at the substrate-coating interface; however, because of the lack of salt, there was little corrosion detected. Therefore, it was postulated that the hydration of the chromate ions artificially resulted in an increased fluorescence, similar to the water response discussed in Chapter II. Secondly, a reduction in the cathodic delamination was observed for both 3.5 and 5 wt% NaCl solutions whereby the extent of the fluorescent intensity increased was reduced in area and contained to the scribe. However, the intensity of the cathodically delaminated region near scribe was higher than the equivalent samples exposed to just the NaCl solutions. It was believed that the increased intensity was a direct result of concentration of OH^- species being formed. As the cathodic delamination was retarded, the concentration was not spread over as large of an area, rather it was contained near the scribe. Therefore, an increased intensity would be expected. Upon measuring the area fluoresced differentials between the chromate and non-chromate solutions, ~60% reduction in cathodic delamination was observed, which correlated well results found in literature.[196-197]

From these data, it was apparent that fluorescence measurements could also be utilized to monitor corrosion inhibitor efficiency. In order to determine if the understanding gained from fluorescence measurements matched with what occurred during the corrosion process, SEM elemental analysis was performed on the films from Figures 5.19 and 5.20.

5.2.5 SEM elemental analysis

In order to confirm the formation of ionic species that would increase fluorescence intensity, SEM-EDS was performed at the scribe, at the edge of the

delamination front, and away from the delamination front where the intact coating remained. As reported in Figure 5.21, there was little measurable Na at the scribe; however, it was found at the delamination front. As cathodic delamination is a cation diffusion limited process, the finding of Na at the front was congruent with current literature. Measuring sodium away from the scribe indicated that sodium migrated under the film at the coating-substrate interface to provide charge neutralization at the cathodic front.

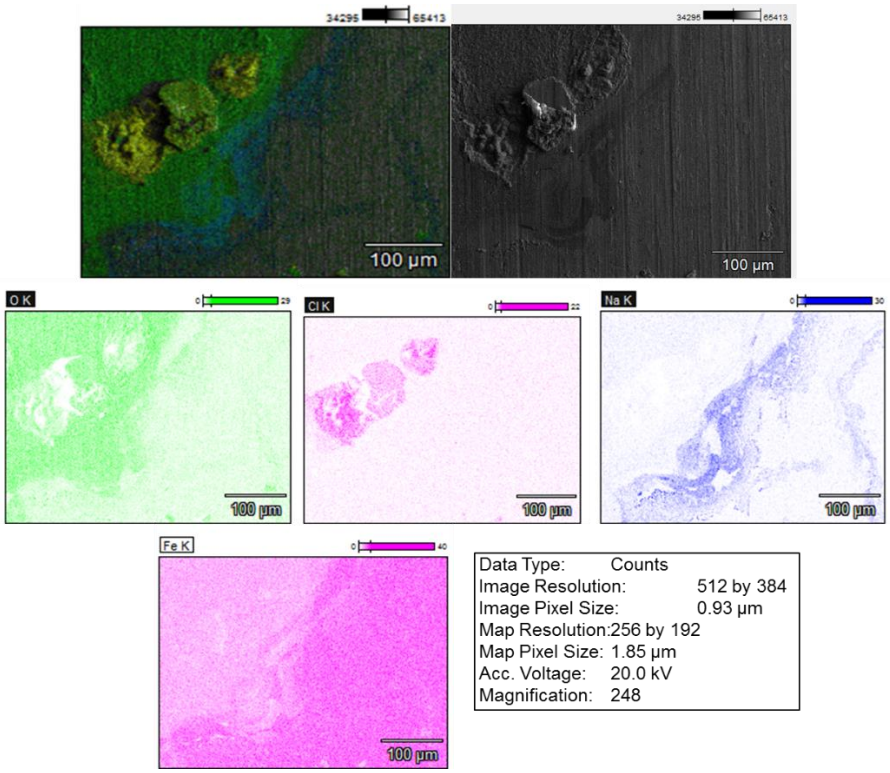

Figure 5.22 SEM-EDS analysis of an ASTM B117 exposed panel.

There existed a distinct separation of sodium and chlorine in each of the samples measured. When measuring the films that were exposed to 5% NaCl with chromate (Figure 5.22), chromium was found deposited in the scribed region, which explained the

lack of fluorescent response away from the panel. This deposition at the scribe inhibited the anodic reaction from occurring, which in turn caused the cathodic reaction being suppressed.

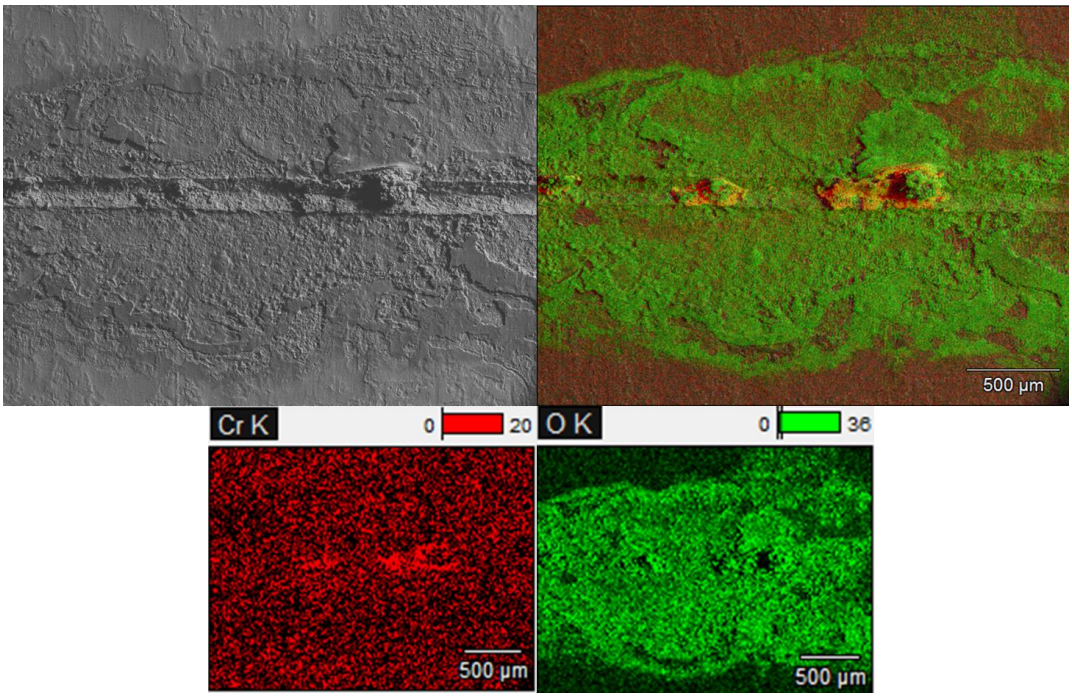

Figure 5.23 Substrate after PKHH coating removal and 240 hrs of 5% NaCl/75 mg/L $SrCrO_4$ exposure.

5.3 Conclusions

This research elucidated FSCN's ability to accurately measure cathodic delamination, which allowed for facile, high throughput analysis. In this work, an excellent correlation was achieved between SKP and fluorescent spectroscopy during cathodic delamination measurements. Comparison of the rates measured from each technique resulted in an average of 9% difference for each residual solvent level. It was also determined that the delamination rate was highly dependent on the amount of residual solvent in the film being measured, which indicated a need for precise sample preparation to ensure the coatings remained consistent. SEM was utilized to confirm the

presence of Na away from the defect, further confirming the diffusion of cations for cathodic delamination. During exposure to strontium chromate during delamination measurements, it was shown that chromate inhibition could also be quantifiably measured with fluorescent spectroscopy. Therefore, faster measurement times and higher throughput could be obtained to speed up inhibitor and polymeric binder screening, reducing the time required to implement new technology.

This work also established the use of multi-probe cocktails to measure different attributes of the corrosion reaction, such as water ingress and pH changes. With further development, these cocktails would provide faster gains in understanding during polymeric binder or inhibitor screening such that new technologies can be realized.

Finally, the complex interplay between binders, solvents, and inhibitors, as well as the residual solvents that remain in the film after curing or drying was shown to all impact corrosion detection rates through fluorescent spectroscopy and SKP. These data suggested a judicious selection of solvents and precise material preparation all impact the cathodic delamination rates. FSCN could also be used for in-field monitoring of cathodic delamination, as SKP is not a viable technique for field measurements. By incorporating FSCN into clear coats used, a simple blacklight flashlight could be used to determine the extent of corrosion, especially in confined areas with complex geometry.

CHAPTER VI – SUMMARY, CONCLUSIONS, AND FUTURE WORK

6.1 Summary and Conclusions

The purpose of this research was to understand further structure-property relationships that govern organic coating's resistance or propensity for corrosion based on measurable changes of the film. It was hypothesized that by changing residual solvents and molecular weights would directly impact the morphology and corrosion performance of thermoplastic coatings. Altering the induction period through a variety of different criterion was utilized throughout each chapter. Scribe width, salt content and composition, residual solvent content and composition, polymer modulus, adhesion, and polymer molecular weight were all quantifiably determined to change the induction period prior to visual macroscopic corrosion. This research suggests that the aforementioned criteria cause irreversible changes to occur in all thermoplastic and thermoset systems utilized by coatings formulators across the world, yet is neglected when coatings are designed.

Chapter III provided a much-needed basis for understanding how accelerated corrosion exposure analysis techniques alter the mechanistic paths and the rates of detectable corrosion processes. Because the visual analysis is so widely used, it was essential to ensure quantifiable and reproducible data, both intra- and inter-laboratory measurements. It was found that only the amount of exposed metal, or the scribe width, impacted the corrosion rate relative to cathodic delamination events. In learning this, new standard operating procedures can be introduced and afford a greater wealth of knowledge of corrosion events that occur in accelerated testing. Equation 9 was

developed to afford direct measurements of any past, present, or future data collected that use any scribe profile, as long as the original scribe area was known.

$$\Delta\, Area\ Percentage\ (\Delta\bar{A}) = \bar{A}_t - \bar{A}_0 \qquad \text{Equation 9}$$

Chapter IV evaluated the effect of molecular weight-induced T_g after conditionally specific drying and annealing profiles and corresponding modulus, and residual solvent concentration on morphological features within a model thermoplastic coating. While coating morphology remains challenging to measure quantifiably, this research was able to determine the critical solvent and modulus importance on microvoid formation within model thermoplastic corrosion control coatings. Internal stress measurements indicated that approximately a 1 MPa difference between the 0 wt% residual solvent films of different molecular weights existed. Furthermore, by utilizing SEM, it was possible to visualize the distribution of these voids, even when they occurred in pigmented, and thus unobservable to the unaided eye. It was found that when large amounts of water-miscible solvent were present, voids formed and grew within the bulk of the polymer such that the film became opaque. Optical transparency measurements were able to confirm a 100% reduction in light transmission at all wavelengths in the visible regime when large amounts of residual solvent were present prior to exposure; however when lower amounts of residual solvent were used and the modulus of the film was greater, then reduction of light transmission was limited to ~12.5% within 24 hours. By using DMA to characterize the tensile storage modulus of the films, a relationship between the dry film modulus and the ability to whiten due to voids was found. Films that contained a sufficient amount of solvent, or were elevated to the appropriate temperature, such that their storage modulus was below 1,450 MPa whitened predictably

and controllably. This research established an explicit dependency on the water-miscible domains that must be present for a film to undergo whitening, as these polymers were surfactant free and water-insoluble by design. Therefore, any voids that formed would be due to the presence of the water-miscible solvents used in the coating application. By decreasing the water-miscible content, up to a 4x increase in the storage modulus was observed to counteract the formation of voids. These voids could be tailored to increase or decrease the rate of inhibitor release or afford pathways such that film behaves like a membrane if desired. Comparison of a fully formulated pigmented film revealed similar trends, in that voids appeared given sufficient time of immersion in DI water at the right temperature. Furthermore, exposure of these films that predictably whitened in DI water exhibited little to no whitening upon exposure to salt containing solutions, which indicated that the salt presence competed against the polymer interactions with water. Voids were found with a diameter of ~2 μm for high residual solvent and decreased as less solvent was present and correspondingly, the film modulus increased. Voids within a commercial coating were found to be ~1 order of magnitude lower in diameter than the voids found in the high residual solvent model thermoplastic films, which was attributed to the increased bulk modulus caused by the incorporation of pigments and fillers, as well as the lack of highly water-miscible solvents. The formation of voids is expected to be applicable to all polymeric materials and are suspected go undetected in almost all pigmented coatings and yet are possible with all ambient cured materials that have solvent or water present during physical or chemical vitrification processes.

In Chapter V, it was shown that fluorescent spectroscopy correlated quantifiably and statistically with SKP during cathodic delamination measurements. Rates between

the two techniques only differed by an average of 9%, which falls within the standard deviation expected for each technique. By reducing the residual solvent content to $1/10^{th}$ of the ambient dried films a 230% reduction in the cathodic delamination was observed. Fluorescent grids printed at the surface of the polymer allowed for easy calculation of the area that underwent cathodic delamination over time and provided a more quantitative analysis than visual methods alone. Inhibitor effect was also monitored with fluorescence, as the corrosion was limited to the scribed region when $SrCrO_4$ was present and resultant inhibitory effects were measured at ~60% reduction in cathodic delamination, which was comparable to literature values. Fluorescence allows for a more facile, higher throughput methodology to study inhibitor effects during corrosion testing. The use of a model thermoplastic poly(hydroxyether), combined with the ease of fluorescent analysis would allow for faster quantitative results of new corrosion inhibitor technology. Further investigations into direct pH measurements could elucidate extent of iron dissolution that must occur before fluorescent intensity increase is observed.

6.2 Future work

While the basis of scribe methodology was established, a dependency on coating chemistry would provide useful in determining the universality of this method. Representative coatings, such as powder coatings, direct-to-metal latexes, and thermoplastic comparisons could be measured such that the coating chemistry could be directly related to the scribe width. Because the dependency on scribe was confirmed by detailed and thorough analysis, the tool types could be down-selected for faster data collection and easier comparison between laboratories and methods worldwide.

Further investigation into the effects of water whitening needs to be conducted. Permeability studies before and after whitening, as well as after a re-drying step above the T_g of the polymer would provide knowledge regarding the interaction of water with these voids. Salt content and whitening relationships could be established, such that a minimum threshold of salt could be found that still causes voids to form. Removal of the water miscible components and incorporation of non-soluble species could further refine the findings from this study. ATR-FTIR water sorption kinetics need to be analyzed to determine the ratios of hydrogen bonding of water within the film, based on time and residual solvent. Lastly, inhibitor release profiles of laden films could be measured such that release kinetics could be determined.

Fluorescent spectroscopy was successfully used to correlate with electrochemical methods in determining cathodic delamination rates. Addition of an acidic sensing probe would reveal greater knowledge regarding the pH gradient that forms at the polymer-substrate interface. Detection of filiform corrosion would also be possible with a different probe and be correlated to the rate determined *via* SKP. A library of inhibitors could be investigated with FSCN laden films and should be compared against the same films under SKP measurement conditions. Comparison of inhibitors *via* fluorescence would provide the grounds for rapid quantification of inhibitor efficiency relative to chromates such that a suitable replacement may be found faster. To better understand the impact of chemistry, further measurements should be made with NeoCryl and other clear thermoplastic resins. In order to provide a complete understanding of molecular weight impacts, PKHH films should also be measured.

REFERENCES

1. Fontana, M. G., *Corrosion engineering*. Tata McGraw-Hill Education: 2005.
2. Shaw, B. A.; Kelly, R. G., What is corrosion? *Interface-Electrochemical Society* **2006,** *15* (1), 24-27.
3. Gerhardus Koch, J. V., Neil Thompson, Oliver Moghissi, Melissa Gould, Joe Payer *International Measures of Prevention, Application, and Economics of Corrosion Technologies Study*; NACE International: 2016.
4. Sangaj, N. S.; Malshe, V., Permeability of polymers in protective organic coatings. *Prog. Org. Coat.* **2004,** *50* (1), 28-39.
5. Sørensen, P. A.; Kiil, S.; Dam-Johansen, K.; Weinell, C. E., Anticorrosive coatings: a review. *J Coat Technol Res* **2009,** *6* (2), 135-176.
6. Thomas, N. L., The barrier properties of paint coatings. **1991**.
7. Forsgren, A.; Knudsen, O. Ø., *Corrosion control through organic coatings*. CRC Press: 2017.
8. Weiss, K. D., Paint and coatings: a mature industry in transition. *Progress in Polymer Science* **1997,** *22* (2), 203-245.
9. Bierwagen, G. P., The science of durability of organic coatings: a foreword. *Prog. Org. Coat.* **1987,** *15* (3), 179-195.
10. Martin, J. W., *Methodologies for predicting the service lives of coating systems*. DIANE Publishing: 1994; Vol. 172.
11. Hanna, J. Understanding Corrosion Protection and Failure Through Model Polymers in Thin Films. The University of Southern Missippi, 2012.
12. Konecki, C. Solvent Effects of Model Polymeric Corrosion Control Coatings on Water Transport and Corrosion Rate. The University of Southern Mississippi, 2017.
13. Foster, S. F.; Hoff, E. A.; Curtzwiler, G. W.; Williams, E. B.; Davis, K. B.; Patton, D. L.; Rawlins, J. W., Chemorheology investigation of a glassy epoxy thermoset on tensile plastic flow and fracture morphology. *Journal of Polymer Science Part B: Polymer Physics* **2015,** *53* (19), 1333-1344.
14. Dušková-smrčková, M.; Dušek, K., Processes and states during polymer film formation by simultaneous crosslinking and solvent evaporation. *Journal of Materials Science* **2002,** *37* (22), 4733-4741.
15. Richardson, H.; Sferrazza, M.; Keddie, J. L., Influence of the glass transition on solvent loss from spin-cast glassy polymer thin films. *The European Physical Journal E* **2003,** *12* (1), 87-91.
16. Palmese, G. R.; Gillham, J. K., Time–temperature–transformation (TTT) cure diagrams: Relationship between Tg and the temperature and time of cure for a polyamic acid/polyimide system. *Journal of Applied Polymer Science* **1987,** *34* (5), 1925-1939.
17. Benjamin, S.; Carr, C.; Walbridge, D. J., Self-stratifying coatings for metallic substrates. *Prog. Org. Coat.* **1996,** *28* (3), 197-207.
18. Beaugendre, A.; Degoutin, S.; Bellayer, S.; Pierlot, C.; Duquesne, S.; Casetta, M.; Jimenez, M., Self-stratifying epoxy/silicone coatings. *Prog. Org. Coat.* **2017,** *103*, 101-110.
19. Vink, P.; Bots, T., Formulation parameters influencing self-stratification of coatings. *Prog. Org. Coat.* **1996,** *28* (3), 173-181.

20. Verkholantsev, V., Heterophase and self-stratifying polymer coatings. *Prog. Org. Coat.* **1995,** *26* (1), 31-52.
21. Chen, L. Self-Stratifying Coatings. University of Akron, 2013.
22. Bierwagen, G.; Fishman, R.; Storsved, T.; Johnson, J., Recent studies of particle packing in organic coatings. *Prog. Org. Coat.* **1999,** *35* (1), 1-9.
23. Perera, D. Y., Effect of pigmentation on organic coating characteristics. *Prog. Org. Coat.* **2004,** *50* (4), 247-262.
24. Erich, S. J. F.; Huinink, H. P.; Adan, O. C. G.; Laven, J.; Esteves, A. C., The influence of the pigment volume concentration on the curing of alkyd coatings: A 1D MRI depth profiling study. *Prog. Org. Coat.* **2008,** *63* (4), 399-404.
25. Van der Wel, G.; Adan, O., Moisture in organic coatings—a review. *Prog. Org. Coat.* **1999,** *37* (1-2), 1-14.
26. Morsch, S.; Kefallinou, Z.; Liu, Y.; Lyon, S. B.; Gibbon, S. R., Controlling the nanostructure of epoxy resins: Reaction selectivity and stoichiometry. *Polymer* **2018,** *143*, 10-18.
27. Foster, S. Mechanochemical Investigation of a Glassy Epoxy-Amine Thermoset Subjected to Fatigue. The University of Southern Mississippi, 2015.
28. Sahagun, C. M.; Morgan, S. E., Thermal Control of Nanostructure and Molecular Network Development in Epoxy-Amine Thermosets. *ACS applied materials & interfaces* **2012,** *4* (2), 564-572.
29. Fedors, R. F., Osmotic effects in water absorption by polymers. *Polymer* **1980,** *21* (2), 207-212.
30. Jiang, B.; Tsavalas, J. G.; Sundberg, D. C., Water whitening of polymer films: Mechanistic studies and comparisons between water and solvent borne films. *Prog. Org. Coat.* **2017,** *105*, 56-66.
31. Liu, Y.; Gajewicz, A. M.; Rodin, V.; Soer, W. J.; Scheerder, J.; Satgurunathan, G.; McDonald, P. J.; Keddie, J. L., Explanations for water whitening in secondary dispersion and emulsion polymer films. *Journal of Polymer Science Part B: Polymer Physics* **2016,** *54* (16), 1658-1674.
32. Aguirreurreta, Z.; Dimmer, J.-A.; Willerich, I.; de la Cal, J. C.; Leiza, J. R., Water Whitening Reduction in Waterborne Pressure-Sensitive Adhesives Produced with Polymerizable Surfactants. *Macromolecular Materials and Engineering* **2015,** *300* (9), 925-936.
33. Johnson, G. E.; Bair, H. E.; Matsuoka, S.; Anderson, E. W.; Scott, J. E., Water Sorption and Its Effect on a Polymer's Dielectric Behavior. In *Water in Polymers*, AMERICAN CHEMICAL SOCIETY: 1980; Vol. 127, pp 451-468.
34. Bair, H. E.; Johnson, G. E.; Merriweather, R., Water sorption of polycarbonate and its effect on the polymer's dielectric behavior. *Journal of Applied Physics* **1978,** *49* (10), 4976-4984.
35. Briggs, G. J.; Edwards, D. C.; Storey, E. B., Water Absorption of Elastomers. *Rubber Chem. Technol.* **1963,** *36* (3), 621-641.
36. McCabe, J. F.; Rusby, S., Water absorption, dimensional change and radial pressure in resin matrix dental restorative materials. *Biomaterials* **2004,** *25* (18), 4001-4007.

37. Schirrer, R.; Thepin, P.; Torres, G., Water absorption, swelling, rupture and salt release in salt-silicone rubber compounds. *Journal of materials science* **1992,** *27* (13), 3424-3434.
38. Greenidge, K., Ascent of sap. *Annual Review of Plant Physiology* **1957,** *8* (1), 237-256.
39. Milburn, J. A., Sap ascent in vascular plants: challengers to the cohesion theory ignore the significance of immature xylem and the recycling of Münch water. *Ann. Bot.* **1996,** *78* (4), 399-407.
40. Steudle, E., The cohesion-tension mechanism and the acquisition of water by plant roots. *Annu. Rev. Plant Biol.* **2001,** *52* (1), 847-875.
41. Angeles, G.; Bond, B.; Boyer, J. S.; Brodribb, T.; Brooks, J. R.; Burns, M. J.; Cavender-Bares, J.; Clearwater, M.; Cochard, H.; Comstock, J., The cohesion-tension theory. *New Phytol.* **2004,** *163* (3), 451-452.
42. Sedgewick, S.; Trevena, D., An estimate of the ultimate tensile strength of water. *Journal of Physics D: Applied Physics* **1976,** *9* (18), L203.
43. Crum, L. A., Tensile strength of water. *Nature* **1979,** *278*, 148.
44. Steudle, E., Trees under tension. *Nature* **1995,** *378*, 663.
45. Dixon, H. H., *The transpiration stream*. University of London press, ltd.: 1924.
46. Tyree, M. T., The cohesion-tension theory of sap ascent: current controversies. *J. Exp. Bot.* **1997,** *48* (10), 1753-1765.
47. Wei, C.; Tyree, M. T.; Steudle, E., Direct measurement of xylem pressure in leaves of intact maize plants. A test of the cohesion-tension theory taking hydraulic architecture into consideration. *Plant Physiol.* **1999,** *121* (4), 1191-1205.
48. JIKEI, M.; YAMAYA, T.; URAMOTO, S.; MATSUMOTO, K., Conductivity enhancement of PEDOT/PSS films by solvent vapor treatment. *International Journal of the Society of Materials Engineering for Resources* **2014,** *20* (2), 158-162.
49. Solvent induced modifications to fiber nanostructure and morphology for 12HSA molecular gels. **2014**.
50. Ruderer, M. A.; Guo, S.; Meier, R.; Chiang, H.-Y.; Körstgens, V.; Wiedersich, J.; Perlich, J.; Roth, S. V.; Müller-Buschbaum, P., Solvent-Induced Morphology in Polymer-Based Systems for Organic Photovoltaics. *Advanced Functional Materials* **2011,** *21* (17), 3382-3391.
51. Jung, Y. S.; Ross, C. A., Solvent-Vapor-Induced Tunability of Self-Assembled Block Copolymer Patterns. *Advanced Materials* **2009,** *21* (24), 2540-2545.
52. Jeong, H. S.; Noh, J. H.; Hwang, C. G.; Kim, S. H.; Lee, S. Y., Effect of Solvent–Nonsolvent Miscibility on Morphology and Electrochemical Performance of SiO2/PVdF-HFP-Based Composite Separator Membranes for Safer Lithium-Ion Batteries. *Macromolecular Chemistry and Physics* **2010,** *211* (4), 420-425.
53. Wang, D.-M.; Lai, J.-Y., Recent advances in preparation and morphology control of polymeric membranes formed by nonsolvent induced phase separation. *Current Opinion in Chemical Engineering* **2013,** *2* (2), 229-237.
54. Jung, J. T.; Kim, J. F.; Wang, H. H.; di Nicolo, E.; Drioli, E.; Lee, Y. M., Understanding the non-solvent induced phase separation (NIPS) effect during the fabrication of microporous PVDF membranes via thermally induced phase separation (TIPS). *J. Membr. Sci.* **2016,** *514*, 250-263.

55. Perera, D. Y., On adhesion and stress in organic coatings. *Prog. Org. Coat.* **1996,** *28* (1), 21-23.
56. Perera, D. Y.; Eynde, D. V., Moisture and temperature induced stresses (hygrothermal stresses) in organic coatings. *Journal of coatings technology* **1987,** *59* (748), 55-63.
57. Kamarchik, P., Crosslink density and the development of internal stress in organic coatings. *Macromolecular Symposia* **2001,** *175* (1), 411-420.
58. Croll, S., *Internal stress in a solvent-cast thermoplastic coating*. Division of Building Research, National Research Council: 1978.
59. Croll, S. G., The origin of residual internal stress in solvent-cast thermoplastic coatings. *Journal of Applied Polymer Science* **1979,** *23* (3), 847-858.
60. Sato, K., The internal stress of coating films. *Prog. Org. Coat.* **1980,** *8* (2), 143-160.
61. Negele, O.; Funke, W., Internal stress and wet adhesion of organic coatings. *Prog. Org. Coat.* **1996,** *28* (4), 285-289.
62. Tsavalas, J. G.; Sundberg, D. C., Hydroplasticization of polymers: model predictions and application to emulsion polymers. *Langmuir* **2010,** *26* (10), 6960-6966.
63. Jiang, B.; Tsavalas, J.; Sundberg, D., Measuring the glass transition of latex-based polymers in the hydroplasticized state via differential scanning calorimetry. *Langmuir* **2010,** *26* (12), 9408-9415.
64. Lim, L.-T.; Britt, I. J.; Tung, M. A., Sorption and transport of water vapor in nylon 6,6 film. *Journal of Applied Polymer Science* **1999,** *71* (2), 197-206.
65. de Nève, B.; Shanahan, M. E. R., Effects of humidity on an epoxy adhesive. *International Journal of Adhesion and Adhesives* **1992,** *12* (3), 191-196.
66. De Neve, B.; Shanahan, M. E. R., Physical and Chemical Effects in An Epoxy Resin Exposed to Water Vapour. *The Journal of Adhesion* **1995,** *49* (3-4), 165-176.
67. Standard Practice for Operating Salt Spray (Fog) Apparatus. ASTM International: 2016.
68. Defense, D. o., Primer, Epoxy Coating, Corrosion Inhibiting Lead and Chromate Free. Department of Defense: 2010; Vol. MIL-DTL-53022D.
69. Standard Test Method for Evaluation of Painted or Coated Specimens Subjected to Corrosive Environments. ASTM International: 2016.
70. International, A., Standard Practice for Evaluating Degree of Rusting on Painted Steel Surfaces. ASTM: 2012; Vol. D610-08.
71. Standarization, I. O. f., Paints and Varnishes-Evaluation of Degradation of Coatings. In *Designation of quantity and size of defects, and of intensity of uniform changes in appearance*, ISO: 2016; Vol. 4628.
72. Selvaraj, R.; Selvaraj, M.; Iyer, S. V. K., Studies on the evaluation of the performance of organic coatings used for the prevention of corrosion of steel rebars in concrete structures. *Prog. Org. Coat.* **2009,** *64* (4), 454-459.
73. Zapponi, M.; Pérez, T.; Ramos, C.; Saragovi, C., Prohesion and outdoors tests on corrosion products developed over painted galvanized steel sheets with and without Cr(VI) species. *Corros. Sci.* **2005,** *47* (4), 923-936.
74. Kinlen, P. J.; Silverman, D. C.; Jeffreys, C. R., Corrosion protection using polyaniline coating formulations. *Synth. Met.* **1997,** *85* (1), 1327-1332.

75. Mehta, N. K.; Bogere, M. N., Environmental studies of smart/self-healing coating system for steel. *Prog. Org. Coat.* **2009,** *64* (4), 419-428.
76. Loo, M. V.; Laiderman, D. D.; Bruhn, R. R., Filiform Corrosion. *CORROSION* **1953,** *9* (8), 277-283.
77. Fastrup, B.; Saarnak, A., AC impedance of painted and scribed steel panels under atmospheric exposure. *Prog. Org. Coat.* **1988,** *16* (3), 277-290.
78. Lambert, M. R.; Townsend, H. E.; Hart, R. G.; Frydrych, D. J., Accelerated corrosion tests of precoated sheet steels for automobiles. *Industrial & Engineering Chemistry Product Research and Development* **1985,** *24* (3), 378-384.
79. Chico, B.; de la Fuente, D.; Pérez, M. L.; Morcillo, M., Corrosion resistance of steel treated with different silane/paint systems. *J Coat Technol Res* **2012,** *9* (1), 3-13.
80. Feng, Z.; Frankel, G. S.; Matzdorf, C. A., Quantification of Accelerated Corrosion Testing of Coated AA7075-T6. *J. Electrochem. Soc.* **2014,** *161* (1), C42-C49.
81. Nguyen, T.; Martin, F., Modes and Mechanisms of Degradation of Epoxy-Coated Reinforcing Steel in Marine Environment. *Durability of Building Materials Components* **1996,** *7*, 491.
82. Arrabal, R.; Mota, J. M.; Criado, A.; Pardo, A.; Mohedano, M.; Matykina, E., Assessment of duplex coating combining plasma electrolytic oxidation and polymer layer on AZ31 magnesium alloy. *Surf. Coat. Technol.* **2012,** *206* (22), 4692-4703.
83. Galliano, F.; Landolt, D., Evaluation of corrosion protection properties of additives for waterborne epoxy coatings on steel. *Prog. Org. Coat.* **2002,** *44* (3), 217-225.
84. He, J.; Gelling, V. J.; Tallman, D. E.; Bierwagen, G. P., A Scanning Vibrating Electrode Study of Chromated-Epoxy Primer on Steel and Aluminum. *J. Electrochem. Soc.* **2000,** *147* (10), 3661-3666.
85. Yasuda, H.; Reddy, C.; Yu, Q.; Deffeyes, J.; Bierwagen, G.; He, L., Effect of scribing modes on corrosion test results. *Corrosion* **2001,** *57* (1), 29-34.
86. Corporation, G. M., Cyclic Corrosion Laboratory Test. In *Test Procedure Materials*, General Motors Worldwide Engineering Standards: 2006; Vol. GMW 14872.
87. The Effects and Economic Impact of Corrosion. In *Corrosion: Understanding the Basics*, International, A., Ed. 2000.
88. Pourbaix, M., Thermodynamics and corrosion. *Corros. Sci.* **1990,** *30* (10), 963-988.
89. Van Muylder, J., Thermodynamics of Corrosion. In *Electrochemical Materials Science*, Bockris, J. O. M.; Conway, B.; Yeager, E.; White, R., Eds. Springer US: 1981; Vol. 4, pp 1-96.
90. Cicek, V., Thermodynamics of Corrosion. *Cathodic Protection: Industrial Solutions for Protecting Against Corrosion*, 75-96.
91. Mierisch, A. M.; Yuan, J.; Kelly, R. G.; Taylor, S. R., Probing Coating Degradation on AA2024-T3 Using Local Electrochemical and Chemical Techniques. *J. Electrochem. Soc.* **1999,** *146* (12), 4449-4454.
92. Nazarov, A.; Le Bozec, N.; Thierry, D., Assessment of steel corrosion and deadhesion of epoxy barrier paint by scanning Kelvin probe. *Prog. Org. Coat.* **2018,** *114*, 123-134.

93. Legghe, E.; Aragon, E.; Bélec, L.; Margaillan, A.; Melot, D., Correlation between water diffusion and adhesion loss: Study of an epoxy primer on steel. *Prog. Org. Coat.* **2009,** *66* (3), 276-280.
94. Piens, M.; De Deurwaerder, H., Effect of coating stress on adherence and on corrosion prevention. *Prog. Org. Coat.* **2001,** *43* (1), 18-24.
95. Dickie, R. A., Adhesion of organic coatings and its loss due to corrosion. In *Adhesion Aspects of Polymeric Coatings*, Springer: 1983; pp 319-327.
96. Hammond, J.; Holubka, J.; Dickie, R., The application of X-ray photo-electron spectroscopy to a study of interfacial composition in corrosion-induced paint de-adhesion. *Corros. Sci.* **1981,** *21* (3), 239-253.
97. Nazarov, A.; Olivier, M.-G.; Thierry, D., SKP and FT-IR microscopy study of the paint corrosion de-adhesion from the surface of galvanized steel. *Prog. Org. Coat.* **2012,** *74* (2), 356-364.
98. deVries, J.; Riley, T.; Holubka, J.; Dickie, R., Surface studies of conversion coated steel after corrosion induced paint deadhesion. *Surface and interface analysis* **1985,** *7* (3), 111-116.
99. Leidheiser Jr, H.; Kendig, M. W., The Mechanism of Corrosion of Poly butadiene-Coated Steel in Aerated Sodium Chloride. *Corrosion* **1976,** *32* (2), 69-76.
100. Fürbeth, W.; Stratmann, M., The delamination of polymeric coatings from electrogalvanised steel–a mechanistic approach.: Part 1: delamination from a defect with intact zinc layer. *Corros. Sci.* **2001,** *43* (2), 207-227.
101. Leng, A.; Streckel, H.; Stratmann, M., The delamination of polymeric coatings from steel. Part 2: First stage of delamination, effect of type and concentration of cations on delamination, chemical analysis of the interface. *Corros. Sci.* **1998,** *41* (3), 579-597.
102. Fürbeth, W.; Stratmann, M., Investigation of the delamination of polymer films from galvanized steel with the Scanning Kelvinprobe. *Fresenius J. Anal. Chem.* **1995,** *353* (3-4), 337-341.
103. Pathak, S. S.; Blanton, M. D.; Mendon, S. K.; Rawlins, J. W., Investigation on dual corrosion performance of magnesium-rich primer for aluminum alloys under salt spray test (ASTM B117) and natural exposure. *Corros. Sci.* **2010,** *52* (4), 1453-1463.
104. Simoes, A.; Battocchi, D.; Tallman, D.; Bierwagen, G., Assessment of the corrosion protection of aluminium substrates by a Mg-rich primer: EIS, SVET and SECM study. *Prog. Org. Coat.* **2008,** *63* (3), 260-266.
105. Knudsen, O. Ø.; Steinsmo, U.; Bjordal, M., Zinc-rich primers—Test performance and electrochemical properties. *Prog. Org. Coat.* **2005,** *54* (3), 224-229.
106. Galvanic Corrosion. http://structx.com/Material_Properties_001.html (accessed 9/13/2018).
107. V. Ashworth, C. J. L. B., H. Charlton, J.J. Fairhurst, P.R. Falkner, E. Jackson, S. Monk, S. Sarsfield, T.J.J. Smith, A Short Introduction to Corrosion and Its Control: Corrosion of Metals and Its Prevention. 9.
108. Williams, G.; McMurray, H. N., Chromate Inhibition of Corrosion-Driven Organic Coating Delamination Studied Using a Scanning Kelvin Probe Technique. *J. Electrochem. Soc.* **2001,** *148* (10), B377-B385.

109. Zin, I. M.; Howard, R. L.; Badger, S. J.; Scantlebury, J. D.; Lyon, S. B., The mode of action of chromate inhibitor in epoxy primer on galvanized steel. *Prog. Org. Coat.* **1998,** *33* (3–4), 203-210.
110. Howard, R. L.; Zin, I. M.; Scantlebury, J. D.; Lyon, S. B., Inhibition of cut edge corrosion of coil-coated architectural cladding. *Prog. Org. Coat.* **1999,** *37* (1–2), 83-90.
111. van Soestbergen, M.; Baukh, V.; Erich, S. J. F.; Huinink, H. P.; Adan, O. C. G., Release of cerium dibutylphosphate corrosion inhibitors from highly filled epoxy coating systems. *Prog. Org. Coat.* **2014,** *77* (10), 1562-1568.
112. Qi, X.; J Gelling, V., A Review of Different Sensors Applied to Corrosion Detection and Monitoring. *Recent Patents on Corrosion Science* **2011,** *1* (1), 1-7.
113. Zhou, Q.; Wang, Y., Comparisons of clear coating degradation in NaCl solution and pure water. *Prog. Org. Coat.* **2013,** *76* (11), 1674-1682.
114. Amirudin, A.; Thierry, D., Application of electrochemical impedance spectroscopy to study the degradation of polymer-coated metals. *Prog. Org. Coat.* **1995,** *26* (1), 1-28.
115. Maples, A., Electrochemical Methods to Monitor Corrosion and Coating Failure. North Dakota State University: 2013.
116. Basics of Electrochemical Impedance Spectroscopy. https://www.gamry.com/application-notes/EIS/basics-of-electrochemical-impedance-spectroscopy/.
117. Dariva, C. G.; Galio, A. F., Corrosion Inhibitors–Principles, Mechanisms and Applications. **2014**.
118. Leng, A.; Streckel, H.; Stratmann, M., The delamination of polymeric coatings from steel. Part 1: Calibration of the Kelvinprobe and basic delamination mechanism. *Corros. Sci.* **1998,** *41* (3), 547-578.
119. König, T.; Simon, G. H.; Heinke, L.; Lichtenstein, L.; Heyde, M., Defects in oxide surfaces studied by atomic force and scanning tunneling microscopy. *Beilstein Journal of Nanotechnology* **2011,** *2*, 1-14.
120. Stratmann, M., The investigation of the corrosion properties of metals, covered with adsorbed electrolyte layers—A new experimental technique. *Corros. Sci.* **1987,** *27* (8), 869-872.
121. Stratmann, M.; Streckel, H.; Feser, R., A new technique able to measure directly the delamination of organic polymer films. *Corros. Sci.* **1991,** *32* (4), 467-470.
122. Stratmann, M.; Leng, A.; Fürbeth, W.; Streckel, H.; Gehmecker, H.; Groβe-Brinkhaus, K. H., The scanning Kelvin probe; a new technique for the in situ analysis of the delamination of organic coatings. *Prog. Org. Coat.* **1996,** *27* (1), 261-267.
123. Jr., H. L., Corrosion of Painted Metals—A Review. *CORROSION* **1982,** *38* (7), 374-383.
124. Leidheiser, H.; Wang, W.; Igetoft, L., The mechanism for the cathodic delamination of organic coatings from a metal surface. *Prog. Org. Coat.* **1983,** *11* (1), 19-40.
125. Wapner, K.; Stratmann, M.; Grundmeier, G., In situ infrared spectroscopic and scanning Kelvin probe measurements of water and ion transport at polymer/metal interfaces. *Electrochim. Acta* **2006,** *51* (16), 3303-3315.

126. Wielant, J.; Posner, R.; Hausbrand, R.; Grundmeier, G.; Terryn, H., SKP as a tool to study the physicochemical interaction at buried metal–coating interfaces. *Surface and Interface Analysis* **2010,** *42* (6-7), 1005-1009.
127. Zhang, J.; Frankel, G. S., Corrosion-Sensing Behavior of an Acrylic-Based Coating System. *CORROSION* **1999,** *55* (10), 957-967.
128. Taylor, S.; Moongkhamklang, P., The delineation of local water interaction with epoxy coatings using fluorescence microscopy. *Prog. Org. Coat.* **2005,** *54* (3), 205-210.
129. Alodan, M. A.; Smyrl, W. H., Detection of Localized Corrosion Using Fluorescence Microscopy. *J. Electrochem. Soc.* **1997,** *144* (10), L282-L284.
130. Sibi, M. P.; Zong, Z., Determination of corrosion on aluminum alloy under protective coatings using fluorescent probes. *Prog. Org. Coat.* **2003,** *47* (1), 8-15.
131. Augustyniak, A.; Ming, W., Early detection of aluminum corrosion via “turn-on” fluorescence in smart coatings. *Prog. Org. Coat.* **2011,** *71* (4), 406-412.
132. Augustyniak, A.; Tsavalas, J.; Ming, W., Early detection of steel corrosion via "turn-on" fluorescence in smart epoxy coatings. *ACS applied materials & interfaces* **2009,** *1* (11), 2618-23.
133. Büchler, M.; Kerimo, J.; Guillaume, F.; Smyrl, W., Fluorescence and Near-Field Scanning Optical Microscopy for Investigating Initiation of Localized Corrosion of Al 2024. *J. Electrochem. Soc.* **2000,** *147* (10), 3691-3699.
134. Gharaibeh, B.; Omar, M.; Salazar, A. J.; Saito, K., Fluorescence emission sensing in coatings: Method for defects detection in coated surfaces of structural elements. *Prog. Org. Coat.* **2007,** *58* (4), 282-289.
135. Liu, X.; Spikes, H.; Wong, J. S. S., In situ pH responsive fluorescent probing of localized iron corrosion. *Corros. Sci.* **2014,** *87*, 118-126.
136. Büchler, M.; Watari, T.; Smyrl, W. H., Investigation of the initiation of localized corrosion on aluminum alloys by using fluorescence microscopy. *Corros. Sci.* **2000,** *42* (9), 1661-1668.
137. Li, S.-m.; Zhang, H.-r.; Liu, J.-h., Preparation and performance of fluorescent sensing coating for monitoring corrosion of Al alloy 2024. *Transactions of Nonferrous Metals Society of China* **2006,** *16, Supplement 1* (0), s159-s164.
138. Bryant, D. E.; Greenfield, D., The use of fluorescent probes for the detection of under-film corrosion. *Prog. Org. Coat.* **2006,** *57* (4), 416-420.
139. Pidaparti, R.; Neblett, E.; Miller, S.; Alvarez, J., Monitoring the corrosion process of Al alloys through pH induced fluorescence. *Smart Materials and Structures* **2008,** *17* (1), 015001.
140. Salinasá Mayorga, R. M.-P., Nikolay O., Extraordinary character of the solvent influence on protolytic equilibria: inversion of the fluorescein ionization constants in H 2 O–DMSO mixtures. *J. Chem. Soc., Faraday Trans.* **1992,** *88* (20), 3025-3032.
141. Klonis, N.; Sawyer, W. H., Effect of Solvent–Water Mixtures on the Prototropic Equilibria of Fluorescein and on the Spectral Properties of the Monoanion¶. *Photochemistry and Photobiology* **2000,** *72* (2), 179-185.
142. Batistela, V. R.; da Costa Cedran, J.; de Oliveira, H. P. M.; Scarminio, I. S.; Ueno, L. T.; da Hora Machado, A. E.; Hioka, N., Protolytic fluorescein species evaluated using chemometry and DFT studies. *Dyes and Pigments* **2010,** *86* (1), 15-24.

143. Slyusareva, E. A.; Gerasimova, M. A., pH-Dependence of the Absorption and Fluorescent Properties of Fluorone Dyes in Aqueous Solutions. *Russian Physics Journal* **2014,** *56* (12), 1370-1377.
144. Sjöback, R.; Nygren, J.; Kubista, M., Absorption and fluorescence properties of fluorescein. *Spectrochimica Acta Part A: Molecular and Biomolecular Spectroscopy* **1995,** *51* (6), L7-L21.
145. Klonis, N.; Clayton, A. H. A.; Voss, E. W.; Sawyer, W. H., Spectral Properties of Fluorescein in Solvent-Water Mixtures: Applications as a Probe of Hydrogen Bonding Environments in Biological Systems. *Photochemistry and Photobiology* **1998,** *67* (5), 500-510.
146. Derby, B., Inkjet printing ceramics: from drops to solid. *Journal of the European Ceramic Society* **2011,** *31* (14), 2543-2550.
147. Özkol, E.; Ebert, J.; Telle, R., An experimental analysis of the influence of the ink properties on the drop formation for direct thermal inkjet printing of high solid content aqueous 3Y-TZP suspensions. *Journal of the European Ceramic Society* **2010,** *30* (7), 1669-1678.
148. Stringer, J.; Derby, B., Limits to feature size and resolution in ink jet printing. *Journal of the European Ceramic Society* **2009,** *29* (5), 913-918.
149. Hendriks, C. E.; Smith, P. J.; Perelaer, J.; van den Berg, A. M. J.; Schubert, U. S., "Invisible" Silver Tracks Produced by Combining Hot-Embossing and Inkjet Printing. *Advanced Functional Materials* **2008,** *18* (7), 1031-1038.
150. Perelaer, J.; de Laat, A. W.; Hendriks, C. E.; Schubert, U. S., Inkjet-printed silver tracks: low temperature curing and thermal stability investigation. *Journal of Materials Chemistry* **2008,** *18* (27), 3209-3215.
151. Perelaer, J.; Hendriks, C. E.; de Laat, A. W.; Schubert, U. S., One-step inkjet printing of conductive silver tracks on polymer substrates. *Nanotechnology* **2009,** *20* (16), 165303.
152. van Osch, T. H. J.; Perelaer, J.; de Laat, A. W. M.; Schubert, U. S., Inkjet Printing of Narrow Conductive Tracks on Untreated Polymeric Substrates. *Advanced Materials* **2008,** *20* (2), 343-345.
153. Wits, W. W.; Sridhar, A. In *Inkjet printing of 3D metallic silver complex microstructures*, International Conference on Competitive Manufacturing, COMA 2010, 2010; p 6.
154. Marin, V.; Holder, E.; Wienk, M. M.; Tekin, E.; Kozodaev, D.; Schubert, U. S., Ink-Jet Printing of Electron Donor/Acceptor Blends: Towards Bulk Heterojunction Solar Cells. *Macromolecular Rapid Communications* **2005,** *26* (4), 319-324.
155. Perelaer, J., Inkjet printing of functional materials: From nanoparticles to microelectronic devices. Dutch Polymer Institute: p 24.
156. Teichler, A.; Shu, Z.; Wild, A.; Bader, C.; Nowotny, J.; Kirchner, G.; Harkema, S.; Perelaer, J.; Schubert, U. S., Inkjet printing of chemically tailored light-emitting polymers. *European Polymer Journal* **2013,** *49* (8), 2186-2195.
157. Tekin, E.; Holder, E.; Marin, V.; de Gans, B.-J.; Schubert, U. S., Ink-Jet Printing of Luminescent Ruthenium- and Iridium-Containing Polymers for Applications in Light-Emitting Devices. *Macromolecular Rapid Communications* **2005,** *26* (4), 293-297.

158. Yoshioka, Y.; Jabbour, G. E., Desktop inkjet printer as a tool to print conducting polymers. *Synth. Met.* **2006,** *156* (11–13), 779-783.
159. Mannerbro, R.; Ranlöf, M.; Robinson, N.; Forchheimer, R., Inkjet printed electrochemical organic electronics. *Synth. Met.* **2008,** *158* (13), 556-560.
160. Park, B. K.; Kim, D.; Jeong, S.; Moon, J.; Kim, J. S., Direct writing of copper conductive patterns by ink-jet printing. *Thin Solid Films* **2007,** *515* (19), 7706-7711.
161. Cooley, P.; Wallace, D.; Antohe, B., Applicatons of ink-jet printing technology to BioMEMS and microfluidic systems. *Journal of the Association for Laboratory Automation* **2002,** *7* (5), 33-39.
162. Li, E. Q.; Tan, E. K.; Thoroddsen, S. T., Piezoelectric Drop-on-Demand Inkjet Printing of Rat Fibroblast Cells: Survivability Study and Pattern Printing. *arXiv preprint arXiv:1310.0656* **2013**.
163. Li, J. S.; Ueda, E.; Nallapaneni, A.; Li, L. X.; Levkin, P. A., Printable Superhydrophilic–Superhydrophobic Micropatterns Based on Supported Lipid Layers. *Langmuir* **2012,** *28* (22), 8286-8291.
164. Crowley, K.; Morrin, A.; Hernandez, A.; O'Malley, E.; Whitten, P. G.; Wallace, G. G.; Smyth, M. R.; Killard, A. J., Fabrication of an ammonia gas sensor using inkjet-printed polyaniline nanoparticles. *Talanta* **2008,** *77* (2), 710-717.
165. Janoschka, T.; Teichler, A.; Häupler, B.; Jähnert, T.; Hager, M. D.; Schubert, U. S., Reactive Inkjet Printing of Cathodes for Organic Radical Batteries. *Advanced Energy Materials* **2013,** *3* (8), 1025-1028.
166. Perelaer, J.; Smith, P. J.; Hendriks, C. E.; van den Berg, A. M.; Schubert, U. S., The preferential deposition of silica micro-particles at the boundary of inkjet printed droplets. *Soft Matter* **2008,** *4* (5), 1072-1078.
167. Young, D.; Sukeshini, A.; Cummins, R.; Xiao, H.; Rottmayer, M.; Reitz, T., Ink-jet printing of electrolyte and anode functional layer for solid oxide fuel cells. *Journal of Power Sources* **2008,** *184* (1), 191-196.
168. Fieldson, G.; Barbari, T., The use of FTi. r.-atr spectroscopy to characterize penetrant diffusion in polymers. *Polymer* **1993,** *34* (6), 1146-1153.
169. Nguyen, T.; Byrd, E.; Bentz, D., Quantifying water at the organic film/hydroxylated substrate interface. *The Journal of Adhesion* **1995,** *48* (1-4), 169-194.
170. Maples, A. L.; Williams, E. B.; Rawlins, J. W., Understanding Scribe Profile and Tool Type Effects on Visual Corrosion Assessments. *Journal of Failure Analysis and Prevention* **2018**.
171. Compère, C.; Fréchette, É.; Ghali, E., The corrosion evaluation of painted and artificially damaged painted steel panels by AC impedance measurements. *Corros. Sci.* **1993,** *34* (8), 1259-1274.
172. Sørensen, P. A.; Dam-Johansen, K.; Weinell, C. E.; Kiil, S., Cathodic delamination of seawater-immersed anticorrosive coatings: Mapping of parameters affecting the rate. *Prog. Org. Coat.* **2010,** *68* (4), 283-292.
173. Pommersheim, J. M.; Nguyen, T.; Zhang, Z.; Hubbard, J. B., Degradation of organic coatings on steel: Mathematical models and predictions. *Prog. Org. Coat.* **1994,** *25* (1), 23-41.

174. Blandin, H. P.; David, J. C.; Vergnaud, J. M.; Illien, J. P.; Malizewicz, M., Modelling of drying of coatings: Effect of the thickness, temperature and concentration of solvent. *Prog. Org. Coat.* **1987,** *15* (2), 163-172.
175. Vrentas, J. S.; Jarzebski, C. M.; Duda, J. L., A Deborah number for diffusion in polymer-solvent systems. *AlChE J.* **1975,** *21* (5), 894-901.
176. Alsoy, S.; Duda, J. L., DRYING OF SOLVENT COATED POLYMER FILMS. *Drying Technol.* **1998,** *16* (1-2), 15-44.
177. Curtzwiler, G.; Early, M.; Gottschalk, D.; Koneckl, C.; Peterson, R.; Wand, S.; Rawlins, J. W., The World of Surface Coatings Is Centered Around the Glass Transition Temperature, But Which One? Part 2. *JCT COATINGSTECH* **2014,** *11* (9), 40-51.
178. Geise, G. M.; Paul, D. R.; Freeman, B. D., Fundamental water and salt transport properties of polymeric materials. *Progress in Polymer Science* **2014,** *39* (1), 1-42.
179. Fox, T. G.; Flory, P. J., The glass temperature and related properties of polystyrene. Influence of molecular weight. *Journal of Polymer Science* **1954,** *14* (75), 315-319.
180. Jr., T. G. F.; Flory, P. J., Second-Order Transition Temperatures and Related Properties of Polystyrene. I. Influence of Molecular Weight. *Journal of Applied Physics* **1950,** *21* (6), 581-591.
181. Li, T.; Zhou, C.; Jiang, M., UV absorption spectra of polystyrene. *Polymer Bulletin* **1991,** *25* (2), 211-216.
182. Si, L.; Massa, M. V.; Dalnoki-Veress, K.; Brown, H. R.; Jones, R. A., Chain entanglement in thin freestanding polymer films. *Physical review letters* **2005,** *94* (12), 127801.
183. Fetters, L.; Lohse, D.; Richter, D.; Witten, T.; Zirkel, A., Connection between polymer molecular weight, density, chain dimensions, and melt viscoelastic properties. *Macromolecules* **1994,** *27* (17), 4639-4647.
184. Adamson, M. J., Thermal expansion and swelling of cured epoxy resin used in graphite/epoxy composite materials. *Journal of Materials Science* **1980,** *15* (7), 1736-1745.
185. Gupta, V. B.; Drzal, L. T.; Rich, M. J., The physical basis of moisture transport in a cured epoxy resin system. *Journal of Applied Polymer Science* **1985,** *30* (11), 4467-4493.
186. Yu, Z.; Yahsi, U.; McGervey, J. D.; Jamieson, A. M.; Simha, R., Molecular weight-dependence of free volume in polystyrene studied by positron annihilation measurements. *Journal of Polymer Science Part B: Polymer Physics* **1994,** *32* (16), 2637-2644.
187. Artamonova, R. V.; Vinogradova, L. M.; Garanina, S. D.; Zherdev, Y. V.; Korolev, A. Y., Internal stresses and water diffusion in polymers. *Polymer Science U.S.S.R.* **1970,** *12* (2), 385-393.
188. Fox, T. G., Influence of diluent and of copolymer composition on the glass temperature of a polymer system. *The Bulletin of the American Physical Society* **1956,** *1*, 123-132.
189. Van Krevelen, D. W., CHAPTER 15 - RHEOLOGICAL PROPERTIES OF POLYMER MELTS. In *Properties of Polymers (Third Edition)*, Van Krevelen, D. W., Ed. Elsevier: Amsterdam, 1997; pp 457-498.

190. Wu, S., Chain structure and entanglement. *Journal of Polymer Science Part B: Polymer Physics* **1989,** *27* (4), 723-741.
191. Lakowicz, J. R., *Principles of fluorescence spectroscopy*. Second edition. New York : Kluwer Academic/Plenum, [1999] ©1999: 1999.
192. Ríos-Corripio, M. A.; García-Pérez, B. E.; Jaramillo-Flores, M. E.; Gayou, V. L.; Rojas-López, M., UV–Visible intensity ratio (aggregates/single particles) as a measure to obtain stability of gold nanoparticles conjugated with protein A. *J. Nanopart. Res.* **2013,** *15* (5), 1624.
193. Alzoubi, F.; Alzouby, J.; Alqadi, M.; Alshboul, H.; Aljarrah, K., Synthesis and characterization of colloidal gold nanoparticles controlled by the pH and ionic strength. *Chinese Journal of Physics* **2015,** *53* (5), 100801-1.
194. Fürbeth, W.; Stratmann, M., Scanning Kelvinprobe investigations on the delamination of polymeric coatings from metallic surfaces. *Prog. Org. Coat.* **2000,** *39* (1), 23-29.
195. Bobe, S. R.; Raynor, A. M.; Bhosale, S. V.; Bhosale, S. V., Detection of Trace Amounts of Water in Organic Solvent by 8-Hydroxypyrene-1,3,6-Trisulfonic Acid Trisodium Salt. *Australian Journal of Chemistry* **2014,** *67* (4), 615-619.
196. Fayomi, O. S. I.; Popoola, A. P. I.; Joseph, O. O., Assessment of Potassium Chromate Inhibition and Adsorption on Type A513 Mild Steel in Simulated Contaminated Media. *Energy Procedia* **2017,** *119*, 883-890.
197. Baghni, I. M.; Lyon, S. B.; Ding, B., The effect of strontium and chromate ions on the inhibition of zinc. *Surf. Coat. Technol.* **2004,** *185* (2), 194-198.